ABSTRACT

Title of dissertation: ENGINEERING TOPOLOGICAL QUANTUM MATTER WITH PATTERNED LIGHT

Hwan Mun Kim
Doctor of Philosophy, 2021

Dissertation directed by: Professor Mohammad Hafezi
Department of Physics

Topological phases are intriguing phases of matter which cannot be described with traditional characterization methods, and numerous efforts has been put to achieve these exotic phases of matter in a variety of quantum platforms. In this thesis, we discuss how topological quantum states of matter can be engineered by utilizing spatially patterned light, which has become available thanks to the recent advances in beam shaping techniques.

First, we discuss a scheme to construct an optical lattice to confine ultracold atoms on the surface of torus. We investigate the feasibility of this construction with numerical calculations including the estimation of tunneling strengths. We then propose a supercurrent generation experiment to verify the non-trivial topology of the created surface. We propose a scheme to construct fractional quantum Hall states which can demonstrate topological degeneracy. We show how our scheme can be generalized to surfaces with higher genus for exploration of richer topological physics.

Next, we extend our effort for creation of topologically non-trivial surfaces for ultracold atoms to the surfaces with open boundaries. This becomes possible by constructing a bilayer optical lattice with multiple pairs of twist defects. We explain how a spin-dependent optical lattice can serve as the bilayer optical lattice for this purpose. We discuss how fractional quantum Hall states can be loaded on this surface, as well as manipulation and measurement techniques via optical protocols.

Then we turn our attention to electronic systems irradiated by spatially patterned light. In particular, we investigate a way to imprint the superlattice structure in the two-dimensional electronic systems by shining circularly-polarized light. We demonstrate the wide optical tunability of this system allows one to realize a wide variety of band properties. We show that these tunable band properties lead to exotic physics ranging from the topological transitions to the creation of nearly flat bands, which can allow the realization of strongly correlated phenomena in Floquet systems.

Finally, we investigate the Floqut vortex states created by shining light carrying non-zero orbital angular momentum on a 2D semiconductor. We analytically and numerically study the properties of those vortex states, with the methods analogous to the ones applied to superconducting vortex states. We show that such Floquet vortex states exhibit a wide range of tunability, and illustrate the potential utility of such tunability with an example application in quantum state engineering.

ENGINEERING TOPOLOGICAL QUANTUM MATTER WITH PATTERNED LIGHT

by

Hwan Mun Kim

Dissertation submitted to the Faculty of the Graduate School of the
University of Maryland, College Park in partial fulfillment
of the requirements for the degree of
Doctor of Philosophy
2021

Advisory Committee:
Professor Mohammad Hafezi, Chair/Advisor
Professor Maissam Barkeshli
Professor Michael Gullans
Professor Trey Porto
Professor Ronald Walsworth
Professor John Cumings, Dean's representative

Acknowledgments

During the course of my graduate study, I got so much helps and supports from people around me, and I would like to thank these people from my heart. Although numerous people have helped me come up to this point, I would try to list them very briefly.

I really thank my advisor, Mohammad Hafezi, for his continuous support, guidance, and patience. I owe him a lot not just in my knowledge and experience in physics research, but also in ways to present myself and interact with other people.

I was also very fortunate to have opportunities to learn from and collaborate with many brilliant faculties, including Trey Porto, Alexey Gorshkov, Maissam Barkeshli, Jay Sau, Ian Spielman, Andrew Childs, Ivar Martin, and Hideo Aoki, to name a few. I was also happy to be surrounded by many amazing colleagues, including Hossein Dehghani, Guanyu Zhu, Wade DeGottardi, Sunil Mittal, Hirokazu Miyake, Mathias Van Regemortel, Andrey Grankin, Yu-An Chen, Zhicheng Yang, Ze-Pei Cian, Bin Cao, Iman Ahmadabadi, Yijia Xu. I also enjoyed to share our cozy office with Alireza Seif, Zachary Eldredge, and Sabyasachi Barik.

Also, I would like to show my love and appreciation to my family. Having that my parents and my sister are always supporting me and wishing me good luck in my mind, I could have gone through many obstacles in my life so far.

Finally, I deeply thank Joohee Choi for her endless supports and unlimited love. Without her, I would not be the person who I am today. My life is so much better with you, and I truly look forward to all the adventures of our lives.

Table of Contents

List of Tables

List of Figures

Citations to Previously Published Work

Much of this dissertation is based on papers already published. Here we list those publications.

- Chapter 2: "Optical Lattice with Torus Topology", Hwanmun Kim, Guanyu Zhu, J. V. Porto, and Mohammad Hafezi, Phys. Rev. Lett. 121, 133002 (2018).

- Chapter 3: "Twist Defects in Optical Lattice", Hwanmun Kim, Maissam Barkeshli, J. V. Porto, and Mohammad Hafezi, *in preparation.* (2021).

- Chapter 4: "Optical imprinting of superlattices in two-dimensional materials", Hwanmun Kim, Hossein Dehghani, Hideo Aoki, Ivar Martin, and Mohammad Hafezi, Phys. Rev. Research 2, 043004 (2020).

- Chapter 5: "Floquet vortex states induced by light carrying the orbital angular momentum", Hwanmun Kim, Hossein Dehghani, Iman Ahmadabadi, Ivar Martin, Mohammad Hafezi, arXiv:2106.08515 (2021).

Chapter 1: Introduction

1.1 Motivation

Since Klaus von Klitzing first observed the quantum Hall effect [1], tremendous efforts have been put to explore and characterize topological phases of matter. The topological phases are new phases of matter that cannot be described by a symmetry breaking order parameter in Ginzburg-Landau theory [2, 3]. These phases are not just new phases of matter but also used in applications such as metrology [4] and quantum information processing [5, 6].

In the early days of the search for topological phases of matter, it was thought that these states can only exist in condensed matter systems with extreme conditions such as a high magnetic field. Later, it turned out that topological phases of matter are more ubiquitous and the search for topological phases have been extended to various platforms such as ultracold atoms [7–10], superconducting circuits [11–14], photons in waveguides [15–19], photonic crystal [20,21], and optomechanical systems [22, 23]. This list is keep expanding with developments of new techniques to prepare and control classical and quantum systems.

Among many techniques to control quantum systems, the optical manipulation has been highly useful for its wide tunability and its stability. In particular, the

recent advances in shaping optical beams have been successfully applied in systems of ultracold atoms [24–28]. The ability to pattern the beam profile with high precision, however, can be effectively applied to other quantum platforms as well and therefore can open a new possibility of engineering exotic quantum states.

In this thesis, we investigate the possibility of engineering topological quantum states of matter with spatially patterned light. In particular, we study the ways to construct a topologically non-trivial surface for ultracold atoms as well as to engineer topological band structures in driven electronic systems.

1.2 Topological Quantum States

The first widely known topological quantum system is the integer quantum Hall (IQH) state [1, 29–31], which exists in a two-dimensional electron gas under a strong magnetic field and a low temperature. Shortly after, the fractional quantum Hall (FQH) effect was observed. It was discovered that the physics behind the FQH state is quite different from that of the IQH state despite their similar setting.

More recently, spin-orbit-induced topological insulators were discovered [32–38], demonstrating that topological quantum states can exist beside the quantum Hall setting. Later, the concept of topological state was extended to the unconventional superconductor [39–43], the superfluid [44], and gapless systems [45–49].

In this section, we briefly review two widely studied of categories of topological quantum states, the symmetry-protected topological states [50] and the topologically ordered states [3, 51]. The symmetry-protected topological states, such as the

topological insulators, are short-ranged entangled quantum states and they require particular symmetries to be preserved to maintain topological properties. On the other hand, topologically ordered states, such as the FQH states, are long-range entangled quantum states and are robust to any local perturbations regardless of the preservation of the symmetry.

1.2.1 Symmetry-protected Topological States

In condensed matter systems, an electronic band structure may be characterized by topological invariants while it is separated from the other bands. In particular, an index calculated from a band is a topological invariant if the index does not change under any deformation of the Hamiltonian that does not close the gaps between this band and other bands. So if we think of an insulator occupying a single band with a non-zero topological invariant, this insulator cannot be adiabatically deformed into a normal insulator if it remains gapped. A symmetry-protected topological (SPT) phase is a phase of matter where the band can be described by a non-trivial topological invariant as long as particular symmetries are preserved.

One of the most widely used topological invariant is the first Chern number of the band manifold. For example, when a band $\{|\psi_{\mathbf{k}}\rangle\}$ in a 2D material is represented by the crystal momentum $\mathbf{k} = (k_x, k_y)$, the Chern number C of this band can be written as

$$\begin{aligned} C &= \frac{1}{2\pi}\int_{\text{Brillouin Zone}} d^2\mathbf{k}\Omega(\mathbf{k}), \\ \Omega(\mathbf{k}) &= -i\left[\partial_{k_y}\left(\langle\psi_{\mathbf{k}}|\partial_{k_x}|\psi_{\mathbf{k}}\rangle\right) - \partial_{k_x}\left(\langle\psi_{\mathbf{k}}|\partial_{k_y}|\psi_{\mathbf{k}}\rangle\right)\right], \end{aligned} \tag{1.1}$$

where $\Omega(\mathbf{k})$ is the Berry curvature. If an insulator occupies bands whose sum of Chern numbers is non-zero, we call it a topological insulator. If a topological insulator is interfaced with a normal insulator, the gap should close at the interface since the topological invariant cannot change otherwise. Since the bulk parts other than the interface are gapped, electrons can only conduct through the channels on this interface, and they form gapless boundary modes. In general, if two insulators with topological invariant m_1 and m_2 are put together, there are $|m_1 - m_2|$ boundary modes in total.

Since spin-orbit-induced topological insulators are experimentally realized, significant efforts have been put in theoretical classification of different SPT states based on the symmetry of the system. In particular, it turned out that SPT states can be classified by 10 classes based on three discrete symmetries: time-reversal symmetry, particle-hole symmetry, and chiral symmetry [52–54]. In this 10-fold classification scheme, each class can have integer ($\mathbb{Z}$), $\mathbb{Z}_2$, or trivial number as a topological invariant, depending on the dimensionality of the system. Beyond these discrete symmetries, spatial symmetries such as reflection [55, 56], rotation [57–59], inversion [60, 61], and translation [62, 63] have been considered to better classify and characterize different SPT states.

1.2.2 Topologically Ordered States

Topologically ordered states are long-range entangled states unlike SPT states. It means that it cannot be transformed into trivial product state with finite number

of local unitary operations in the thermodynamic limit. For example, the Laughlin wavefunction [64] for the FQH state with filling fraction $1/m$ is given by

$$\Psi_{\text{Laughlin}}(\{z_i\}) = \exp\left(-\frac{1}{4}\sum_i |z_i|^2\right)\prod_{i<j}(z_i - z_j)^m, \tag{1.2}$$

where $z_i = x_i + iy_i$ represents the position of ith electron. As exhibited above, this wavefunction is highly entangled and therefore its physics cannot be captured by a single particle Hamiltonian. Indeed, the Laughlin wavefunction is the exact ground state of the quantum Hall Hamiltonian with the Haldane psuedopotential interaction [65].

To characterize topological orders, the long-range entanglement can be directly used in the form of entanglement entropy [66, 67]. Yet, there are several other ways to characterize topological orders. One such way is to investigate the degeneracy of the ground states [68–73]. For example, the Laughlin state with filling fraction $1/m$ on a Riemann surface with genus g has the ground state degeneracy of m^g. To observe a non-trivial ground state degeneracy, one needs to create a surface with non-zero g, such as torus ($g = 1$), double torus ($g = 2$), and so on. m extracted from this ground state degeneracy is a topological quantum number of this topological order and can be used to distinguish different topological phases.

Another way to characterize topological orders is investigating the braiding statistics of excitations [5, 69, 74–76]. For instance, the excited Laughlin wavefunc-

tion with two quasiholes pinned at ξ_1 and ξ_2 can be written as [64]

$$\begin{aligned}\Psi_{\text{Laughlin, q.h.}}(\{z_i\};\xi_1,\xi_2) &= \exp\left(-\frac{1}{4}\sum_i |z_i|^2\right) \\ &\quad\times \prod_i (z_i-\xi_1)\prod_j (z_j-\xi_2)\prod_{k<l}(z_k-z_l)^m. \end{aligned} \tag{1.3}$$

By adiabatically rotating ξ_2 around ξ_1 in counterclockwise direction, this state picks up the Berry phase of $2\pi/m$. This means that the statistical angle of exchange statistics is π/m and is neither fermionic or bosonic statistics, and these quasihole (or quasiparticle) excitations are called anyons. In case of the Laughlin state, these excitations are Abelian anyons since its braiding only yields an extra phase and does not alter the state vector itself. For other topologically ordered states, excitations can have non-Abelian braiding statistics [5, 76]. These different braiding statistics can be used for the characterization of different topological orders.

1.3 Floquet Theory for Driven Quantum Systems

In this section, we review the Floquet theory for time-periodic quantum systems [77–79]. Especially, we review how such systems can be more simply described in the high-frequency regime [80, 81]. The high-frequency regime is particularly relevant to the optically driven systems since optical frequencies are often far higher than the energy scales of interest in many quantum systems.

Floquet theory was originally developed for periodic linear ordinary differential equations by Gaston Floquet [82]. Now let us apply the Floquet theorem, the main result of the theory, to the Schrödinger equation for a time-periodic quantum system

$H(t) = H(t+T)$ which can often occur in a quantum system driven with frequency $\Omega = 2\pi/T$. The Floquet theorem tells that the steady-state solution of this system is given in the form of

$$|\psi_\alpha(t)\rangle = \exp(-i\epsilon_\alpha t)\,|\phi_\alpha(t)\rangle\,, \qquad |\phi_\alpha(t)\rangle = |\phi_\alpha(t+T)\rangle\,, \tag{1.4}$$

given that the Hamiltonian $H(t)$ is Hermitian. Here, the eigenvalues of the system $\{\epsilon_\alpha\}$ are called quasienergies and they are bounded in the range of $[-\Omega/2, \Omega/2)$. This is because we can replace any state with unbounded quasienergy ϵ'_α with a bounded quasienergy $\epsilon_\alpha = \epsilon'_\alpha - n\Omega$ $(n \in \mathbb{N})$ by setting the periodic states to be $e^{in\Omega t}\,|\phi_\alpha(t)\rangle$. The motion described by the periodic part of the solution $|\phi_\alpha(t)\rangle$ is also called the mircomotion of the state.

The steady solution in Eq. (1.4) indeed resembles Bloch states in its mathematical form. Due to this similarity, the bounded range for the quasienergies, $[-\Omega/2, \Omega/2)$, is often called the Floquet-Brillouin zone. Yet, one big difference is that crystalline systems are periodic over position $\mathbf{r}$ which is a quantum operator that acts on the Hilbert space while time t is merely an external parameter in non-relativistic quantum mechanics. Therefore, the Floquet theory for periodic quantum system necessarily involve infinitely many copies of the Hilbert space, one for each $t \in [0, T)$, while the Bloch theory is completely described within a single copy of the Hilbert space. This issue can be resolved by lifting the vectors in Hilbert space into the space called the Floquet-Hilbert space, also called as the Sambe space following Hideo Sambe [77]. That is, for a vector $|\psi\rangle$ in the Hilbert space at time t is lifted

to a vector $|\psi\rangle\,|t)$ in the Floquet-Hilbert space. Now the Schrödinger equation for a periodic system simply becomes an eigenvalue problem in this Floquet-Hilbert space,

$$[H(t) - i\partial_t]\,|\phi_\alpha(t)\rangle = \epsilon_\alpha\,|\phi_\alpha(t)\rangle\,. \tag{1.5}$$

Here, $H(t) - i\partial_t$ is often called as a Floquet Hamiltonian. In practice, it is more beneficial to use the Fourier basis:

$$|n, j\rangle\!\rangle = T^{-1}\int_0^T dt\; e^{in\Omega t}\,|j\rangle\,|t). \tag{1.6}$$

In this basis, the Floquet Hamiltonian can be written as

$$\begin{aligned} H(t) - i\partial_t &= \sum_{n,q}\sum_{j,j'}\langle j'|H_q|j\rangle\,|n+q, j'\rangle\!\rangle\langle\!\langle n, j| + \sum_n\sum_j n\Omega|n, j\rangle\!\rangle\langle\!\langle n, j| \\ &\equiv \hat{H} + \hat{Z} \end{aligned} \tag{1.7}$$

where $H_q = T^{-1}\int_0^T H(t)e^{-iq\Omega t}dt = H_{-q}^\dagger$ is the harmonic components of the Hamiltonian. To understand the meaning of the Floquet Hamiltonian in this basis, we visualized each terms of Eq. (1.7) in Fig. 1.1. From this figure, we can perceive eigenstates of H_0 as different orbitals localized around each Floquet-Brillouin zone in the extended zone scheme. In this interpretation, $H_{q(\neq 0)}$ acts as tunnelings between different Floquet-Brillouin zones while $\hat{Z}$ does the role of a linear on-site potential for the lattice of Floquet-Brillouin zones. In this perspective, the Floquet

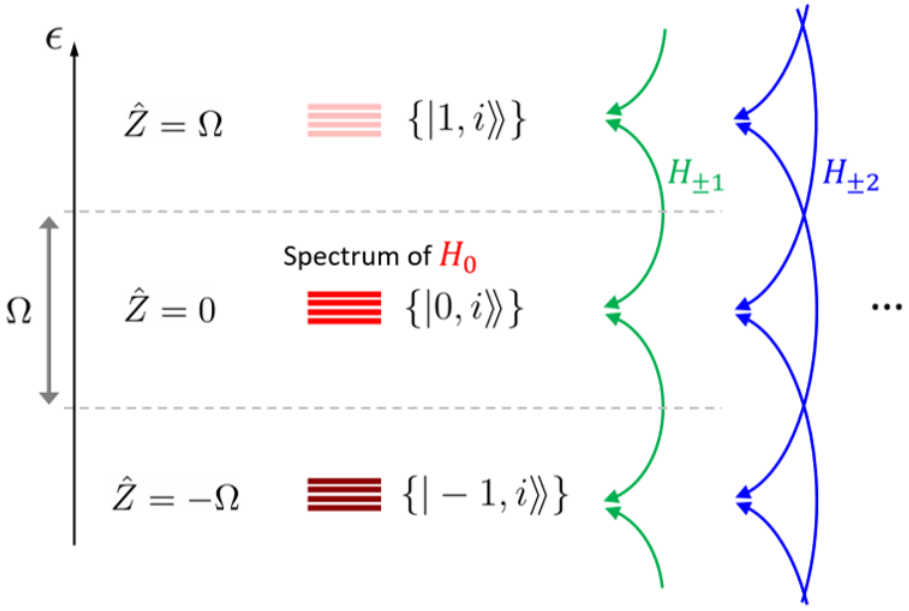

Figure 1.1: A schematic representation of the Floquet Hamiltonian.

Hamiltonian can be understood as a Wannier-Stark problem [83, 84].

1.3.1 High-frequency Expansion

While the full description of a driven quantum system requires the Floquet-Hilbert space, one may get an effective description within a single copy of the Hilbert space in the high-frequency regime. One technique to derive this description is to use the high-frequency expansion (HFE), which is a perturbation expansion in the limit where Ω dominates over all the other energy scales in the problem.

While there are several schemes to carry out this perturbation expansion, the Schrieffer-Wolff (SW) transformation [85, 86] is particularly useful to obtain an effective Hamiltonian description. To apply the SW transformation to some perturbed Hamiltonian $H_{\text{total}} = H_{\text{u.p.}} + V$, we first let $\{|\psi_i\rangle\}$ and $\{E_i\}$ be the eigenstates and the eigenenergies of $H_{\text{u.p.}}$ with $E_i \leq E_{i+1}$. Now one consider a subset

of the Hilbert space $\mathcal{S}$ which can be spanned by the eigenstates of $H_{\text{u.p.}}$ corresponding to eigenenergies $E_k, \cdots, E_l$. Then the SW transformation is applicable if $|V| \ll \min(E_k - E_{k-1}, E_{l+1} - E_l)$. When this condition is satisfied, the effective Hamiltonian within $\mathcal{S}$ is given by

$$H_{\text{eff}} = H_{\text{u.p.}} P + PVP + \frac{1}{2} P \left(\sum_{k \le i,j \le l} \frac{\langle \psi_i | V | \psi_j \rangle}{E_i - E_j} \left[|\psi_i\rangle \langle \psi_j| , V \right] \right) P + O\left(V^3\right), \quad (1.8)$$

where P is the projection operator onto $\mathcal{S}$.

Back to the HFE, we can use the SW transformation if we choose $H_{\text{u.p.}} = \hat{Z}$, $V = \hat{H}$, and $P = \hat{P} = \sum_\alpha |n, \alpha\rangle\!\rangle\langle\langle n, \alpha|$ where $\{|\alpha\rangle\}$ is an arbitrary basis that spans the Hilbert space. Without loss of generality, we can set $n = 0$. Now the SW transformation is applicable as long as $|H_q| \ll \Omega$ for all q. Note that this condition requires the static part of the Hamiltonian, H_0, to be smaller than Ω as well. Then, from Eq. (1.8), the effective Hamiltonian description up to the second order in the perturbation is given by

$$\begin{aligned}
\hat{H}_F &= \sum_\alpha \langle \alpha | H_0 | \alpha \rangle |0, \alpha\rangle\!\rangle\langle\langle 0, \alpha| + \frac{1}{2} \sum_{\alpha,\beta,\gamma} \sum_{q \neq 0} \left(\frac{2 \langle \alpha | H_{-q} | \gamma \rangle \langle \gamma | H_q | \beta \rangle}{-q\Omega} \right) |0, \alpha\rangle\!\rangle\langle\langle 0, \beta| \\
&= \sum_\alpha \langle \alpha | H_0 | \alpha \rangle |0, \alpha\rangle\!\rangle\langle\langle 0, \alpha| + \sum_{\alpha,\beta} \sum_{q>0} \frac{\langle \alpha | [H_q, H_{-q}] | \beta \rangle}{q\Omega} |0, \alpha\rangle\!\rangle\langle\langle 0, \beta| \\
&= \left(H_0 + \sum_{q>0} \frac{[H_q, H_{-q}]}{q\Omega} \right) \otimes \frac{1}{T} \int_0^T |t)(t| dt \equiv H_F \otimes \frac{1}{T} \int_0^T |t)(t| dt. \qquad (1.9)
\end{aligned}$$

Therefore, we can reconstruct the quasienergy spectrum of this system only by diagonalizing H_F instead of the entire Floquet Hamiltonian in this regime. Note that $\mathcal{S}$ is fixed to the $n = 0$ states, so H_F can be factored out from $\hat{H}_F$ regardless of

the perturbation order, therefore a higher order expression for H_F can be found by applying the higher order expansions of Eq. (1.8) which can be found in Ref. [86].

1.3.2 Rotating Wave Approximation

Now let us treat the rotating wave approximation (RWA) in the perspective of the Floquet theory in the high-frequency regime. Just as in the previous section, we can obtain an effective RWA Hamiltonian description with the SW transformation in Eq. (1.8). Yet, we choose the subspace and the perturbation differently. That is, we select

$$\begin{aligned} H_{\text{u.p.}} &= \hat{Z} + \textstyle\sum_n \sum_{j,j'} \langle j'|H_0|j\rangle \, |n,j'\rangle\!\rangle\langle\!\langle n,j|, \\ V &= \textstyle\sum_{n'\neq n} \sum_{j,j'} \langle j'|H_{n'-n}|j\rangle \, |n',j'\rangle\!\rangle\langle\!\langle n,j|, \\ P &= \hat{P} = \textstyle\sum_n \sum_{|j\rangle\in S_n} |n,j\rangle\!\rangle\langle\!\langle n,j|, \end{aligned} \tag{1.10}$$

where $\{S_n\}$ is a set of non-overlapping subspaces of the Hilbert space. We let $\{|\psi_i^{(0)}\rangle\}$ and $\{E_i^{(0)}\}$ be the eigenstates and the eigenenergies of H_0. Then we define the spectral gap for each harmonic components, $\Delta_{q(>0)}$, as

$$\Delta_q = \min\left(\bigcup_n \bigcup_{m=-q,q} \left\{ |E_i^{(0)} - E_j^{(0)} - m\Omega| \,\middle|\, |\psi_i^{(0)}\rangle \in S_n, |\psi_j^{(0)}\rangle \notin S_{n+m} \right\} \right). \tag{1.11}$$

Then we require $|H_q| \ll \Delta_q$ for all $q > 0$ to apply the SW transformation. Under this condition, the effective Hamiltonian up to the first order in the perturbation is

given by

$$\begin{aligned}\hat{H}_{\mathrm{RWA}} &= \sum_{n}\sum_{|\psi_i^{(0)}\rangle\in S_n}\left(n\Omega+E_i^{(0)}\right)|n,\psi_i^{(0)}\rangle\!\rangle\langle\!\langle n,\psi_i^{(0)}| \\ &\quad+\sum_{n'\neq n}\sum_{|j\rangle\in S_n}\sum_{|j'\rangle\in S_{n'}}\langle j'|H_{n'-n}|j\rangle\,|n',j'\rangle\!\rangle\langle\!\langle n,j| \end{aligned} \tag{1.12}$$

.

To understand the RWA in a detailed example, let us consider a two-band system H_0 perturbed by a simple harmonic driving $H_1e^{i\Omega t}+H_{-1}e^{-i\Omega t}$. To describe how the two bands are hybridized by the driving, we use the RWA. In this case, we may choose $S_0=\{|j\uparrow\rangle\}$ to be the upper-band subspace and $S_1=\{|j\downarrow\rangle\}$ to be the lower-band subspace while we set all the other S_n empty. In this case, the spectral gap Δ_1 is set by the interplay of the bandwidth and the driving frequency. Yet, if we can assume this driving is reasonably local in the momentum space, i.e. slowly changing over the space compared to the lattice constant, then we can make $\Delta_1\simeq\Omega$ by slicing the Brillouin zone and choose S_0 and S_1 within the momenta in each slice. In this case, we require $|H_1|\ll\Omega$ for the RWA, and it leads to the RWA Hamiltonian

$$\begin{aligned}\hat{H}_{\mathrm{RWA}} &= \sum_{j,j'}(\langle j'\uparrow|H_0|j\uparrow\rangle\,|0,j'\uparrow\rangle\!\rangle\langle\!\langle 0,j\uparrow|+\langle j'\downarrow|H_0|j\downarrow\rangle\,|1,j'\downarrow\rangle\!\rangle\langle\!\langle 1,j\downarrow| \\ &\quad+\langle j'\downarrow|H_1|j\uparrow\rangle\,|1,j'\downarrow\rangle\!\rangle\langle\!\langle 1,j\uparrow|+\langle j'\uparrow|H_{-1}|j\downarrow\rangle\,|1,j'\uparrow\rangle\!\rangle\langle\!\langle 1,j\downarrow|)\end{aligned} \tag{1.13}$$

which describes the hybridization of the two bands.

1.3.3 Remarks

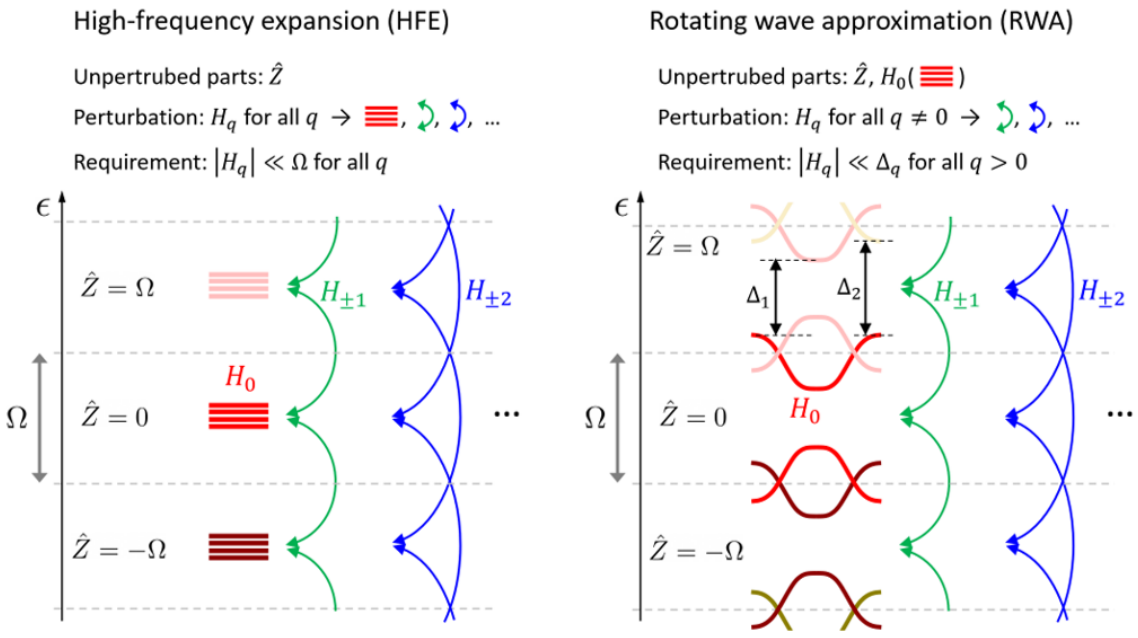

Figure 1.2: Comparison between the high-frequency expansion (HFE) and the rotating wave approximation (RWA).

To summarize, we present the difference between the HFE and the RWA in Fig. 1.2. While these two approaches are both used in the high-frequency regime, the requirement of each approximation is slightly different and one need to be cautious. In general, the HFE is used to find the correction of the entire energy spectrum due to the second order effect in the perturbation. On the other hand, the RWA is used to find the interplay of different energy levels (or bands, if there is any good quantum number which can parameterize the system) connected by the driving as the linear order effect of the perturbation.

So far, we have not said much about the symmetry of the driving term while reviewing the Floquet theory. In fact, if the driving term itself has spatial periodicity, the Floquet theory can be extended to a formalism for spacetime crystals [87,88].

Beside the spatial lattice translations, the driven quantum systems with other symmetries can also lead to rich physics [89, 90].

1.4 Optically Driven Quantum Systems

If an electron under the quantum Hamiltonian $H(\mathbf{p}, \mathbf{r})$ is applied with electromagnetic field represented by the electrostatic potential $V(\mathbf{r})$ and the magnetic potential $\mathbf{A}(\mathbf{r}, t)$, its dynamics is described by a new quantum Hamiltonian $H(\mathbf{p} + e\mathbf{A}(\mathbf{r}, t)/\hbar, \mathbf{r}) - eV(\mathbf{r})$ via minimal coupling $\mathbf{p} \to \mathbf{p} + e\mathbf{A}(\mathbf{r}, t)/\hbar$. This description through minimal coupling Hamiltonian is valid as long as the applied electromagnetic field is the coherent light. If we consider a quantum system driven by irradiation of electromagnetic wave, we may disregard the electrostatic potential $V(\mathbf{r})$. The remaining minimal coupling Hamiltonian $H(\mathbf{p} + e\mathbf{A}(\mathbf{r}, t)/\hbar, \mathbf{r})$ is a time-periodic Hamiltonian which can be understood with the Floquet theory described in the Section 1.3. In the case of optically driven quantum systems, the radiation frequency is a few hundreds THz which translates into a few eV per photon. This is quite high energy scale in many quantum systems, so the approximations in the high-frequency regime is often applicable.

1.4.1 Neutral Atoms with Driving Fields

While the description of driven electronic material is rather straightforward since an electron is a charged elementary particle, it is less obvious how optical driving fields affect the motion of a neutral atom. The essence of this atomic motion

can be understood with a simple two-level problem. Let us consider the transition between an atomic orbital $|g\rangle$, which is one of the occupied orbitals of the ground state of the atom, and an excited orbital $|e\rangle$. Supposing the transition frequency is ω_0, the static Hamiltonian of this two-level problem is simply $\hbar\omega_{ge}\,|e\rangle\,\langle e|$. Under the presence of electric field oscillating with frequency ω, the electric dipole potential energy is given by $-\mathbf{d}\cdot\mathbf{E}(t)$ where $\mathbf{d}=-e\mathbf{r}$ is the electric dipole operator. While each orbital has no intrinsic dipole moment ($e\,\langle g|\mathbf{r}|g\rangle = e\,\langle e|\mathbf{r}|e\rangle = 0$), the transition dipole moment ($\mu_{eg} = e\,\langle e|\mathbf{r}|g\rangle = \mu_{ge}^*$) can be non-zero. Now by writing $\mathbf{E}(t)\cdot\mu_{eg} = \Omega e^{-i\omega t} + \bar{\Omega}e^{i\omega t}$, the time-dependent Hamiltonian of this two-level problem becomes

$$H_{\text{2-level}} = \hbar\omega_{ge}\,|e\rangle\,\langle e| + \hbar\left(\Omega e^{-i\omega t} + \bar{\Omega}e^{i\omega t}\right)|e\rangle\,\langle g| + \hbar\left(\Omega^* e^{i\omega t} + \bar{\Omega}^* e^{-i\omega t}\right)|g\rangle\,\langle e|\,. \quad (1.14)$$

The temporal Fourier components of this Hamiltonian are $H_0 = \hbar\omega_{ge}\,|e\rangle\,\langle e|$ and $H_1 = \hbar\bar{\Omega}\,|e\rangle\,\langle g| + \hbar\Omega^*\,|g\rangle\,\langle e| = H_{-1}^\dagger$. Then we can use RWA in Eq. (1.12) with the choice of $S_0 = \{|e\rangle\}$ and $S_1 = \{|g\rangle\}$, which leads to the RWA Hamiltonian

$$H_{\text{RWA}} = \hbar\omega_{ge}|0,e\rangle\!\rangle\langle\!\langle 0,e| + \hbar\omega|1,g\rangle\!\rangle\langle\!\langle 1,g| + \hbar\Omega|0,e\rangle\!\rangle\langle\!\langle 1,g| + \hbar\Omega^*|1,g\rangle\!\rangle\langle\!\langle 0,e|, \quad (1.15)$$

and this RWA Hamiltonian is valid as long as $|\Omega| \ll \omega$. By adjusting the offset energy by subtracting $\hbar\omega_{ge}I$ from this Hamiltonian and writing the detuning $\delta = \omega - \omega_{ge}$, this RWA Hamiltonian can be also written as $\hbar\delta|1,g\rangle\!\rangle\langle\!\langle 1,g| + \hbar\Omega|0,e\rangle\!\rangle\langle\!\langle 1,g| + \hbar\Omega^*|1,g\rangle\!\rangle\langle\!\langle 0,e|$. Then the eigenenergies of this Hamiltonian are given by $\epsilon_\pm = \hbar(\delta/2)\left(1 \pm \sqrt{1+4|\Omega|^2/\delta^2}\right)$. In the large detuning limit $|\Omega| \ll \delta$, the dressed state

close to the ground state has the eigenenergy $\epsilon_+ = \hbar\delta + \hbar|\Omega|^2/\delta + O\left(\hbar|\Omega|^4/\delta^3\right)$. This indicates that the ground state gains an extra energy offset $\hbar|\Omega|^2/\delta$ which corresponds to the AC stark shift [91].

In case the irradiated beam is spatially patterned so that $\Omega = \Omega(\mathbf{r})$, this energy offset provides a potential landscape for the atom. The total potential is given by the summation of energy offsets corresponding to all possible atomic transitions which are allowed by the selection rule $\mu_{eg} \neq 0$. Yet, a term corresponding to particular transition ($|g\rangle \rightarrow |e\rangle$) can dominate if the driving frequency is tuned close to that transition frequency ω_{ge}. In this case, the sign of this potential can be controlled by choosing the detuning postive (blue-detuned) or negative (red-detuned). This potential can be shaped into different lattice patterns by superposing several beams, which are called optical lattices [92,93]. For example, two counter-propagating plane waves $\mathbf{E_1}(x,t) = \left(E_0 e^{i(qx-\omega t)} + \text{c.c.}\right)\hat{\mathbf{y}}$ and $\mathbf{E_2}(x,t) = \left(E_0 e^{i(-qx-\omega t)} + \text{c.c.}\right)\hat{\mathbf{y}}$ yield the potential $U(x) = \left(4E_0^2\left|\mu_{eg,y}\right|^2\hbar/\delta\right)\cos^2(qx)$ which creates a 1D lattice of a lattice spacing π/q.

1.5 Recent Advances in Patterning Optical Beam

While the interference pattern of several optical beams can generate spatial patterns such as lattice patterns in optical lattices, there are other useful optical manipulations, such as addressing of single lattice site, which cannot be implemented by interfering several plane beams. In this section, we briefly review some of the recent advances in techniques of spatially patterning the optical beams which can

help to create and control exotic quantum states.

One promising technique is the holographic beam shaping using digital micro-mirror devices (DMD) [94]. A DMD is composed of a 2D array of small mirror patches which are individually turned on and off by switching the orienting angle of the mirror. With a given angle of the incident beam and the given target amplitude pattern, the binary map of DMD panel to generate that target amplitude pattern can be calculated. This can generate an arbitrary amplitude pattern of the beam with precision comparable to the optical wavelength. This can be used for simultaneous addressing of single lattice sites for ultracold atoms loaded on an optical lattice, and therefore can be used for the quantum gas microscope [95]. Further, each mirror cell can be switched with a rate of a few kHz; therefore, we can also update the amplitude pattern of the beam with the same rate [96].

Another useful imaging tool for optical manipulation is the optical tweezer [97]. It uses a focused laser beam which maximizes the intensity at a focal point and the center of the beam profile. If the frequency of the beam is red-detuned from a particular atomic transition, the AC stark shift on an atom provides a trapping potential. With a high-resolution optical tweezer, one can individually capture single atoms and move them around freely. It can even be used to assemble multiple atoms to construct an arbitrary atomic structure in any dimension up to three [98–100].

1.6 Outline of Thesis

The remainder of this thesis is organized as follows.

- In chapter 2, we propose an experimental scheme to construct an optical lattice where the atoms are confined to the surface of a torus. This construction utilizes the spatially shaped laser beams which could be realized with recently developed high resolution imaging techniques. To study the feasibility of this proposal, the tunneling strengths for atoms in the torus lattice are numerically calculated. To illustrate the nontrivial role of topology in atomic dynamics on the torus, we study the quantized superfluid currents and fractional quantum Hall states on such a structure. We then numerically investigate the robustness of the topological degeneracy of such fractional quantum Hall states and propose an experimental way to detect this degeneracy. We also demonstrate how this scheme for torus construction can be generalized to surfaces with higher genus for exploration of richer topological physics.

- In chapter 3, we propose an experimental scheme to construct a bilayer optical lattice with multiple pairs of twist defects. These pairs of twist defects effectively embed the ultracold atoms in a topologically non-trivial surface with open boundaries. To locate the twist defects in the optical lattice, recently developed high resolution imaging techniques can be utilized for site-resolving shaping of the laser beams. To demonstrate the effect of non-trivial topology in atomic dynamics, we investigate the quantized supercurrents and fractional quantum Hall states on this structure. We also investigate how the degenerate fractional quantum Hall ground states on this manifold can be measured and manipulated via optical manipulations.

- In chapter 4, we propose an optical method of shining circularly polarized and spatially periodic laser fields to imprint superlattice structures in two-dimensional electronic systems, by studying the case of monolayer graphene. We particularly consider the high-frequency regime where the electronic system can remain in the quasiequilibrium phase for an extended amount of time. We demonstrate that the wide optical tunability allows one to tune different properties of the effective band structure, including Chern number, energy bandwidths, and band gaps. We also demonstrate that this tunability of the superlattice leads to unique physics ranging from the topological transitions to the creation of flat bands in a kagome superlattice, which may allow the experimental realization of strongly correlated phenomena in Floquet systems.

- In chapter 5, we propose a scheme to create an electronic Floquet vortex state by irradiating a two-dimensional semiconductor with the laser light carrying non-zero orbital angular momentum. We analytically and numerically study the properties of the Floquet vortex states, with the methods analogous to the ones previously applied to the analysis of superconducting vortex states. With this analysis, we show that the number of created vortex modes is equal to the vorticity of the applied beam. We also show that such Floquet vortex states exhibit a wide range of tunability, and illustrate the potential utility of such tunability with an example application in quantum state engineering.

Chapter 2: Optical Lattice with Torus Topology

2.1 Introduction

In the past decades, ultracold atoms in optical lattices have been widely used to study a range of interesting coherent and many-body physics [101]. In particular, there has been remarkable progress in investigating phenomena [7, 8, 102, 103] in both different dimensions [104–106] and lattice geometries, such as square [102, 104], triangular [107], honeycomb [108], kagome [109], ring [110], cylinder [111], and more recently ribbon lattices with synthetic dimensions [10].

Meanwhile, intriguing physics can be explored in systems with non-trivial topologies. For example, it is theoretically predicted that there are topologically protected degeneracies on surfaces with non-zero genus, like the fractional quantum Hall (FQH) model [72, 112] or spin liquids [113–115]. Such systems are expected to not only contain rich many-body physics but also possibly be used in topological quantum computation [113]. While there have been interesting proposals to make torus surfaces in ultracold atomic systems, using synthetic dimensions [116] and semi-2D geometries by modifying cylinders [117, 118], the experimental construction of a torus in real space has remained challenging. Moreover, the presence of edge physics and the finite size effects have made the observation of FQH effect in

ultracold atoms challenging.

In this chapter, we propose a scheme to construct an optical lattice in which atomic dynamics is confined to the surface of a torus. Our construction makes use of recent advances in beam shaping, in the context of ultracold atomic systems [94, 98–100, 119]. Specifically, we show that a rectangular square lattice with a hole in the middle can be turned into the surface of a torus by shaping a single beam perpendicular to the layers (Fig. 2.1). Moreover, we discuss that this construction could be generalized to surfaces with higher genus. To illustrate the non-trivial role of topology in atomic dynamics on the torus, we first investigate the hydrodynamics of bosonic superfluid on the torus. Specifically, we demonstrate a sequence of optical manipulations that generates quantized supercurrents in two intersecting non-contractible cycles. Furthermore, in the strongly correlated regime, we discuss a FQH model which can be realized on this torus. To numerically investigate the topological degeneracy on such system, we consider a relatively small square lattice (6×6) with torus topology. We show that the anticipated topological degeneracy exists and is robust against the discrepancy between inter- and intra-layer tunneling and disorder. Moreover, we propose a way to experimentally detect the topological degeneracy.

2.2 Torus Construction

In the following, we show that by using several pairs of laser beams in the x, y, and z directions, one can build an optical lattice in which atomic dynamics

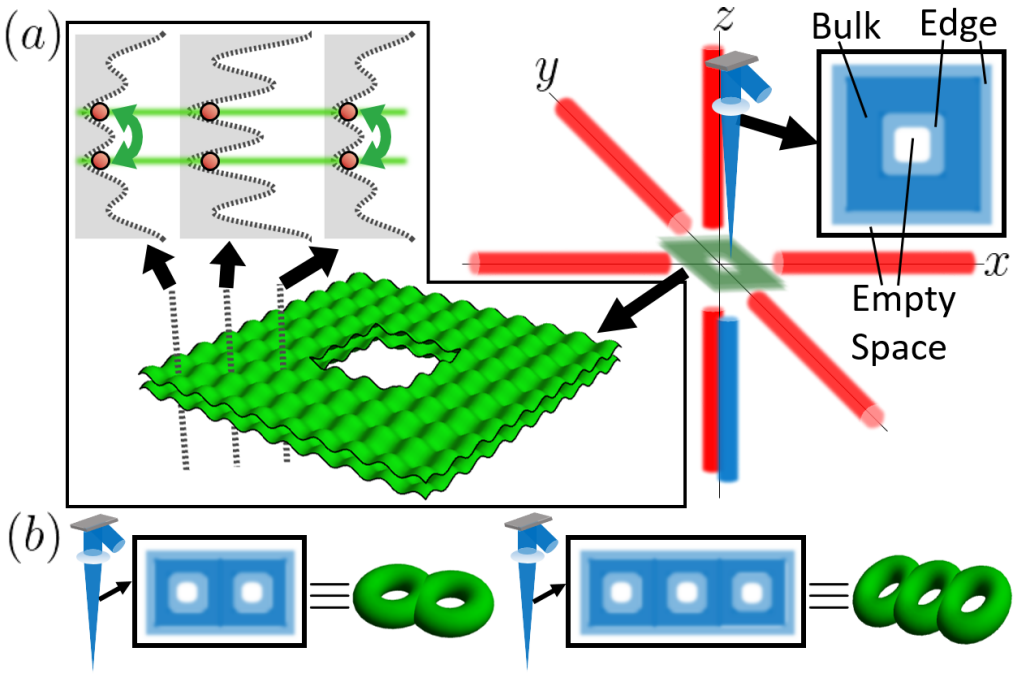

Figure 2.1: (a) Schematic beam configuration for a torus surface in an optical lattice. Plane wave beams in the horizontal directions generate a rectangular lattice in the xy plane. In the z direction, a superlattice structure created by pairs of blue-detuned and red-detuned beams confines atoms in two layers. The $-z$ propagating blue-detuned beam has the beam shape of a square annulus. (Inset) Different laser intensities turn the inter-layer tunneling on and off in different regions. To complete the torus surface, only the inter-layer tunneling on in the edge region is allowed. (b) Generalization of the scheme to surfaces with higher genus ($g = 2, 3$ shown for example) can be achieved by puncturing more holes in the middle of the lattice.

is confined to the surface of a torus (Fig. 2.1). We first make a bilayer system by creating a superlattice structure in the z direction. Using high resolution optics, we then tailor one of the beams used in the superlattice structure to have the shape of a square annulus. This square annulus divides the xy plane into three regions: *bulk*, *edge*, and *empty space* [Fig. 2.1(a)]. By having a different set of intensities in these regions, the trap potential can be arranged to only allow atoms to vertically tunnel through lattice sites in the edge region, thus confining atoms to the surface of a torus.

To prepare a bilayer system, we use a 3D optical lattice with a superlattice structure in the z direction. Red-detuned laser beams with wavevectors $\pm k_x \hat{\mathbf{x}}$ and $\pm k_y \hat{\mathbf{y}}$ form a 2D rectangular lattice with lattice spacings $(a_x, a_y) = (\pi/k_x, \pi/k_y)$. For the superlattice structure, we use a pair of blue-detuned lasers with wavevectors $\pm k_z \hat{\mathbf{z}}$ and another pair of red-detuned lasers with wavevectors $\pm q_z \hat{\mathbf{z}}$. When the $\pm z$ propagating beams do not vary in the xy plane, the combined vertical dipole potential is given by $V_z(z) = V_b(z) + V_r(z) = V_{\text{blue}} \cos^2(k_z z) - V_{\text{red}} \cos^2(q_z z)$ for properly chosen relative phases, where V_{blue} (V_{red}) is the amplitude of the dipole potential generated by the blue-detuned (red-detuned) beam pair alone. Then atoms with atomic mass m can be confined at two neighboring minima, which we call the $\pm z_0$, as shown in Fig. 2.2(b). Atoms in these minima constitute the bilayer system.

To complete the torus surface, we tailor the $-z$ propagating blue-detuned beam in the shape of a square annulus in the xy plane, adjusted to achieve the desired inter-layer tunneling only along edge sites. In particular, we make the laser intensity lower at the edge compared to the bulk region. The resulting potential barrier in the z direction is shallower at the edge than the bulk, which makes the inter-layer tunneling non-zero at the edge while negligible in the bulk region. With the laser intensity of the $-z$ propagating beam set to zero in the empty space region, the $+z$ propagating blue-detuned beam generates a higher dipole potential in the empty space compared to the edge and the bulk region. This difference in dipole potential energetically prevents atoms from escaping the designated square annulus.

To be concrete, we consider the following beam shapes for the blue-detuned

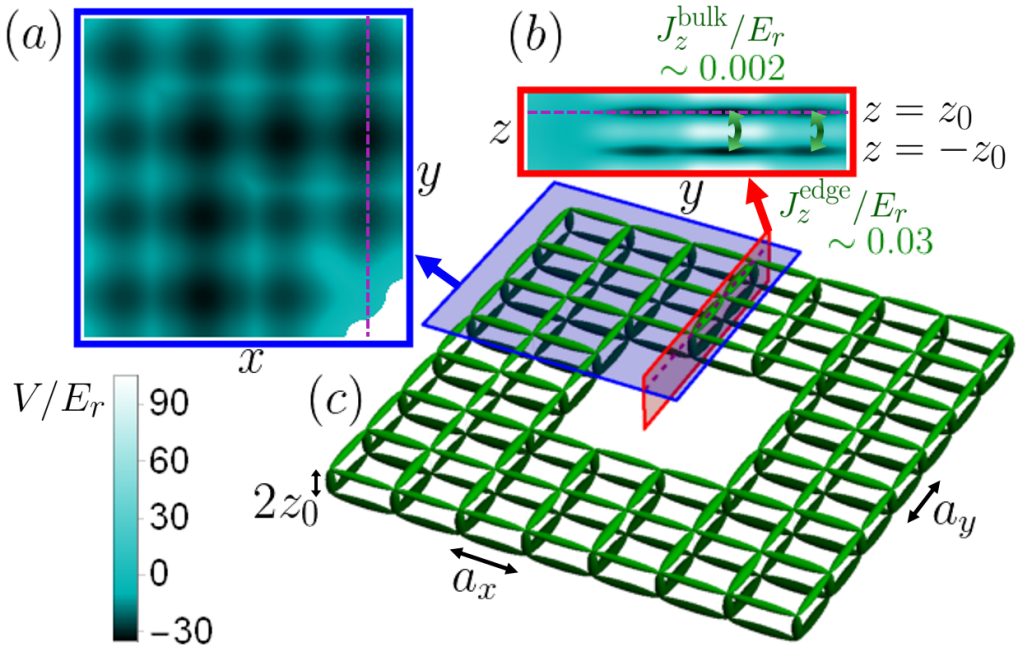

Figure 2.2: Numerically evaluated dipole potential and tunneling strengths. We consider Rb^{87} atoms with $a_x \simeq a_y = 480$ nm and $k_x = k_z/2 = 2q_z$. In the unit of recoil energy $E_r \equiv \hbar^2 k_x^2/2m$ ($E_{r,z} \equiv \hbar^2 k_z^2/2m$), $V_0 = 8E_r, V_{\rm E} = 60E_r = 15E_{r,z}, V_{\rm B} = 120E_r = 30E_{r,z}$, and $V_{\rm red} = 20E_r = 5E_{r,z}$. (a) Dipole potentials in the xy plane on the upper layer. (b) Dipole potentials in the yz plane. Inter-layer tunneling strengths in bulk ($J_z^{\rm bulk}$) and edge ($J_z^{\rm edge}$) are shown for comparison. (c) Numerically evaluated tunneling strengths represented as the thickness of bonds in the 3D lattice. Shown tunneling strengths range from $0.03E_r$ to $0.04E_r$.

beams:

$$\mathbf{E}_+(\mathbf{r},t) = \hat{\mathbf{y}}\left(e^{+ik_z(z-ct)} + \text{c.c.}\right)\mathcal{E}_+, \tag{2.1}$$

$$\mathbf{E}_-(\mathbf{r},t) = \hat{\mathbf{y}}\left(e^{-ik_z(z+ct)} + \text{c.c.}\right)\begin{cases} \mathcal{E}_{\rm B} & \text{bulk} \\ \mathcal{E}_{\rm E} & \text{edge} \\ 0 & \text{empty space} \end{cases}.$$

In this discrete setting, bulk and edge regions correspond to the zones around bulk and edge sites in the square annulus, within the distance $a_x/2$ ($a_y/2$) in the x (y) direction. The rest of the area is designated as empty space. For illustrative pur-

poses, we assume the model beam has sharp boundaries between different regions, but in an experimental realization, one can relax this constraint and construct a good approximation of Eq. (2.1) using beams with sufficient numerical apertures ($0.17 \sim 0.80$) (see Sec. 2.5). The recent progress in beam-shaping techniques for optical lattices [94, 98–100, 119] could allow one to realize such a beam profile in the lab. Note that this beam profile should be placed properly in the xy plane in a way that regional distinctions in Eq. (2.1) match with the horizontal lattice sites.

This beam profile gives rise to the combined vertical dipole potential including interference between the $+z$ and $-z$ propagating beams:

$$
\begin{aligned}
V_z(\mathbf{r}) &= V_b(\mathbf{r}) - V_{\mathrm{red}} \cos^2(q_z z), \qquad (2.2)\\
V_b(\mathbf{r}) &= \begin{cases} V_{\mathrm{B}} \cos^2(k_z z) + V_{\mathrm{B}}^{(0)} & \text{bulk} \\ V_{\mathrm{E}} \cos^2(k_z z) + V_{\mathrm{E}}^{(0)} & \text{edge} \\ V_{\mathrm{S}} & \text{empty space} \end{cases},
\end{aligned}
$$

where the lattice potential amplitudes are $V_{\mathrm{B/E}} = 4 f_0 \mathcal{E}_+ \mathcal{E}_{\mathrm{B/E}}$, and the energy offsets are $V_{\mathrm{B/E}}^{(0)} = f_0(\mathcal{E}_+ - \mathcal{E}_{\mathrm{B/E}})^2$, $V_{\mathrm{S}} = f_0 \mathcal{E}_+^2$. Here, the proportionality constant f_0 depends on beam frequency, dipole elements, and transition frequency [120]. By setting $\mathcal{E}_{\mathrm{B}} > \mathcal{E}_{\mathrm{E}}$, the potential barrier between layers in the edge region is shallower than in the bulk region. This barrier difference leads to an inter-layer tunneling strength which is stronger in the edge than in the bulk. Moreover, we need to satisfy two additional conditions: (1) to have a smooth torus, the on-site energy in the edge and the bulk regions should be the same, and (2) this on-site energy

should be smaller than the potential in the empty space, so that atoms are trapped in the designated square annulus. To find on-site energies in these conditions, we should include the zero point energies in the effective potentials as well. Then, these requirements can be summarized as

$$V_{\mathrm{B}}^{(0)} + \frac{\hbar\omega_B}{2} = V_{\mathrm{E}}^{(0)} + \frac{\hbar\omega_{\mathrm{E}}}{2} < V_{\mathrm{S}} \tag{2.3}$$

where the zero point energy of the harmonic confinements are

$$\frac{1}{2}\hbar\omega_{\mathrm{B/E}} = \frac{1}{2}\hbar \sum_{s=x,y,z} \sqrt{m^{-1}\, \partial_s^2 V(\mathbf{r})|_{\mathbf{r}\in \mathrm{B/E}}}. \tag{2.4}$$

To evaluate this, we consider the total dipole potential $V(\mathbf{r}) = V_{xy}(x,y) + V_z(\mathbf{r})$, where the horizontal dipole potential is $V_{xy}(x,y) = V_0\{\cos^2(k_x x) + \cos^2(k_y y)\}$ and $V_z(\mathbf{r})$ is given in Eq. (2.2). While it is not obvious to find a set of parameters satisfying these conditions simultaneously, it is possible to satisfy Eq. (2.3) by tuning $m, k_x, k_y, k_z, q_z, V_0, V_{\mathrm{red}}, \mathcal{E}_+, \mathcal{E}_{\mathrm{E}}, \mathcal{E}_{\mathrm{B}}, f_0$. For example, the parameters in Fig. 2.2 fulfill these requirements (see Sec. 2.7).

To verify that our beam design leads to the desired optical lattice, we numerically evaluate the total dipole potential for Rb^{87} atoms [Figs. 2.2(a) and 2.2(b)]. We approximately evaluate the tunneling strengths by solving the Schrödinger equation over the region containing each pair of the nearest neighboring sites (see Sec. 2.7). Fig. 2.2(c) shows that it is possible to suppress inter-layer tunneling in the bulk, while simultaneously setting inter-layer tunneling in the edge and intra-layer tun-

neling everywhere to be non-vanishing. Here, for boundaries between the different regions, we use more realistic resolution limited potentials (see Sec. 2.5) instead of the step functions in Eq. (2.1).

Once our scheme for torus construction is realized, it is straightforward to extend the scheme to genus-g surfaces [Fig. 2.1(b)]. The only requirement is to puncture more holes in the beam shape, which requires no higher resolution in beam-shaping than puncturing a single hole. On such genus-g surfaces, one can explore richer topological physics as we discuss later.

2.3 Quantized Supercurrents in Two Cycles

To demonstrate how topology plays a non-trivial role in the dynamics of ultracold atoms on a torus surface, we numerically investigated the hydrodynamics of weakly interacting bosonic superfluids. Previously, in a ring geometry, it has been experimentally demonstrated that the flow of supercurrents is quantized along the single quantization axis [110, 121]. The quantization of supercurrent results from the fact that wavefunction of the atomic condensate should be single-valued and its phase should be compact on a closed cycle. More interestingly, in the torus setting, there are two intersecting non-contractible cycles [Fig. 2.3(a)] which allow supercurrents to be quantized separately along each. In particular, the vorticity, which is defined as

$$v_i = \frac{1}{2\pi\rho_{\text{avg}}} \oint_{\text{cycle } i} \text{Im}\left(\psi^* \nabla \psi\right) \cdot \mathbf{dl} \quad (i = 1, 2), \tag{2.5}$$

is quantized to an integer, up to a small finite-size fluctuation. Here, ρ_{avg} is the average condensate density and $\psi(\mathbf{r})$ is the condensate wavefunction. To generate the supercurrents with non-zero vorticities, we stir the atomic condensate with an extra dipole potential [122]. In particular, we prepare a blue-detuned, focused beam and move it along each non-contractible cycle to generate the supercurrent flow in the stirring direction [Fig. 2.3(a)]. The supercurrent flows can be detected through established methods, such as time-of-flight imaging [121].

To specifically show the quantization along each cycle, we numerically simulate these stirring procedures [Fig. 2.3(b)]. In the weakly interacting and tight-binding regime, atomic dynamics in our optical lattice can be described in the mean-field approximation,

$$\begin{aligned} i\hbar\partial_t\psi_j^{\uparrow/\downarrow} &= -J\sum_{k;|k-j|=1}\psi_k^{\uparrow/\downarrow} - \left(J\psi_j^{\downarrow/\uparrow}\right)\delta_{j\in\text{edge}} \\ &\quad + \left\{V^{\uparrow/\downarrow}(\mathbf{r}_j,t) - \mu + U\left|\psi_j^{\uparrow/\downarrow}\right|^2\right\}\psi_j^{\uparrow/\downarrow}, \end{aligned} \tag{2.6}$$

where ψ_j^l is the condensate wavefunction at site j on layer l ($l = \uparrow$ / $\downarrow$ for the upper/lower layer). Here, $|k-j|$ indicates the distance between site k and j and $\delta_{j\in\text{edge}} = 1$ if j belongs to the edge region (0 otherwise). J is the tunneling strength, U is the on-site interaction energy, V^l is the stirring potential on layer l and μ is the chemical potential. Superfluid remains stable if the stirring is slower than the sound speed, $\sqrt{\mu/m}$ [123]. This dynamics can be simulated with the numerical methods for the Gross-Pitaevskii equation [124–126]. See Sec. 2.8 for further details.

In the simulation, we verify that the stirred superfluid exhibits the quantized

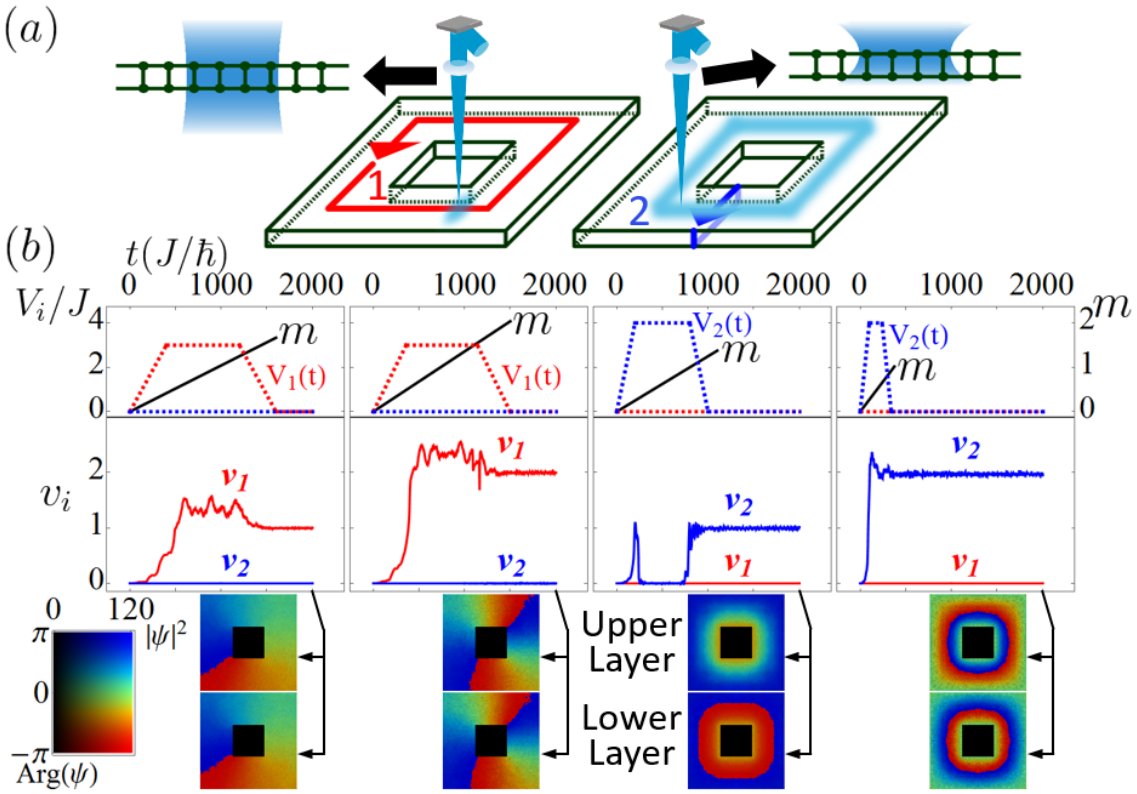

Figure 2.3: (a) A scheme to generate supercurrents in two cycles. A focused, blue-detuned laser beam acts as a stirrer along each cycle, namely, cycle 1 and 2. Note that the stirrer along cycle 2 is focused on the upper layer. A uniform condensate is loaded on the torus initially, then the stirring potential along cycle 1 (V_1) or cycle 2 (V_2) is ramped up and down. (b) Quantization of vorticity in two cycles. Dotted curves in the upper plots indicate the ramping sequences of V_1 and V_2. Solid lines in the upper plots indicate the number of completed cycles (m) in the stirring process. The lower plots show vorticities (v_i) changing over time. Steady-state wavefunctions of the different sequences are shown below.

vorticity along each cycle of stirring [Fig. 2.3(b)]. We also see that this vorticity increases with the stirring speed. As expected, the evaluated vorticity along each cycle coincides with the wavefunction winding numbers [Fig. 2.3(b)]. Also, we observe the creation and annihilation of vortex-antivortex pairs during the increment of vorticity (see Sec. 2.8).

2.4 Topological Degeneracy in FQH States

Our construction allows one to investigate the dynamics of strongly interacting ultracold atoms on a torus. As an example, we study a bosonic FQH model, which could be realized by laser-assisted tunneling [7, 8]. Specifically, the lattice FQH Hamiltonian for bosonic atoms on our torus can be written as

$$\begin{aligned} H = & \sum_{n,m} \sum_{l=\uparrow,\downarrow} \left(\frac{U}{2} a_{n,m}^{l\dagger\ 2} a_{n,m}^{l\ 2} - J e^{i\theta_x^l} a_{n+1,m}^{l\dagger} a_{n,m}^{l} - J e^{i\theta_y^l} a_{n,m+1}^{l\dagger} a_{n,m}^{l} + \text{H.c.} \right) \\ & - \sum_{(n,m)\in \text{edge}} \left(J' a_{n,m}^{\uparrow\dagger} a_{n,m}^{\downarrow} + \text{ H.c.} \right), \qquad (2.7) \\ \theta_x^{\uparrow/\downarrow}(n,m) = & \frac{(n \mp m)\phi}{2}, \ \theta_y^{\uparrow/\downarrow}(n,m) = \frac{(m \pm n)\phi}{2}. \end{aligned}$$

Here, $a_{n,m}^{l}$ annihilates an atom at site (n, m) on layer l. J and J' are the effective intra- and inter-layer tunneling strengths, and U is the on-site interaction energy. With proper size of square annulus, the synthetic magnetic flux per unit cell can be set to ϕ (see Sec. 2.10). To obtain the tunneling phases in Eq. (2.7), we apply a magnetic field in such a way that the Zeeman energy gradient becomes Δ_x (Δ_y) per site in the x (y) direction. Then we apply Raman beams whose detuning matches with Δ_x (Δ_y) to induce the tunneling in the x (y) direction [Fig. 2.4(a)]. Since the surface orientations of two layers are opposite to each other, the required tunneling phases in each layer should be different as well. This can be achieved by targeting the different Raman beams on the different layers [Fig. 2.4(b)]. To do so, we use a triplet of beams for each tunneling term, namely $T_{\mathbf{i}=\mathbf{1}\sim\mathbf{4}} \equiv \{\mathbf{i}, \mathbf{i}+, \mathbf{i}-\}$. Here, the beam $\mathbf{i}$ ($\mathbf{i}\pm$) has the frequency ω_i ($\omega_{i\pm}$) and the wavevector $\mathbf{k_i}$ ($\mathbf{k_{i\pm}}$). In this triplet,

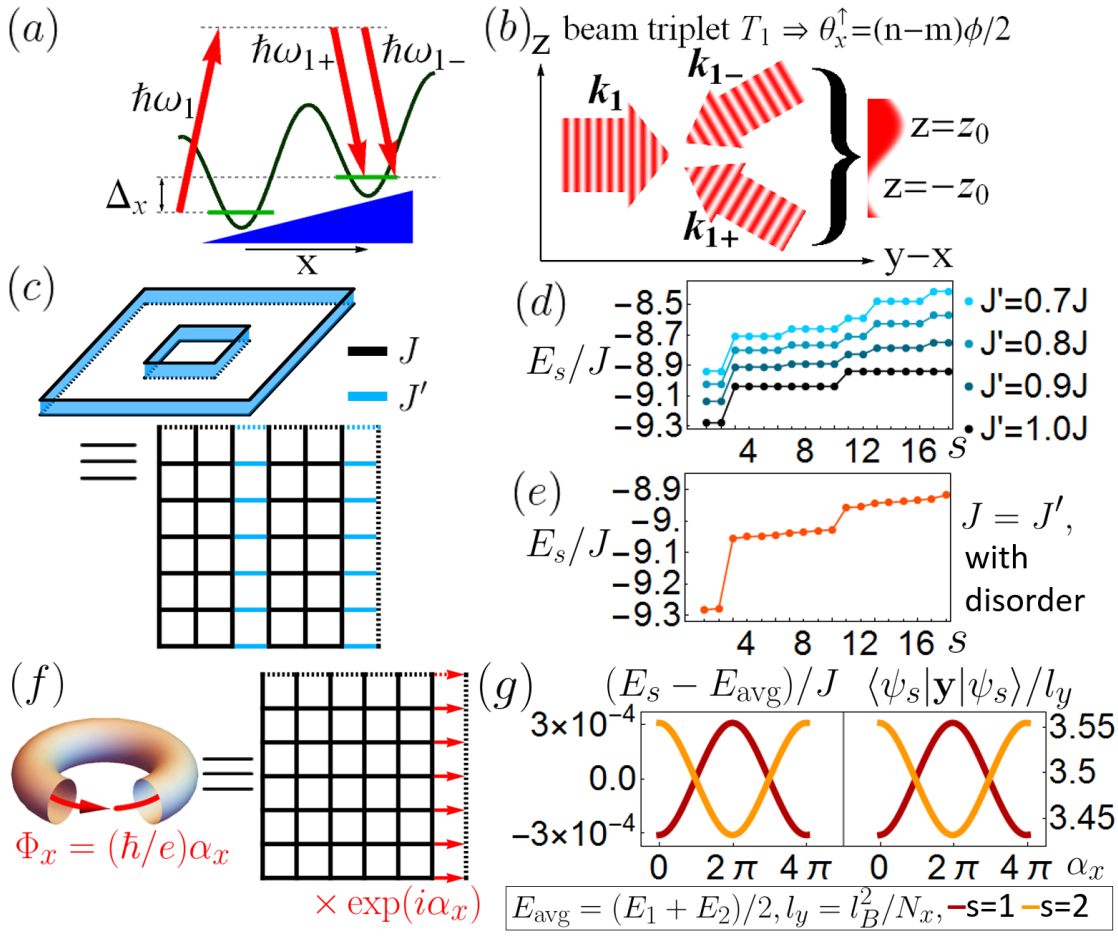

Figure 2.4: (a),(b) A scheme for FQH Hamiltonian. Different Raman beam triplets $T_{\mathbf{i=1\sim4}}$ give the different tunneling phases in Eq. (2.7). Schematic beam configuration of $T_{\mathbf{1}}$ is shown for an example. Zeeman eneargy difference Δ_x (Δ_y) in the x (y) direction is matched with detuning of Raman beams in triplets $T_{\mathbf{i=1,3}}$ ($T_{\mathbf{i=2,4}}$) to give tunneling terms in the same direction. To address each layer independently, beam $\mathbf{i}+$ and $\mathbf{i}-$ in triplet $T_{\mathbf{i=1,2}}$ ($T_{\mathbf{i=3,4}}$) destructively interfere at lower (upper) layer. (c) Exact diagonalization of FQH Hamiltonian for 3 hardcore bosonic atoms on a 6×6 square lattice ($N_x = N_y = 6$) with periodic boundary conditions and $\phi = \pi/3$, magnetic length $l_B \equiv \sqrt{2\pi/\phi}$. E_s ($|\psi_s\rangle$) indicates the s-th lowest eigenenergy (eigenstate). (d) Energy spectrums with distinct intra-layer (J) and inter-layer (J') tunnelings. (e) Spectrum with a random disorder of scale $0.05J$. Energy splitting between the ground states is $5 \times 10^{-3} J$. (f) Inserting flux Φ_x through the handle of torus is equivalent to the boundary condition with twist angle α_x. (g) With additional potential $V(y) = (0.01J/N_y)y$, the spectral flows in α_x can be detected by measuring the y-coordinates of the states.

the beams $\mathbf{i}+$ and $\mathbf{i}-$ have the same x and y components and have the opposite z components in the wavevectors. These two beams then form a standing wave in z direction. By aligning the beams $\mathbf{i}+$ and $\mathbf{i}-$ to destructively interfere at the lower (upper) layer, the beam triplet $T_{\mathbf{i}}$ can solely address the upper(lower) layer. In a rotating frame, these Raman beams result in the effective tunneling terms given in Eq. (2.7) (see Sec. 2.9).

We numerically investigated the topological degeneracy in FQH system on the torus. In particular, FQH systems with filling fraction $\nu = 1/m$ on a torus surface have m-fold ground-state degeneracies [72,112]. To numerically diagonalize the FQH Hamiltonian, we put the upper layer part of Hamiltonian in Eq. (2.7) on a 6×6 square lattice with periodic boundary conditions [Fig. 2.4(c)]. For filling fraction $\nu = 1/2$, we have the anticipated two-fold ground-state degeneracy [Fig. 2.4(d)].

To examine the robustness of this degeneracy, we calculate the energy spectrum for varying inter-layer tunnelings (J') and a disorder potential [Figs. 2.4(d) and 2.4(e)]. We can see the two-fold degeneracy persists within slight ground energy splittings which are smaller than the tunneling strengths, the disorder scale, and the excitation gap. Therefore, this topological degeneracy in a small FQH system is robust against potential experimental imperfections.

Furthermore, one can measure the topological degeneracy by measuring the spectral flow during the synthetic magnetic flux insertion though the handle of the torus. As shown in Fig. 2.4(f), the insertion of flux Φ_x is equivalent to the boundary condition $\psi(x + N_x, y) = \psi(x, y) \exp(i\alpha_x)$ where $\alpha_x = (e/\hbar)\Phi_x$. For $\nu = 1/m$, the spectral flow of each ground state shows the $2m\pi$-periodicity in

α_x [127, 128]. To observe this periodicity, we can introduce a small energy splitting by applying a potential $V(y) \propto y$. Such a spectral flow is manifested in the y-coordinate expectation values of the ground states (see [Fig. 2.4(g)], Sec. 2.11). This average atom position can be experimentally detected through the density measurements.

2.5 Validity of Model Laser Beams

In our design of optical lattice, we assume each laser beam maintains the beam shape in their propagating direction. While such assumption is reasonable for the plane wave beams, the model beam shape in Eq. (2.1) with this assumption would violate Maxwell's laws. If we modify this model beam to satisfy Maxwell's laws, the beam shape should change as the beam propagates. For this modified beam to be a good approximation of Eq. (2.1), we should check the change of beam shape is modest over the region in which our bilayer system is located. On the other hand, beam shaping with a high precision requires experimental schemes to focus laser beams in the targeted area. To make sure that our beam design is experimentally feasible, we should check if the highest numerical aperture (NA) required in our design is achievable with the current technology.

To construct an approximation of the $-z$ propagating beam ($\mathbf{E}_-$) in Eq. (2.1), in a way that Maxwell's laws are satisfied, we reconstruct the 3D intensity profile of this model beam with Hermite-Gaussian (HG) decomposition (Fig. 2.5). Each HG

mode has the form of [129]

$$\begin{aligned}
\mathcal{E}_{lm}(x,y,z) &= \mathcal{E}_0 \frac{w_0}{w(z)} H_l\left(\frac{\sqrt{2}x}{w(z)}\right) H_m\left(\frac{\sqrt{2}y}{w(z)}\right) \exp\left(-\frac{x^2+y^2}{w^2(z)}\right) \\
&\quad \times \exp\left(-i\frac{\pi(x^2+y^2)z}{\lambda(z^2+(\pi w_0^2/\lambda)^2)} - i\frac{2\pi z}{\lambda} + i\eta(z)\right), \\
w(z) &= \sqrt{w_0^2 + (\lambda z/\pi w_0)^2}, \\
\eta(z) &= (l+m+1)\tan^{-1}\left(\frac{z^2}{z^2+(\pi w_0^2/\lambda)^2}\right).
\end{aligned} \tag{2.8}$$

Here, $H_l(x)$ is the lth order Hermite polynomial, λ is the wavelength of the beam and w_0 is the beam waist radius. Since each mode is a solution of the electromagnetic wave equation, any superposition of concentric and confocal HG modes satisfy Maxwell's laws. In particular, we consider the superposition such that

$$|\mathbf{E}_-(\mathbf{r},t)|_{z=0,t=0} = \sum_{l,m=0}^{M} C_{lm}\mathcal{E}_{lm}(x,y,0). \tag{2.9}$$

Since $|\mathbf{E}_-|$ is an even function in x and y, we can omit modes with odd l or odd m. While full HG decomposition requires $M \to \infty$, we set $M = 120$ to keep the required NA of the beams experimentally accessible. We also need to replace the step functions in $|\mathbf{E}_-|$ with smoother functions. In particular, we use sinusoidal functions in the overlapping region between the different regions. For example, if

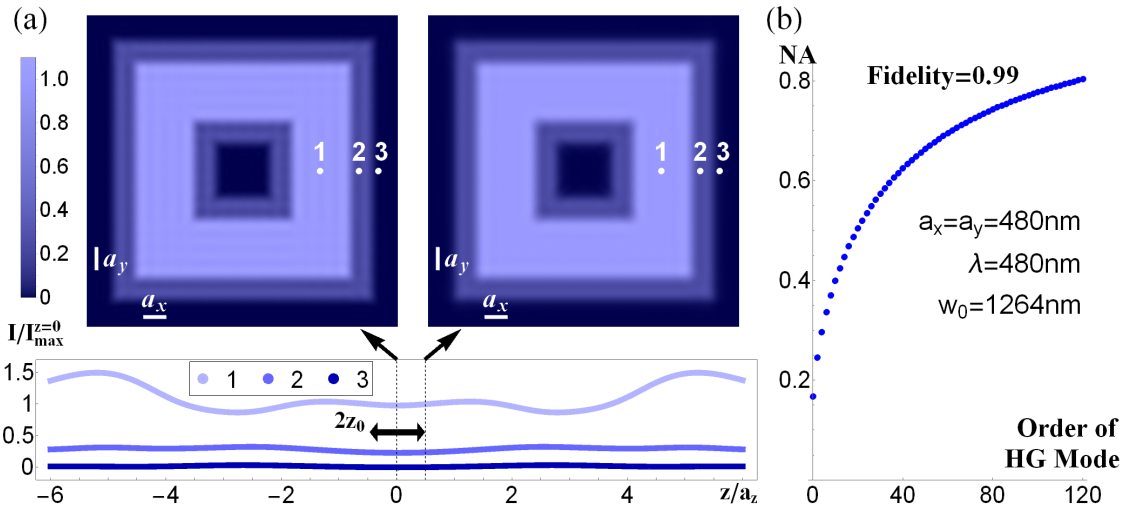

Figure 2.5: (a) Intensity profile of the reconstructed beam through HG decomposition. Here, $I_{\max}^{z=0}$ indicates the maximum intensity at $z = 0$. The beam shape is almost maintained over $|z| \leq z_0$, where the bilayer system are located. (b) Numerical apertures of HG modes used in the reconstructed bean, which ranges from 0.17 to 0.80. We used HG modes up to the order of 120, while only the even modes are used for the symmetry reason.

the cut is located at $x = 0$, beam amplitude changes as

$$\mathcal{E}(x) = \begin{cases} \mathcal{E}_1 & -a_x/2 < x < -ba_x/2 \\ (\mathcal{E}_1 - \mathcal{E}_2)\cos^2\{(\pi x)/(2ba_x) + \pi/4\} & |x| < ba_x/2 \\ \mathcal{E}_2 & ba_x/2 < x < a_x/2 \end{cases} \tag{2.10}$$

where $b = 0.7$ between the edge and the empty space, and $b = 0.4$ for the rest of boundaries. To carry out the numerical evaluation in Fig. 2.5, we use $\lambda = 480$ nm and $w_0 = 1264$ nm over the lattice with $a_x = a_y = 480$ nm. As shown in Fig. 2.5(a), the intensity profile of the reconstructed beam almost maintains its beam shape over the region of our bilayer system. Therefore, one can construct an approximation of the model beam that satisfies Maxwell's laws.

To see if this reconstructed beam in Fig. 2.5(a) is achievable with reasonable

NA, we calculate numerical aperture of each HG mode used in the reconstructed beam. Since Eq. (2.8) is separable in $x/w(z)$ and $y/w(z)$, we can define the radius of the mode l, $r_l(z)$, in a way that the intensity proportion of the HG beam of mode l, m that passes through the ellipse $\{\mathbf{r}|x^2/r_l^2(z) + y^2/r_m(z)^2 \leq 1\}$ is equal to the certain fidelity. By setting this fidelity to be 0.99, we get

$$\frac{\int_{-r_l(z)}^{r_l(z)} H_l^2\left(\frac{\sqrt{2}x}{w(z)}\right)\exp\left(-\frac{2x^2}{w^2(z)}\right)dx}{\int_{-\infty}^{\infty} H_l^2\left(\frac{\sqrt{2}x}{w(z)}\right)\exp\left(-\frac{2x^2}{w^2(z)}\right)dx} = \sqrt{0.99} \tag{2.11}$$

Since $r_l(z)$ is proportional to $w(z) = \sqrt{w_0^2 + (\lambda z/\pi w_0)^2}$, $r_l(z) \sim \alpha_l z$ for $z \gg w_0^2/\lambda$. Then the numerical aperture for the lth mode is given by $\mathrm{NA}_l = \sin(\tan^{-1}\alpha_l) = (1+\alpha_l^{-2})^{-1/2}$, which is evaluated in Fig. 2.5(b). As shown in the figure, the numerical apertures of HG modes used in Eq. (2.9) range from NA = 0.17 to NA = 0.80. Since high-order HG beams are already implemented with NA=0.8 [94] and the focused beam with NA=0.92 for addressing of ultracold atoms is experimentally reported [130], the reconstructed beam in Fig. 2.5 is experimentally promising.

We also use the focused laser beams used in supercurrent generation procedure (Fig. 2.3) . Since the focused laser beam with NA=0.92 is reported [130], we use this number as the benchmark for the stirring laser beams. With the NA=0.92 and the wavelength $\lambda = 480$ nm, the Gaussian beam has the waist radius $w_0 = \lambda/\pi(\mathrm{NA}^{-2} - 1)^{0.5} = 65$ nm, which is far smaller than the lattice spacing in the numerical evaluation in Fig. 2.2. This tells that the focused beam used in stirring in the cycle 1 is experimentally feasible. For the stirrer along the cycle 2, we need to obtain enough imbalance in intensities of the focused laser beam reaching upper and

lower layers. In our numerical evaluation of the optical lattice, the distance between the upper and lower layers is $z_0 = 120$ nm. If this Gaussian beam is focused at one of the layers, the central laser intensity at the other layer is

$$I_{z_0} = I_0 \left\{ 1 + \left(\frac{\lambda z_0}{\pi w_0^2} \right)^2 \right\}^{-1} = (0.051) I_0, \tag{2.12}$$

where I_0 is the central laser intensity at the focused layer. This provides a lower bound of the intensity ratio $\gamma = I_{z_0}/I_0$ which we introduce and compare later.

2.6 Conditions for On-site energies

In our torus construction, we have following set of independent parameters: $m, k_x, k_y, k_z, q_z, V_0, V_{\text{red}}, \mathcal{E}_+, \mathcal{E}_{\text{E}}, \mathcal{E}_{\text{B}}$ and f_0. Yet, the required conditions for the on-site energies stated in Eq. (2.3) are not represented in these parameters directly. To express Eq. (2.3) with this set of parameters, we first express the overall dipole potential as

$$\begin{aligned} V(\mathbf{r}) &= V_0\{\cos^2(k_x) + \cos^2(k_y)\} - V_{\text{red}} \cos^2(q_z z) + V_b(\mathbf{r}), \\ V_b(\mathbf{r}) &= \begin{cases} 4 f_0 \mathcal{E}_+ \mathcal{E}_{\text{B}} \cos^2(k_z z) + f_0(\mathcal{E}_+ - \mathcal{E}_{\text{B}})^2 & \text{bulk} \\ 4 f_0 \mathcal{E}_+ \mathcal{E}_{\text{E}} \cos^2(k_z z) + f_0(\mathcal{E}_+ - \mathcal{E}_{\text{E}})^2 & \text{edge} \\ f_0 \mathcal{E}_+^2 & \text{empty space} \end{cases}, \end{aligned} \tag{2.13}$$

by using $V_{\mathrm{B/E}} = 4f_0\mathcal{E}_+\mathcal{E}_{\mathrm{B/E}}$, $V^{(0)}_{\mathrm{B/E}} = f_0(\mathcal{E}_+ - \mathcal{E}_{\mathrm{B/E}})^2$, and $V_{\mathrm{S}} = f_0\mathcal{E}_+^2$. Now the zero point energy of the harmonic confinements can be expressed as

$$\begin{aligned}
\frac{\hbar}{2}\omega_{\mathrm{B/E}} &= \frac{\hbar}{2}\omega_{\mathrm{B/E}}(m, k_x, k_y, k_z, q_z, V_0, V_{\mathrm{red}}, \mathcal{E}_+, \mathcal{E}_{\mathrm{E}}, \mathcal{E}_{\mathrm{B}}, f_0) \\
&= \frac{\hbar}{2}\sum_{s=x,y,z}\sqrt{m^{-1}\,\partial_s^2 V(\mathbf{r})|_{\mathbf{r}\in\mathrm{B/E}}} \\
&= \hbar(k_x + k_y)\sqrt{\frac{V_0}{2m}} \\
&\quad +\hbar\sqrt{\frac{q_z^2 V_{\mathrm{red}}}{2m}\cos(2q_z z_{\mathrm{B/E}}) - \frac{2k_z^2 f_0\mathcal{E}_+\mathcal{E}_{\mathrm{B/E}}}{m}\cos(2k_z z_{\mathrm{B/E}})},
\end{aligned} \tag{2.14}$$

where $z_{\mathrm{B/E}}$ is the smallest positive number satisfying

$$q_z V_{\mathrm{red}}\sin(2q_z z_{\mathrm{B/E}}) = 4k_z f_0\mathcal{E}_+\mathcal{E}_{\mathrm{B/E}}\sin(2k_z z_{\mathrm{B/E}}). \tag{2.15}$$

Now Eq. (2.3) becomes

$$f_0(\mathcal{E}_+ - \mathcal{E}_{\mathrm{B}})^2 + \frac{\hbar}{2}\omega_{\mathrm{B}} = f_0(\mathcal{E}_+ - \mathcal{E}_{\mathrm{E}})^2 + \frac{\hbar}{2}\omega_{\mathrm{E}} < f_0\mathcal{E}_+^2, \tag{2.16}$$

and it is completely determined by the forementioned set of independent parameters.

We also show that the parameters used in Fig. 2.2 satisfy these conditions. We evaluate the on-site energy for each site and verify that it is the same for all sites (Fig. 2.6). As shown in the figure, on-site energies in the bulk and the edge are matched so that atoms can tunnel to each other within the same layer. By doing so, one can make the torus surface smooth. Also, this on-site energy is lower than the dipole potential in the empty space, which indicates that the leakage to the empty

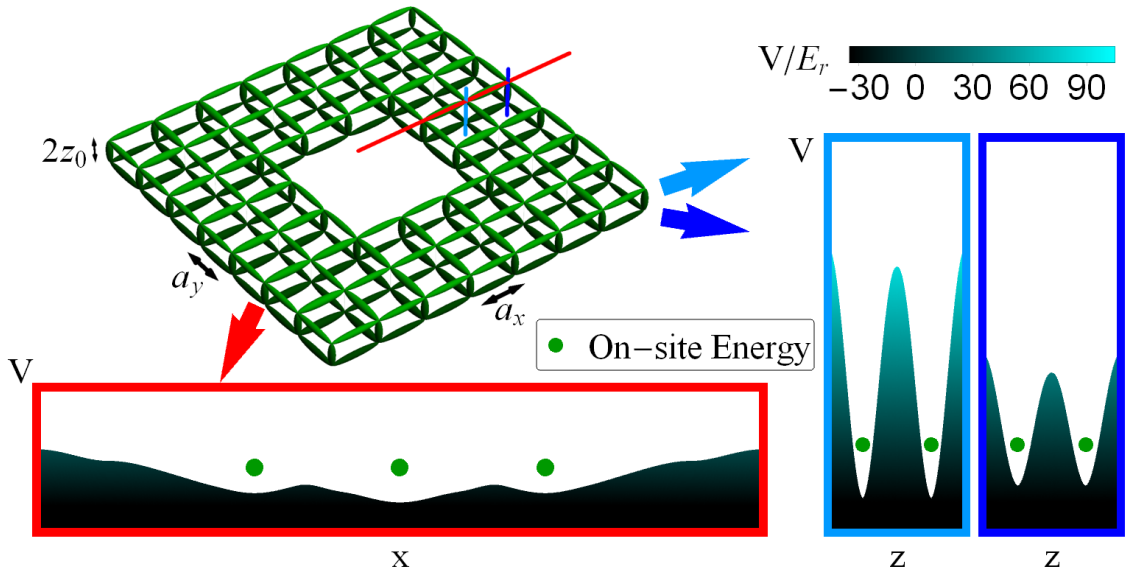

Figure 2.6: On-site energy presented with the dipole potential along several lines in the optical lattice. On-site energies in the bulk and the edge are set to be equal, which leads to a smooth torus surface.

space is energetically prevented.

2.7 Numerical Evaluation of Tunneling Strength

To find the tunneling strength between two neighboring sites, we use the isolated two-site model for this pair of sites. If E_1 and E_2 are on-site energy site 1 and 2 in this pair, the model Hamiltonian is given by $\begin{pmatrix} E_1 & -J^* \\ -J & E_2 \end{pmatrix}$, whose eigenenergies are given by $\epsilon_\pm = (E_1 + E_2)/2 \pm \sqrt{|J|^2 + (E_1 - E_2)^2/4}$. Conversely, the tunneling strength $|J|$ is given by

$$|J| = \frac{1}{2}\sqrt{(\epsilon_+ - \epsilon_-)^2 - (E_1 - E_2)^2}. \tag{2.17}$$

To evaluate E_1, E_2, and $\epsilon_\pm$, we numerically solve the 3D Schrodinger equa-

tions. For example, for two sites located at $(x, y, z) = (-a_x/2, 0, 0)$ and $(x, y, z) = (a_x/2, 0, 0)$, we take points in the real space as

$$x_n = -a_x + (n - 1/2)\delta x, \quad y_n = -a_y/2 + (n - 1/2)\delta y,$$
$$z_n = -a_z/2 + (n - 1/2)\delta z, \tag{2.18}$$

for $n \in \mathbb{N}$ such that

$$X_1 = \{x_n | n \leq N_x\}, X_2 = \{x_n | N_x < n \leq 2N_x\}, Y = \{y_n | n \leq N_y\}, Z = \{z_n | n \leq N_z\},$$

where $\delta x = a_x/N_x$, $\delta y = a_y/N_y$, and $\delta z = a_z/N_z$. Denote the position $(x, y, z) = (x_i, y_j, z_k)$ as ijk. Now the discrete Schrodinger equation gives the following Hamiltonian:

$$H_{i'j'k',ijk} = \frac{\hbar^2}{m} \times \begin{cases} -(1/2)\delta x^{-2} & \text{if } |i' - i| = 1,\ j' = j,\ k' = k \\ -(1/2)\delta y^{-2} & \text{if } i' = i,\ |j' - j| = 1,\ k' = k \\ -(1/2)\delta z^{-2} & \text{if } i' = i,\ j' = j,\ |k' - k| = 1 \\ \delta_0^{-2} + V(x_i, y_j, z_k) & \text{if } i' = i,\ j' = j,\ k' = k \\ 0 & \text{else} \end{cases},$$
$$\text{where} \quad \delta_0^{-2} = \delta x^{-2} + \delta y^{-2} + \delta z^{-2}. \tag{2.19}$$

Here, $V(x, y, z)$ is the dipole potential introduced in Eq. (2.2). Now E_1 (E_2) is the lowest eigenenergy obtained by numerically diagonalizing this H over $X_1 \times Y \times Z$ ($X_2 \times Y \times Z$), while ϵ_- and ϵ_+ are the first and second lowest eigenenergies obtained

by numerically diagonalizing H over $(X_1 \cup X_2) \times Y \times Z$. From Eq. (2.17), we can evaluate the tunneling strength between the two targeted site.

This method can be applied to every pair of neighboring sites, as presented in Fig. 2.2. For the tunneling strengths in the figure, we use $N_x = N_y = N_z = 60$ in the evaluation. With the dipole potential presented in Fig. 2.2, in the unit of recoil energy $E_r = \hbar^2 k_x^2/2m$, calculated tunneling strengths are given as follows; the intra-layer tunneling strength between two bulk sites is $0.032E_r$, the intra-layer tunneling strength between an edge site and a bulk site is $0.041E_r$, the inter-layer tunneling strength between two edge sites is $0.036E_r$, and the inter-layer tunneling strength between two bulk sites is $0.002E_r$.

2.8 Numerical Simulation of Dynamics in Condensate with Stirring Potentials

As presented in Eq. (2.6), in the mean field limit, the dynamics of condensate wavefunction is determined by

$$\begin{aligned} i\hbar\partial_t \psi_j^{\uparrow/\downarrow} &= -J \sum_{k;|k-j|=1} \psi_k^{\uparrow/\downarrow} - \left(J\psi_j^{\downarrow/\uparrow}\right) \delta_{j\in\text{edge}} \\ &\quad + \left\{ V^{\uparrow/\downarrow}(\mathbf{r}_j, t) - \mu + U \left|\psi_j^{\uparrow/\downarrow}\right|^2 \right\} \psi_j^{\uparrow/\downarrow}, \end{aligned} \tag{2.20}$$

where j runs over sites in each layer. Stirring potential $V^l(\mathbf{r}_j, t) = V^l(x, y, t) = V^l(r, \phi, t)$ ($l = \uparrow / \downarrow$ for upper/lower layer) in this equation is given by

$$\begin{aligned}
&\text{Stirring along cycle 1:} \\
&V^{\uparrow}(\mathbf{r}_j, t) = V_1(t) e^{-[(x-X(t))^2+(y-Y(t))^2]/2d_1^2} \\
&V^{\downarrow}(\mathbf{r}_j, t) = V_1(t) e^{-[(x-X(t))^2+(y-Y(t))^2]/2d_1^2} \\
&\text{Stirring along cycle 2:} \\
&V^{\uparrow}(\mathbf{r}_j, t) = V_2(t)(e^{-(r-R_A(t))^2/2d_2^2} + \gamma e^{-\gamma(r-R_B(t))^2/2d_2^2}) \\
&V^{\downarrow}(\mathbf{r}_j, t) = V_2(t)(\gamma e^{-\gamma(r-R_A(t))^2/2d_2^2} + e^{-(r-R_B(t))^2/2d_2^2})
\end{aligned} \qquad (2.21)$$

Here, $(X(t), Y(t)) = R_0(\cos\frac{2\pi t}{\tau_1}, \sin\frac{2\pi t}{\tau_1})$, $R_A(t) = R_1 + (R_2 - R_1)\left(\mathrm{mod}(\frac{t}{\tau_2}, 1)\right)$ and $R_B(t) = R_1 + (R_2 - R_1)\,(\mathrm{mod}(-t/\tau_2, 1))$. In each stirring sequence in Fig. 2.3(b), $V_i(t)(i = 1, 2)$ ramps up from 0 to $V_{\mathrm{max},i}$, then remains at $V_{\mathrm{max},i}$, and finally ramps down to 0. Stirring periods are $\tau_1 = 1200\hbar/J$ and $\tau_1 = 920\hbar/J$ for the first two graphs and $\tau_2 = 1000\hbar/J$ and $\tau_2 = 460\hbar/J$ for the last two graphs.

In the simulations presented in Fig. 2.3, we consider a torus embedded in two layers of 108×108 square lattice ($a_x = a_y = a$) with a 36×36 puncture in the middle. Numerical parameters used in this simulation are $U = 0.0041J, \mu = 27.4J, V_{\mathrm{max},1} = 3.0J, V_{\mathrm{max},2} = 4.0J, R_0 = 36.0a, R_1 = 32.0a, R_2 = 128.0a, d_1 = 12.0a, d_2 = 4.0a, \gamma = 0.2$. Note that γ used in this simulation is well above the lower bound obtained in Eq. (2.12).

By observing the course of dynamics of the atomic condensate more closely, one can find that each addition of vorticity is accompanied by a particular procedure of creating, moving, and annihilating vortex-antivortex pairs. For example, the

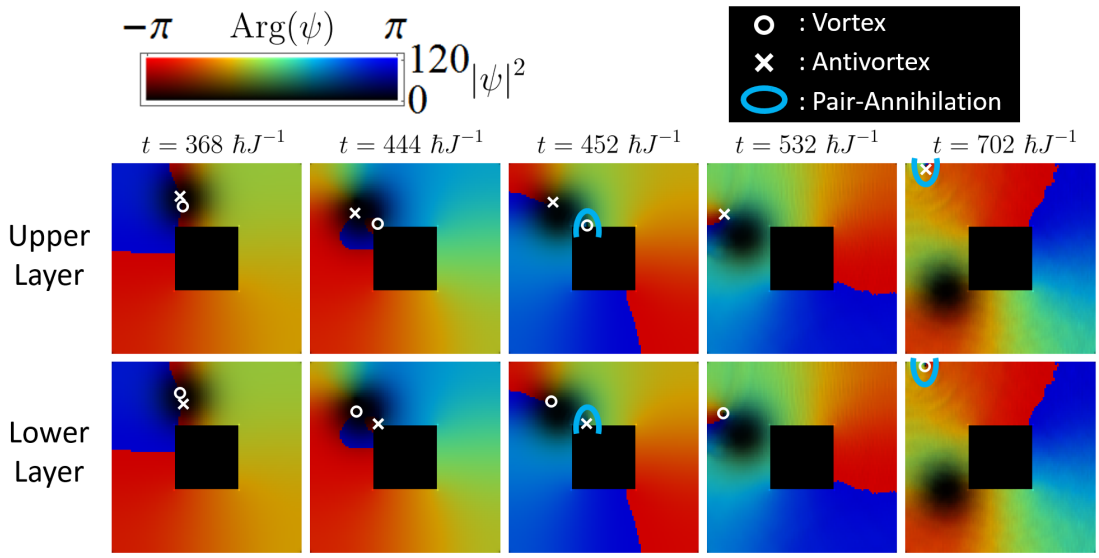

Figure 2.7: Condensate wavefunction during the stirring procedure presented in the leftmost graph in Fig. 2.3(b). Determination of vortex and antivortex is opposite in upper and lower layers due to their opposite orientations of surfaces.

procedure of vorticity addition of the leftmost graph in Fig. 2.3(b) is illustrated in Fig. 2.7. As shown in the figure, once vortex-antivortex pairs are created on the upper and lower layers, the vortex (antivortex) in the upper (lower) layer moves toward the inner edge, while the antivortex (vortex) in the upper (lower) layer moves toward the outer edge. Around each edge, newly paired vortex and antivortex annihilate with each other. This is topologically equivalent to the operation that moves an antivortex along the loop 2 once, which results in the addition of a unit vorticity to the loop 1. Similarly, an operation that moves an antivortex along the loop 1 once adds a unit vorticity to the loop 2.

2.9 Laser-Assisted Tunneling Terms for Quantum Hall Hamiltonian

Here we introduce the expression of laser-assisted tunneling terms based on the approach of [8]. To adopt the laser-assisted tunneling in the horizontal direction, we may apply a magnetic field with linear tilts in x and y direction to obtain additional potential $\Delta_x(x/a_x) + \Delta_y(y/a_y)$. We set $\Delta_y \neq \Delta_x$. For the tight-binding model with Wannier basis $\{|w_{nm}\rangle\}$ and bare tunneling strength J, overall Hamiltonian with the additional potential is

$$\begin{aligned} H_0 &= \sum_{n,m\in\mathbb{Z}} \Big\{ (n\Delta_x + m\Delta_y) \left|w_{nm}\right\rangle \left\langle w_{nm}\right| \\ &\qquad - J\left(\left|w_{(n+1)m}\right\rangle \left\langle w_{nm}\right| + \left|w_{n(m+1)}\right\rangle \left\langle w_{nm}\right| + \text{H.c.} \right) \Big\} . \end{aligned} \tag{2.22}$$

This Hamiltonian can be diagonalized with Wannier-Stark basis $\{|nm\rangle\}$, which is described by [131]

$$|nm\rangle = \sum_{r,s\in\mathbb{Z}} J_r\left(\frac{2J}{\Delta_x}\right) J_s\left(\frac{2J}{\Delta_y}\right) \left|w_{(n+r)(m+s)}\right\rangle , \tag{2.23}$$

where J_r is the Bessel function of the 1st kind with order r. It is straightforward to show that $H_0 |nm\rangle = (n\Delta_x + m\Delta_y) |nm\rangle$ with the aid of recurrence relation of Bessel function, $J_{r-1}(x) + J_{r+1}(x) = 2rJ_r(x)/x$.

Now we apply pairs of Raman beams $\mathbf{p}_1$ and $\mathbf{p}_2$ with detuning $c(|\mathbf{p}_1| - |\mathbf{p}_2|) = \Delta_x/\hbar$, $\mathbf{q}_1$ and $\mathbf{q}_2$ with detuning $c(|\mathbf{q}_1| - |\mathbf{q}_2|) = \Delta_y/\hbar$. Then two-photon process between the two beams generate a time-varying dipole potential $V_{\text{dip}}(x, y, t) =$

$\Omega_x \cos(\delta\mathbf{p}\cdot\mathbf{r} - \Delta_x t/\hbar - \theta_x) + \Omega_y \cos(\delta\mathbf{q}\cdot\mathbf{r} - \Delta_y t/\hbar - \theta_y)$, where $\delta\mathbf{p} = \mathbf{p}_1 - \mathbf{p}_2 = p_x\hat{\mathbf{x}} + p_y\hat{\mathbf{y}}$, $\delta\mathbf{q} = \mathbf{q}_1 - \mathbf{q}_2 = q_x\hat{\mathbf{x}} + q_y\hat{\mathbf{y}}$ are relative wave vectors and θ_x, θ_y are relative phases between the two beams in each pair. In Wannier-Stark basis in the tight binding limit ($J \ll \Delta_x, \Delta_y$), this dipole potential has the following relevant components:

$$
\begin{aligned}
&\frac{\Omega_x}{2}\langle nm|e^{i(\delta\mathbf{p}\cdot\mathbf{r}-\Delta_x t/\hbar-\theta_x)}|nm\rangle = \frac{\Omega_x}{2}e^{i\theta_p(n,m)}e^{-i(\Delta_x t/\hbar+\theta_x)} + O\left(\frac{\Omega J^2}{\Delta^2}\right) \equiv A^{(x)}_{nm}(t),\\
&\frac{\Omega_y}{2}\langle nm|e^{i(\delta\mathbf{q}\cdot\mathbf{r}-\Delta_y t/\hbar-\theta_y)}|nm\rangle = \frac{\Omega_y}{2}e^{i\theta_q(n,m)}e^{-i(\Delta_y t/\hbar+\theta_y)} + O\left(\frac{\Omega J^2}{\Delta^2}\right) \equiv A^{(y)}_{nm}(t),\\
&\frac{\Omega_x}{2}\langle (n+1)m|e^{\pm i(\delta\mathbf{p}\cdot\mathbf{r}-\Delta_x t/\hbar-\theta_x)}|nm\rangle\\
&\quad = \frac{\Omega_x J}{2\Delta_x}e^{\pm i\theta_p(n,m)}e^{\mp i(\Delta_x t/\hbar+\theta_x)}\left(1 - e^{\pm ip_x a_x}\right) + O\left(\frac{\Omega J^2}{\Delta^2}\right),\\
&\frac{\Omega_y}{2}\langle (n+1)m|e^{\pm i(\delta\mathbf{q}\cdot\mathbf{r}-\Delta_y t/\hbar-\theta_y)}|nm\rangle\\
&\quad = \frac{\Omega_y J}{2\Delta_x}e^{\pm i\theta_q(n,m)}e^{\mp i(\Delta_y t/\hbar+\theta_y)}\left(1 - e^{\pm iq_x a_x}\right) + O\left(\frac{\Omega J^2}{\Delta^2}\right),\\
&\frac{\Omega_x}{2}\langle n(m+1)|e^{\pm i(\delta\mathbf{p}\cdot\mathbf{r}-\Delta_x t/\hbar-\theta_x)}|nm\rangle\\
&\quad = \frac{\Omega_x J}{2\Delta_y}e^{\pm i\theta_p(n,m)}e^{\mp i(\Delta_x t/\hbar+\theta_x)}\left(1 - e^{\pm ip_y a_y}\right) + O\left(\frac{\Omega J^2}{\Delta^2}\right),\\
&\frac{\Omega_y}{2}\langle n(m+1)|e^{\pm i(\delta\mathbf{q}\cdot\mathbf{r}-\Delta_y t/\hbar-\theta_y)}|nm\rangle\\
&\quad = \frac{\Omega_y J}{2\Delta_y}e^{\pm i\theta_q(n,m)}e^{\mp i(\Delta_y t/\hbar+\theta_y)}\left(1 - e^{\pm iq_y a_y}\right) + O\left(\frac{\Omega J^2}{\Delta^2}\right).
\end{aligned}
\tag{2.24}
$$

Here, $\theta_p(n,m) \equiv np_x a_x + mp_y a_y$, $\theta_q(n,m) \equiv nq_x a_x + mq_y a_y$. Now the overall

Hamiltonian is

$$
\begin{aligned}
&H(t) = H_0 + V_{\rm dip}(t) \\
&= \sum_{n,m} \Big\{ \Big(n\Delta_x + m\Delta_y + A^{(x)}_{nm}(t) + A^{(x)*}_{nm}(t) + A^{(y)}_{nm}(t) + A^{(y)*}_{nm}(t) \Big) |nm\rangle \langle nm| \\
&\quad + \frac{J}{\Delta_x} \Big(g(p_x a_x) A^{(x)}_{nm}(t) + g(q_x a_x) A^{(y)}_{nm}(t) + \text{c.c.} \Big) |(n+1)m\rangle \langle nm| + \text{ H.c.} \\
&\quad + \frac{J}{\Delta_y} \Big(g(p_y a_y) A^{(x)}_{nm}(t) + g(q_y a_y) A^{(y)}_{nm}(t) + \text{c.c.} \Big) |n(m+1)\rangle \langle nm| + \text{ H.c.} \Big\}, \\
&\text{where} \quad g(x) = 1 - e^{ix}.
\end{aligned} \tag{2.25}
$$

To get rid of differences in diagonal terms, we can use a transformation U to a rotating frame,

$$
\begin{aligned}
U &= \exp\left[i \sum_{n,m} \left\{ \frac{n\Delta_x + m\Delta_y}{\hbar} t - 2 \ \text{Im} \left(\frac{A^{(x)}_{nm}(t)}{\Delta_x} + \frac{A^{(y)}_{nm}(t)}{\Delta_y} \right) \right\} |nm\rangle \langle nm| \right] \\
&\equiv \sum_{n,m} e^{iB(n,m)} |nm\rangle \langle nm| .
\end{aligned} \tag{2.26}
$$

In this rotating frame, the effective Hamiltonian is given by

$$
\begin{aligned}
H_{\rm rot} &= UHU^\dagger + i\hbar \left(\partial_t U\right) U^\dagger \\
&\equiv \sum_{n_x,n_y} J^{(x)}_{nm}(t) |(n+1)m\rangle \langle nm| + J^{(y)}_{nm}(t) |n(m+1)\rangle \langle nm| + \text{ H.c.} \\
&= \sum_{n,m} \Big\{ \frac{J}{\Delta_x} e^{i(B(n+1,m) - B(n,m))} \Big(g(p_x a_x) A^{(x)}_{nm}(t) + g(q_x a_x) A^{(y)}_{nm}(t) + \text{c.c.} \Big) \\
&\qquad \times |(n+1)m\rangle \langle nm| + \text{ H.c.} \\
&\qquad + \frac{J}{\Delta_y} e^{i(B(n,m+1) - B(n,m))} \Big(g(p_y a_y) A^{(x)}_{nm}(t) + g(q_y a_y) A^{(y)}_{nm}(t) + \text{c.c.} \Big) \\
&\qquad \times |n(m+1)\rangle \langle nm| + \text{ H.c.} \Big\}.
\end{aligned} \tag{2.27}
$$

By using Jacobi-Anger identity $e^{iz\cos\theta} = \sum_{r\in\mathbb{Z}} i^r J_r(z) e^{ir\theta}$, we get

$$
\begin{aligned}
&e^{i(B(n+1,m)-B(n,m))} \\
&= e^{i\Delta_x t/\hbar} \exp\left\{-i\frac{2\Omega_x}{\Delta_x}\sin\frac{p_x a_x}{2}\cos(\theta_p(n,m)+p_x a_x/2-\Delta_x t/\hbar-\theta_x)\right\} \\
&\quad\times\exp\left\{-i\frac{2\Omega_y}{\Delta_y}\sin\frac{q_x a_x}{2}\cos(\theta_q(n,m)+q_x a_x/2-\Delta_y t/\hbar-\theta_y)\right\} \\
&= e^{i\Delta_x t/\hbar}\sum_r J_r\left(-\frac{2\Omega_x}{\Delta_x}\sin\left(\frac{p_x a_x}{2}\right)\right) i^r e^{ir(\theta_p(n,m)+p_x a_x/2-\Delta_x t/\hbar-\theta_x)} \\
&\quad\times\sum_s J_s\left(-\frac{2\Omega_y}{\Delta_y}\sin\left(\frac{q_x a_x}{2}\right)\right) i^s e^{is(\theta_q(n,m)+q_x a_x/2-\Delta_y t/\hbar-\theta_y)}, \\
&e^{i(B(n,m+1)-B(n,m))} \\
&= e^{i\Delta_y t/\hbar} \exp\left\{-i\frac{2\Omega_x}{\Delta_x}\sin\frac{p_y a_y}{2}\cos(\theta_p(n,m)+p_y a_y/2-\Delta_x t/\hbar-\theta_x)\right\} \\
&\quad\times\exp\left\{-i\frac{2\Omega_y}{\Delta_y}\sin\frac{q_y a_y}{2}\cos(\theta_q(n,m)+q_y a_y/2-\Delta_y t/\hbar-\theta_y)\right\} \\
&= e^{i\Delta_y t/\hbar}\sum_r J_r\left(-\frac{2\Omega_x}{\Delta_x}\sin\left(\frac{p_y a_y}{2}\right)\right) i^r e^{ir(\theta_p(n,m)+p_y a_y/2-\Delta_x t/\hbar-\theta_x)} \\
&\quad\times\sum_s J_s\left(-\frac{2\Omega_y}{\Delta_y}\sin\left(\frac{q_y a_y}{2}\right)\right) i^s e^{is(\theta_q(n,m)+q_y a_y/2-\Delta_y t/\hbar-\theta_y)}.
\end{aligned}
\tag{2.28}
$$

For brevity, we define

$$
\begin{aligned}
C_{p,x(y)} &\equiv (2\Omega_{x(y)}/\Delta_{x(y)})\sin(p_{x(y)}a_{x(y)}/2), \\
C_{q,x(y)} &\equiv (2\Omega_{x(y)}/\Delta_{x(y)})\sin(q_{x(y)}a_{x(y)}/2).
\end{aligned}
\tag{2.29}
$$

By time averaging Eq. (2.27) over the time scale $\sim \hbar/\Delta$, we obtain following effective

tunneling amplitudes:

$$
\begin{aligned}
J^{(x)}_{nm,\text{eff}} &= \frac{J\Omega_x}{2\Delta_x}\Big\{e^{i(\theta_p(n,m)-\theta_x)}(1-e^{ip_xa_x})J_0\left(C_{p,x}\right) \\
&\qquad -e^{-i(\theta_p(n,m)-\theta_x)}(1-e^{-ip_xa_x})J_2\left(C_{p,x}\right)e^{i2(\theta_p(n,m)+p_xa_x/2-\theta_x)}\Big\}J_0\left(C_{q,x}\right) \\
&= \frac{J\Omega_x}{2\Delta_x}e^{i(\theta_p(n,m)-\theta_x)}(1-e^{ip_xa_x})\left\{J_0\left(C_{p,x}\right)+J_2\left(C_{p,x}\right)\right\}J_0\left(C_{q,x}\right) \\
&= JJ_1\left(C_{p,x}\right)J_0\left(C_{q,x}\right)\exp\{i(\theta_p(n,m)-\theta_x+(p_xa_x-\pi)/2)\}, \\
J^{(y)}_{nm,\text{eff}} &= \frac{J\Omega_y}{2\Delta_y}\Big\{e^{i(\theta_q(n,m)-\theta_y)}(1-e^{iq_ya_y})J_0\left(C_{q,y}\right) \\
&\qquad -e^{-i(\theta_q(n,m)-\theta_y)}(1-e^{-iq_ya_y})J_2\left(C_{q,y}\right)e^{i2(\theta_q(n,m)+p_ya_y/2-\theta_y)}\Big\}J_0\left(C_{p,y}\right) \\
&= \frac{J\Omega_y}{2\Delta_y}e^{i(\theta_q(n,m)-\theta_y)}(1-e^{iq_ya_y})\left\{J_0\left(C_{q,y}\right)+J_2\left(C_{q,y}\right)\right\}J_0\left(C_{p,y}\right) \\
&= JJ_1\left(C_{q,y}\right)J_0\left(C_{p,y}\right)\exp\{i(\theta_q(n,m)-\theta_y+(q_ya_y-\pi)/2)\}. \qquad (2.30)
\end{aligned}
$$

Since θ_p and θ_q are linear in n and m, the resulting effective Hamiltonian describes the charged particle under the presence of a uniform magnetic field [132]. These expressions can be further simplified in perturbative regime, $\Omega_x, \Omega_y \ll \Delta_x, \Delta_y$. In such case, $C_{p,x(y)}, C_{q,x(y)} \ll 1$, so $J_0(C) = 1 + O(C^2)$ and $J_1(C) = C/2 + O(C^2)$. Then by setting $\theta_x = (p_xa_x + \pi)/2$ and $\theta_y = (q_ya_y + \pi)/2$, we get

$$
\begin{aligned}
J^{(x)}_{nm,\text{eff}} &= -\frac{J\Omega_x}{\Delta_x}\sin\left(\frac{p_xa_x}{2}\right)\exp\{i(np_xa_x+mp_ya_y)\}, \\
J^{(y)}_{nm,\text{eff}} &= -\frac{J\Omega_y}{\Delta_y}\sin\left(\frac{q_ya_y}{2}\right)\exp\{i(nq_xa_x+mq_ya_y)\}. \qquad (2.31)
\end{aligned}
$$

2.10 Beam Configuration for Quantum Hall Hamiltonian on Torus

For the simplicity of construction, we assume our lattice spans from $(n, m) = (1, 1)$ to $(n, m) = (L, L) = (p+2q+1, p+2q+1)$. Here, p is the width of the square puncture in the middle while q is the width of the square annulus, in the unit of lattice spacing. To obtain the tunneling phases shown in Eq. (2.7), we need our Raman beams to satisfy following conditions:

$$(\mathbf{k}_{i+})_z = -(\mathbf{k}_{i-})_z = (\pi/4)z_0^{-1}, \quad i = 1 \text{ to } 4. \tag{2.32}$$

$$\begin{aligned} |\mathbf{k}_1| - |\mathbf{k}_{1\pm}| = |\mathbf{k}_{3\pm}| - |\mathbf{k}_3| = (\omega_1 - \omega_{1\pm})/c = (\omega_{3\pm} - \omega_3)/c = \Delta_x/\hbar c, \\ |\mathbf{k}_2| - |\mathbf{k}_{2\pm}| = |\mathbf{k}_{4\pm}| - |\mathbf{k}_4| = (\omega_2 - \omega_{2\pm})/c = (\omega_{4\pm} - \omega_4)/c = \Delta_y/\hbar c. \end{aligned} \tag{2.33}$$

$$\begin{aligned} (\mathbf{k}_1 - \mathbf{k}_{1\pm})_x = (\mathbf{k}_2 - \mathbf{k}_{2\pm})_x = (\mathbf{k}_{3\pm} - \mathbf{k}_3)_x = (\mathbf{k}_4 - \mathbf{k}_{4\pm})_x = \phi/2a_x, \\ (\mathbf{k}_{1\pm} - \mathbf{k}_1)_y = (\mathbf{k}_{2\pm} - \mathbf{k}_2)_y = (\mathbf{k}_{3\pm} - \mathbf{k}_3)_y = (\mathbf{k}_4 - \mathbf{k}_{4\pm})_y = \phi/2a_y. \end{aligned} \tag{2.34}$$

$$(p+q)\phi \bmod 2\pi = (q+2)\phi \bmod 2\pi = 0. \tag{2.35}$$

Here, the relative phase between beams $\mathbf{k}_{i+}$ and $\mathbf{k}_{i-}$ are adjusted in a way that the vertical standing wave between them have a node at $z = -z_0$ $(i = 1, 2)$ or $z = z_0$ $(i = 3, 4)$. That is, the beam triplets $T_\mathbf{1}$ and $T_\mathbf{2}$ target the upper layer while the beam

triplets $T_{\mathbf{3}}$ and $T_{\mathbf{4}}$ target the lower layer. Eq. (2.32) is required to guarantee that beams labeled with $+$ and beams labeled with $-$ to show constructive interference at targeted layer while they destructively interfere at the non-targeted layer. Eq. (2.33) implies that $T_{\mathbf{1}}$ and $T_{\mathbf{3}}$ give laser-assisted tunneling in the x direction while $T_{\mathbf{2}}$ and $T_{\mathbf{4}}$ give laser-assisted tunneling in the y direction. Eq. (2.34) ensures that synthetic magnetic flux threading each plaquette in the outward direction to be ϕ, with a choice of symmetric gauge. Expressions for laser-assisted tunneling terms are identified in Eq. (2.30) and Eq. (2.31). With given conditions, phases of the tunneling terms in Eq. (2.31) are given by

$$\begin{aligned}
\mathrm{Arg}\left(-J^{(x)}_{nm,\mathrm{eff}}\right) &= \begin{cases} (\mathbf{k_1}-\mathbf{k}_{\mathbf{1},\pm})\cdot\mathbf{r}_{nm} = (n-m)\phi/2 & \text{upper layer} \\ (\mathbf{k}_{\mathbf{3},\pm}-\mathbf{k_3})\cdot\mathbf{r}_{nm} = (n+m)\phi/2 & \text{lower layer} \end{cases}, \\
\mathrm{Arg}\left(-J^{(y)}_{nm,\mathrm{eff}}\right) &= \begin{cases} (\mathbf{k_2}-\mathbf{k}_{\mathbf{2},\pm})\cdot\mathbf{r}_{nm} = (n-m)\phi/2 & \text{upper layer} \\ (\mathbf{k}_{\mathbf{4},\pm}-\mathbf{k_4})\cdot\mathbf{r}_{nm} = -(n+m)\phi/2 & \text{lower layer} \end{cases}, \\
&\text{where} \quad \mathbf{r}_{nm} = na_x\hat{\mathbf{x}} + ma_y\hat{\mathbf{y}}.
\end{aligned} \tag{2.36}$$

To have the uniform synthetic magnetic field all over the torus surface, we need to make every plaquette in the side areas to have flux ϕ in the outward direction. Keeping the inter-layer tunneling real, the outward flux from each plaquette in side areas are shown in Fig. 2.8(a). While the outward fluxes from different sides are not identical in general, we may set all of them to be identical up to modulo of 2π.

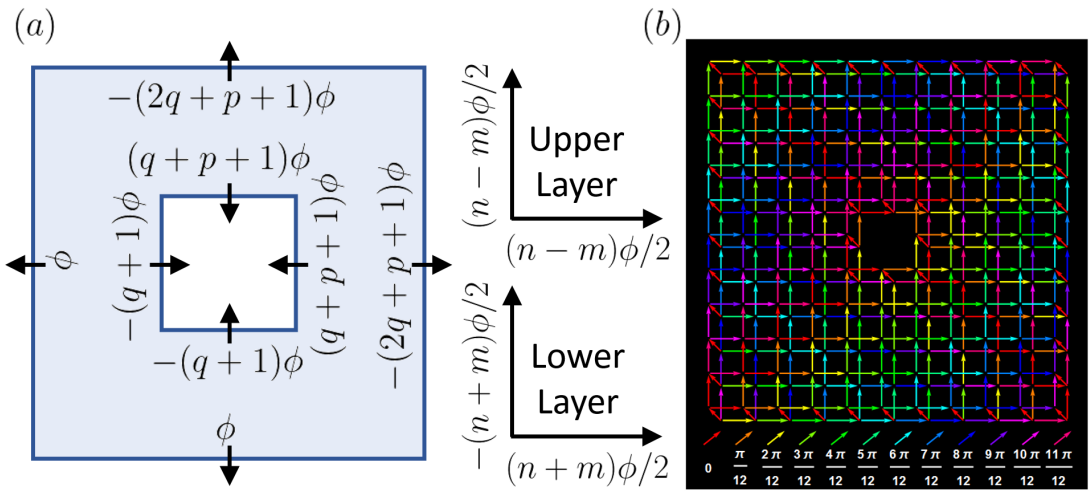

Figure 2.8: (a) Flux per plaquette toward the outside of torus along the side areas. p is the width of the square puncture in the middle, and q is the width of the square annulus. Size of the square lattice is then $L \times L$, $L = 2q + p + 1$. (b) tunneling phases of sample lattice with $p = 2, q = 4, \phi = \pi/3$.

That is,

$$-(q+1)\phi \bmod 2\pi = (p+q+1)\phi \bmod 2\pi = -(2q+p+1)\phi \bmod 2\pi = \phi, \quad (2.37)$$

which is equivalent to the condition Eq. (2.35). To illustrate how this scheme works altogether, tunneling phases in a lattice with $p = 2, q = 4, \phi = \pi/3$ is shown in Fig. 2.8(b). From this figure, one can check that outward flux from every single plaquette is the same as ϕ.

2.11 Measurement of Topological Degeneracy

In Fig. 2.4(g), the spectral flow and the flow of the y-coordinates in the changing twist angle show very similar graphs to each other. To briefly understand the physics behind this resemblance, we can consider the thin torus limit [133]. For

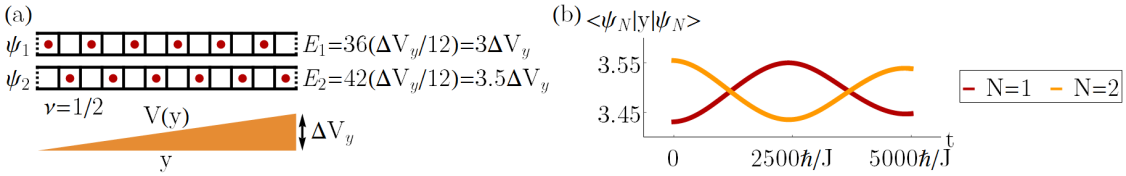

Figure 2.9: (a) The relation between the energy splitting and difference in y-coordinates becomes clear in the thin torus limit. Case of $N_p = 6, \nu = 1/2$ is shown for an example. (b) Average y-coordinates during the adiabatic flux insertion, in the presence of potential $V(y) = (0.01J/L_y)y$. Flux corresponds to $\alpha_x = 4\pi$ is inserted over the time interval of $5000\hbar/J$.

a short interaction length, the two-fold degenerate ground states for $\nu = 1/2$ are given as $|010101\cdots\rangle$ and $|101010\cdots\rangle$ where each 0 and 1 indicates the occupation at each orbital. While there is some freedom to choose these orbitals, we select the orbitals localized in the y direction on the torus $(x, y) \in [0, L_x) \times [0, L_y)$. If a perturbative potential $V(y) = (\Delta V_y/L_y)y$ is applied, the energy shift in each ground state is proportional to the y-coordinate expectation values of each state, as shown in Fig. 2.9(a). Since this energy splitting is a finite-size effect which should vanish in the thermodynamic limit, the proportionality constant presented in this thin torus limit is not precise. Yet, in a finite-size system, this effect can be experimentally detected.

With a proper cooling scheme, we can prepare atoms to be in a particular ground state due to the energy splitting. Yet, to observe the 4π-periodicity in spectral flow of each state, the flux should to be inserted adiabatically. To see if such an adibatic evolution is possible, we simulate the procedure of flux insertion on the system in Fig. 2.4(g) [Fig. 2.9(b)]. As shown in the figure, change in y-coordinates can be detected in a proper adiabatic time evolution. By measuring the atomic densities for the varying twist angle, one can detect the anticipated

periodicity and therefore measure the topological degeneracy.

2.12 Outlook

Aforementioned generalization of the scheme to a genus-g surface leads to a topologically protected m^g-fold degenerate ground-state subspace for abelian and non-abelian FQH states. In that context, one can implement modular transformations to probe topological orders, measure fractional statistics, and realize fault-tolerant logical gates for topological quantum computations [134, 135].

Chapter 3: Twist Defects in Optical Lattice

3.1 Introduction

Ultra-cold atoms in optical lattices have been broadly used to study a variety of coherent and many-body physics for the high tunability of the optical lattices [92, 93, 136, 137]. Among many attempts to create various lattice structure in different dimensions using this tunability of optical lattices [107, 109, 111, 138–143], the creation of topologically non-trivial surfaces have drawn huge attentions for its possibility to host the topologically ordered phases of matter such as fractional quantum Hall (FQH) states [72, 112] or spin liquids [113–115]. Such phases of matter is interesting not only for their rich many-body physics but also for the possible applications in the topological quantum computation [113]. While several schemes have been proposed to create topologically non-trivial closed surfaces for the ultra-cold atoms [118, 144], the experimental realization of such schemes still remains as a challenging problem.

One common challenge in the schemes suggested so far is the necessity of creating a closed surface. To create a closed surface, one needs to connect all the boundaries to each other and such task is often experimentally demanding. However, one can still create topologically non-trivial surfaces by introducing twist defects in

a bilayer system [145–149]. Here, twist defects are the point defects created at the end of line defects that sew each layer of a bilayer system with the other layer, as shown in Fig. 3.1(a). As long as the line defects are located far enough from the boundary of the system, one can map the entire bilayer system with $g + 1$ pairs of twist defects to a g-genus surface up to two punctures that does not harm the topological nature of the system.

In this paper, we propose a scheme to construct a bilayer optical lattice with multiple pairs of twist defects. Specifically, we use spin-dependent optical lattice [150–154] in checker board shape where each spin of the atomic ground state to represent each of layer in the bilayer system. To create pairs of twist defects, we use Raman process to generate inter-layer tunneling across the line defects which are set by site-resolving laser fields, where such spatially shaped beams can be achieved with recent advancements in high-resolution imaging techniques [24, 94, 98–100, 119, 155–157]. To exhibit the role of topology in the dynamics of atoms on the creates surface, we first study the hydrodynamcis of bosonic superfluid stirred around the twist defects. Specifically, we introduce sequences of local optical manipulation that can generate quantized supercurrents and verify its feasibility with numerical simulations. Moreover, to study the topologically ordered phases in strongly correlated regime, we discuss a FQH model realizable on our lattice construction. We also illustrate how the topologically ordered phases can be measured through randomized local unitary operations even in the presence of open boundaries. Finally, we discuss how the braiding of twist defects guided by the modulation of the laser field can be used for the operation among the topologically

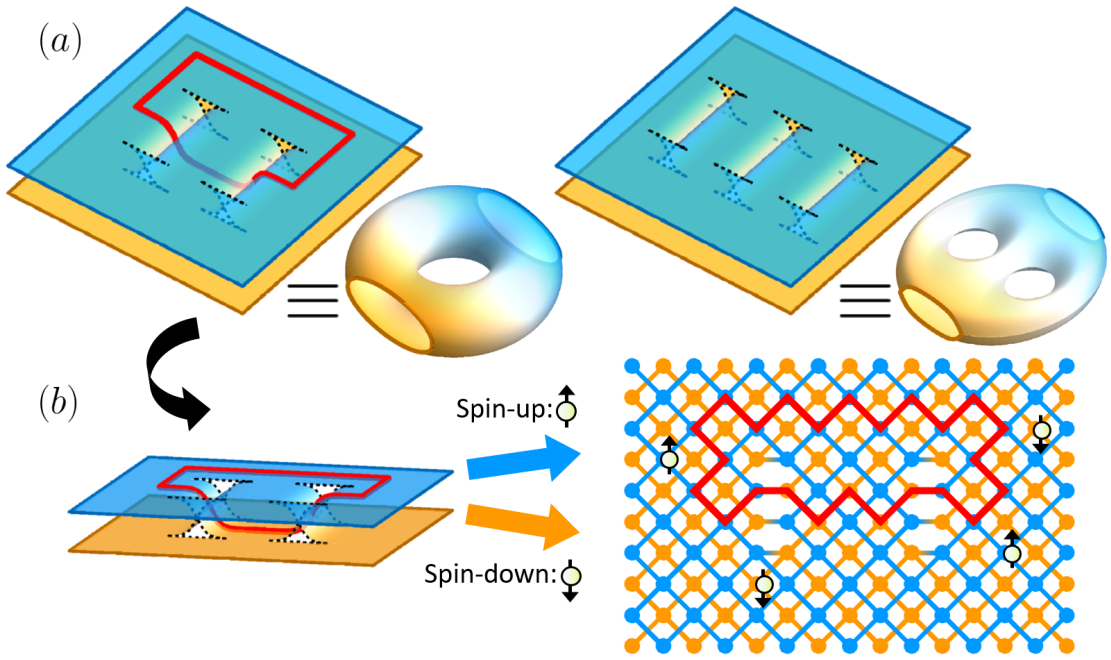

Figure 3.1: (a) Bilayer surface with twist defects. A surface with $g+1$ pairs of twist defects is topologically equivalent to a g-genus surface up to two punctures. (b) The upper (lower) layer is consisted of atoms in the spin-up (spin-down) state. Atoms with different spin states are put in alternating order in a checkerboard lattice. For the demonstration purpose, a sample non-contractible loop is drawn in red.

degenerated states.

3.2 Bilayer Lattice with Twist Defects

To construct a bilayer lattice, we consider spin-up (spin-down) state of an alkali atomic ground state, $|\uparrow\rangle$ ($|\downarrow\rangle$), represents the upper (lower) layer of the bilayer system (Fig. 3.1). With Zeeman energy splitting $\epsilon > 0$, these two layers are energetically separated. To avoid the undesired interaction between different layers, we let different spin states stay on alternating sites in a checkerboard lattice. For this, we create a spin-dependent dipole potential $V_{lat}(\mathbf{r})$ generated by following plane wave

laser beams with different polarizations [Fig. 3.2(a)]:

$$\begin{aligned}
\mathbf{E}(\mathbf{r},t) &= \mathcal{E}\sum_{s=\pm1}\left(e^{isky}\hat{\mathbf{x}}+ie^{iskx}\hat{\mathbf{y}}\right)e^{-i\omega t}+\text{c.c.} \\
&\equiv \left[\mathcal{E}_1(x,y)\hat{\mathbf{e}}_1+\mathcal{E}_{-1}(x,y)\hat{\mathbf{e}}_{-1}\right]e^{-i\omega t}+\text{c.c.}\ , \\
V_{lat}(\mathbf{r}) &= f_0\sum_{s=\pm1}\left[\left(\frac{2}{\Delta_{3/2}}+\frac{1}{\Delta_{1/2}}\right)\mathcal{E}_s^2(x,y)\otimes I\right. \\
&\qquad \left.+\left(\frac{1}{\Delta_{3/2}}-\frac{1}{\Delta_{1/2}}\right)s\mathcal{E}_s^2(x,y)\otimes\sigma_z\right]. \qquad (3.1)
\end{aligned}$$

where $\hat{\mathbf{e}}_{\pm1}=(\hat{\mathbf{x}}\pm i\hat{\mathbf{y}})/\sqrt{2}, \hat{\mathbf{e}}_0=\hat{\mathbf{z}}$ are circular polarizations and $I=|\uparrow\rangle\langle\uparrow|+|\downarrow\rangle\langle\downarrow|$, $\sigma_z=|\uparrow\rangle\langle\uparrow|-|\downarrow\rangle\langle\downarrow|$. $\omega=ck$ is the beam frequency, where we set $\hbar=1$ from now on. f_0 is the proportionality constant, and $\Delta_{1/2}$ ($\Delta_{3/2}$) is the detuning from atomic transition $S_{1/2}\rightarrow P_{1/2}$ ($S_{1/2}\rightarrow P_{3/2}$). By setting the beam frequency to satisfy $\Delta_{3/2}=-2\Delta_{1/2}$, the dipole potential becomes $V_{lat}(\mathbf{r})=-V_0\cos kx\cos ky\otimes\sigma_z$ where $V_0=12f_0\mathcal{E}^2/\Delta_{1/2}$. This potential confines atoms with different spin states in alternating sites of a checkerboard lattice with lattice spacing $a=\pi/k$. Note that extra pair of laser beams is required to confine the atoms in the z direction.

We need a few more laser beams to to create a line defect sewing different layers. First, we need Raman beams to restore the inter-layer tunnelings across the designated line. For this, we shine a pair of red-detuned beams whose frequency difference matches with the Zeeman energy splting ϵ [Fig. 3.2(b)]. We set the polarization of one of these beams to be $\hat{\mathbf{x}}=(\hat{\mathbf{e}}_1+\hat{\mathbf{e}}_{-1})/\sqrt{2}$ and the other beam to be $\hat{\mathbf{z}}=\hat{\mathbf{e}}_0$ so that spin state can flip through the resonant Raman process between these beams. By shaping the beam with polarization $\hat{\mathbf{x}}$ to target only the sites around the

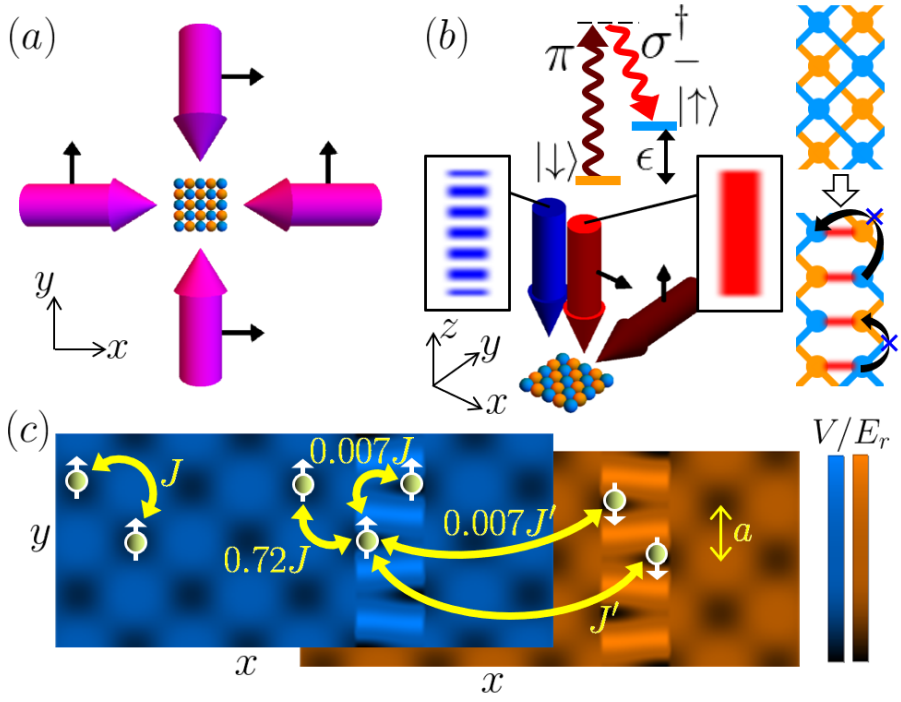

Figure 3.2: (a) The spin-dependent checker board lattice is generated by pairs of counter-propagating laser beams in the x and y direction. These beams have in-plane polarizations, which are represented as small black arrows. (b) Different layers are connected through the Raman beam pair with detuning equal to Zeeman energy ϵ. The intensity pattern of one of these beams define the location of line defects. Additional beam with a stripe intensity pattern generates potential barriers to block undesired tunnelings. (c) Numerically calculated tunneling strengths for different pairs of neighboring sites. Here, the dipole potential is evaluated with $V_0 = 5E_r$, $V_b = 25E_r$ where $E_r = k^2/2M$ is the recoil energy. V_r is set to satisfy Eq. (3.3) with these parameters.

designated line defect, we can control the area affected by this Raman process. Next, we need another beam that creates potential barriers to block undesired tunnelings. In particular, we shine a blue-detuned beam targeting the area around the line defect, with an intensity pattern of stripe ridges with period a [Fig. 3.2(b)]. Along with the previous Raman beam targeting the same area, the overall dipole potential

becomes

$$V(\mathbf{r}) \quad = \quad V_{lat}(\mathbf{r}) + A(\mathbf{r}) \left[V_b \sin^2 \left(\frac{\pi y}{a} \right) - V_r \right], \tag{3.2}$$

where the regional function $A(\mathbf{r})$ is 1 if $\mathbf{r}$ is within the distance of $a/2$ from the line defect and is 0 otherwise. $V_b(V_r)$ is the potential amplitude created from the blue-detuned (red-detuned) beam. Then, this potential creates barriers along the direction of line defect which prevent atoms around the line defect to tunnel into the other lattice sites than the nearest ones across the line defect.

To make the surface around the line defects smooth, we need to calibrate the on-site energy of every site equal. Here, on-site energy of a lattice site is the sum of dipole potential and the zero point energy of the harmonic confinement at that site. Then the calibration condition is

$$E_{\mathbf{R}_\mathrm{I}} = E_{\mathbf{R}_\mathrm{O}}, \;\; E_{\mathbf{R}} = V(\mathbf{R}) + \sum_{s=x,y} \sqrt{\frac{\partial_s^2 V(\mathbf{r})|_{\mathbf{r}=\mathbf{R}}}{4M}}, \tag{3.3}$$

where $\mathbf{R}_\mathrm{I}$ ($\mathbf{R}_\mathrm{O}$) is the position of a lattice site that is (is not) adjacent to the line defects. M here is the atomic mass. This condition can be satisfied by tuning V_0, V_b and V_r in Eq. (3.2) appropriately.

In order to check if our dipole potential can generate the desired lattice model, we numerically evaluate the different tunneling strengths based on the potential in Eq. (3.2). For this, we calculate pseudo Wannier functions for different lattice sites and evaluate overlaps between them to obtain different tunneling strengths. To make

the beam design more experimentally accessible, We modify the regional function in Eq. (3.2) so that it has smooth boundary. Calculated tunneling strengths with a sample set of parameters satisfying Eq. (3.3) are shown in Fig. 3.2(c). As shown in the figure, it is possible to keep the undesired tunneling strengths far weaker than the desired tunneling strengths. Note that our optical lattice design heavily relies on capabilities of generating arbitrary beam intensity patterns with a high precision, while the recent progress in beam-shaping technologies enable us to engineer such laser beams.

3.3 Quantized Supercurrents along Different Non-contractible Loops

To illustrate how topology affects the dynamics of ultracold atoms on the surface with twist defects, we numerically study the hydrodynamics of weakly interacting bosonic superfluid on such surface. A distinct phenomenon we can expect is the supercurrent flowing along each non-contractible loop. While there are several ways to create supercurrent flows in a bosonic condensate, one can stir the condensate with extra spin-dependent potential along some of the non-contractible loops. This requires blue-detuned dipole potentials addressing on different layers selectively, and it can be achieved by tuning the frequency of extra beam relatively closer to one spin-flip transition than the other transitions, remaining in the far-detuned limit compared to the tunneling strengths [Fig. 3.3(a)]. With careful arrangement of stirring paths, supercurrent flows along different non-contractible loops can be generated, and that dynamics can be captured through following mean-field description

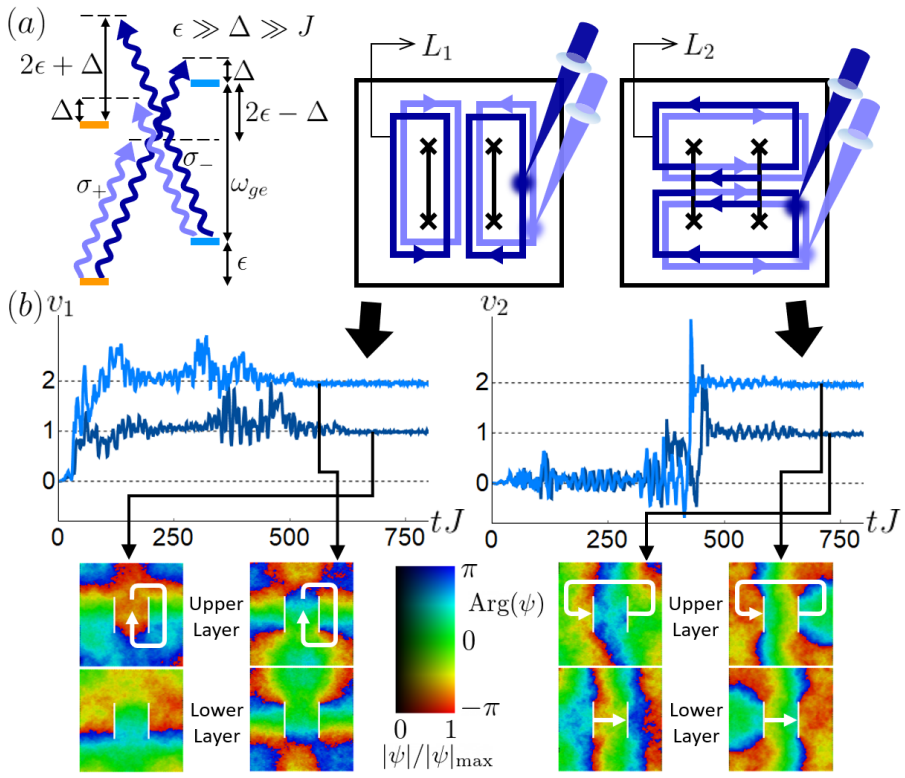

Figure 3.3: (a) The frequency of a laser beam is set close to the excitation from the spin-up (spin-down) state to the excited spin-down (spin-up) state. By controlling the detuning much smaller than the Zeeman energy ϵ and much larger than the typical tunneling strength J, this beam can effectively generate the dipole potential only on the upper (lower) layer. By using these layer-targeting beams as stirrers for different non-contractible loops, one can generate supercurrent flows along those loops. (b) Simulation of stirring procedures for different stirring loops. Generated supercurrent flows show the quantized vorticities along the stirred non-contractible loops. For the clarity of vorticity counting, guide lines (white) for non-contractible loops are drawn.

of the bosonic condensate:

$$i\hbar\partial_t\psi_{\mathbf{i}\rho} = -J\sum_{\langle\mathbf{j},\mathbf{k}\rangle}\psi_{\mathbf{j}\bar{\rho}}\delta_{\mathbf{ik}} - J\sum_{[\mathbf{j},\mathbf{k}]}\psi_{\mathbf{j}\rho}\delta_{\mathbf{ik}} + \left\{V_\rho(i_x,i_y,t) - \mu + U\left|\psi_{\mathbf{i}\rho}\right|^2\right\}\psi_{\mathbf{i}\rho}. \quad (3.4)$$

Here, $\psi_{\mathbf{i}\rho}$ is the condensate wave function at site $\mathbf{i} = (i_x, i_y)$ on layer ρ, where $i_x + i_y$ must be even (odd) for $\rho =\uparrow (\downarrow)$. $\bar{\rho} =\downarrow (\uparrow)$ for $\rho =\uparrow (\downarrow)$. $\langle\mathbf{j},\mathbf{k}\rangle$ indicate the nearest neighboring pairs of sites $\mathbf{j},\mathbf{k}$ that intersect with the line defects. $[\mathbf{j},\mathbf{k}]$ indicate

pairs of sites $\mathbf{j}, \mathbf{k}$ such that $|\mathbf{j} - \mathbf{k}|^2 = 2$ where the pairs do not intersect with the line defects. J is the tunneling strength, U is the on-site interaction energy, V_ρ is the stirring potential on layer ρ, and μ is the chemical potential. With this mean-field description, we simulated the supercurrent generation procedures as shown in Fig. 3.3(b).

Since the condensate wave function is single-valued, supercurrent flows generated along each non-contractible loop is quantized in a certain way. In particular, up to some finite-size fluctuation, the vorticity defined as following is quantized to an integer:

$$v_n = \frac{1}{2\pi\rho_{\text{avg}}} \sum_{s=0}^{N-1} \text{Im}\left(\psi^*_{\mathbf{i}_s\sigma_s}\psi_{\mathbf{i}_{s+1}\sigma_{s+1}}\right) \tag{3.5}$$

where $\mathbf{i}_1\sigma_1, \cdots, \mathbf{i}_N\sigma_N = \mathbf{i}_0\sigma_0$ are lattice points along the non-contractible loop L_n. ρ_{avg} is the average condensate occupation per site. Dyanmics of these vorticities during the stirring procedures are presented in Fig. 3.3(b). As shown in the figure, these vorticities converge into different integers after strring, depending on the strength and speed of stirrer.

3.4 FQH States with Twist Defects

More interestingly, strongly interacting ultracold atoms on the surface with twist defects can exhibit exotic topological physics. A good example to study is FQH system on such surface, and one of the simplest bosonic lattice model for such

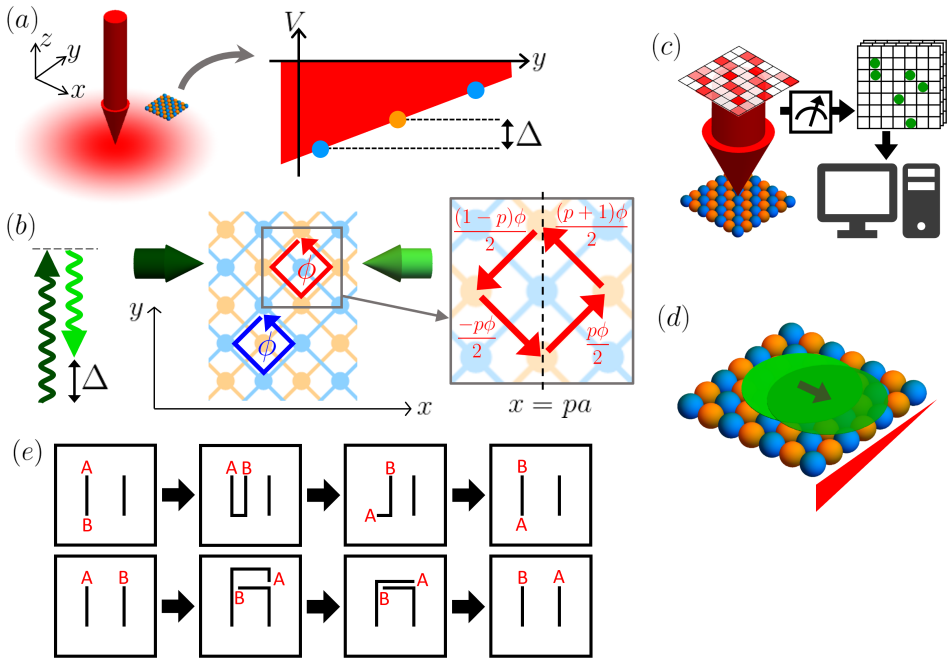

Figure 3.4: (a) A uniform dipole potential gradient can be created by an out-of-focus Gaussian beam. (b) To create uniform synthetic magnetic field, we apply a Raman beam pair with the momentum kick perpendicular to the linear potential gradient. This makes an atom to accumulate a total phase of ϕ when circulating each plaquette on each layer. (c) By applying randomized on-site potential through site-resolving tailored laser light, one can perform random unitary operations. By processing the particle occupation measurements followed by the random unitary operations, one can obtain the fractional Chern number. (d) The Hall conductivity can be determined by measuring the Hall drift of the center of mass in response of a extra linear dipole potential gradient. (e) By slowly altering the targeting region of the focused beams configuring the line defects, one can deform the line defects as desired. Through some sequences of such deformation, one can braid arbitrary two twist defects.

system is Harper-Hofstadter-Hubbard (HHH) Hamiltonian [132, 158]:

$$H = \sum_{\rho=\uparrow,\downarrow} \left\{ \sum_{\mathbf{i}} \frac{U}{2} a^{\dagger 2}_{\mathbf{i}\rho} a^{2}_{\mathbf{i}\rho} - J' \sum_{\langle \mathbf{i},\mathbf{j} \rangle} a^{\dagger}_{\mathbf{i}\rho} a_{\mathbf{j}\bar{\rho}} - J \sum_{[\mathbf{i},\mathbf{j}]} \left(e^{ij_x\phi/2} a^{\dagger}_{\mathbf{i}\rho} a_{\mathbf{j}\rho} + \text{H.c.} \right) \right\}. \tag{3.6}$$

Here, $a^{\dagger}_{\mathbf{i}\rho}$ creates an atom at site $\mathbf{i} = (i_x, i_y)$ on layer ρ, where $i_x + i_y$ must be even (odd) for $\rho = \uparrow$ ($\downarrow$). Conventions for $\bar{\rho}$, $\langle \mathbf{i},\mathbf{j} \rangle$, and $[\mathbf{i},\mathbf{j}]$ are the same as in Eq. (3.4). J and J' are the effective intra- and interlayer tunneling strengths,

U is the on-site interaction energy. ϕ represents the threaded flux per each square plaquette on each layer. This HHH Hamiltonian is known to host the bosonic lattice version of Laughlin states [158]. In the presence of $g+1$ pairs of twist defects, the Laughlin states with filling fraction $1/m$ (m even) have m^g-fold topologically protected degeneracy, just as in the g-genus surface [147].

The HHH Hamiltonian can be realized within our setup by using the laser-assisted tunnelings [7, 8]. For this, we require a uniform dipole potential gradient which can be created by an out-of-focus Gaussian beam. This potential gradient introduces a uniform on-site energy difference between nearby lattice sites in its direction, and a pair of Raman beams is applied in a way that their detuning matches to this on-site energy difference. By adjusting the direction of momentum kick from the Raman beam pair to be perpendicular to the dipole potential gradient, one can create synthetic flux ϕ per each square plaquette on each layer. Along with the on-site interaction between atoms, this scheme complete the HHH Hamiltonian in Eq. (3.6).

Furthermore, pairs of twist defects not only provide a topologically non-trivial surface, but also can be used for non-trivial quantum operations on the topological states hosted on this surface. For instance, the braiding of twist defects follow a non-Abelian statistics despite the fact that underlying Laughlin states only have Abelian quasiparticles [145, 147, 148]. That is, by braiding different twist defects, one transforms the topological quantum state to a different state rather than mere acquisition of a phase factor. Such braiding operation can be naturally performed in our setup, since the location of line defects are solely defined by the target area of

focused laser beams. By slowly adjusting the targeting area of these beams, one can deform the line defects as desired. By undergoing a sequence of such deformations, one can do arbitrary braiding of twist defects as presented in Fig. 3.4(e). If the deformation of line defects is inconvenient, there is also another way to realize the braiding operations by performing a sequence of projective measurements [134].

While our scheme prepares the FQH states in the presence of open boundaries, there are still several ways to measure the topological properties of these states. In a recently developed scheme using randomized measurement [159, 160], the atom population over the lattice is measured repeatedly given the application of randomized unitary operation, and one can calculate the many-body Chern number out of these population measurement results. The randomized unitary operation in this process can be realized in our setup by applying randomized disorder dipole potential through a site-resolving, arbitrarily shapable laser beam [Fig. 3.4(c)]. Also, one can determine the Hall conductivity by measuring the Hall drift speed of the atomic center of mass as a linear response to a extra uniform dipole potential gradient [9, 161]. It is also possible to do projective measurement of the many-body states by using an interferometry using an auxiliary qubit [135, 162].

3.5 Evaluation of Tunneling Strength

To evaluate tunneling strength between neighboring sites, we numerically calculate a pseudo-Wannier function for each lattice site based on the lowest band. To be concrete, let our lattice sites are located at $\mathbf{R}_{m,n} = \mathbf{r_0} + m\mathbf{a_1} + n\mathbf{a_2}$ where $\mathbf{r_0}$

is the origin and $\mathbf{a_1}, \mathbf{a_2}$ are primitive lattice vectors. Let us define region $A_{m,n}$ as $A_{m,n} = \{\mathbf{r}|[(\mathbf{r}-\mathbf{r_0})\cdot\mathbf{a_1}] = m, [(\mathbf{r}-\mathbf{r_0})\cdot\mathbf{a_2}] = n\}$ where $[x]$ indicates the largest integer smaller than or equal to x. For a given potential $V(\mathbf{r})$, we numerically solve the Schrodinger equation

$$H = -\frac{1}{2M}\nabla^2 + V(\mathbf{r}) \tag{3.7}$$

with the standard finite difference method with the meshes divided in the directions of $\mathbf{a_1}$ and $\mathbf{a_2}$. We solve this equation over each $A_{m,n}$ with the periodic boundary conditions, and take the ground state wavefunction $\psi_{mn}(\mathbf{r})$ and set it vanishes outside of $A_{m,n}$. Now we construct a large region $\mathcal{A} = \mathcal{A}_{(m_1,n_1)(m_2,n_2)} \equiv \bigcup_{m=m_1}^{m_2}\bigcup_{n=n_1}^{n_2} A_{mn}$. Denote $Q_1 = m_2 - m_1 + 1$, $Q_2 = n_2 - n_1 + 1$, and $Q = Q_1Q_2$. By solving Eq. (3.7) over $\mathcal{A}_{(m_1,n_1)(m_2,n_2)}$ with the periodic boundary conditions, we obtain the s-th lowest state wavefunction $\Psi_s(\mathbf{r})$ for $s = 1, \cdots, Q$. Also we order the lattice sites in this large region as $(m,n) \to l = (m-1)Q_2 + n$. Now we construct a $Q \times Q$ matrix M such that

$$M'_{ls} = \int_{A_l} \Psi_l^*(\mathbf{r})\Psi_s(\mathbf{r})d^2\mathbf{r}, \qquad M_{ls} = M'_{ls}\left(\sum_{t=1}^{Q}|M'_{ts}|^2\right)^{-1/2}. \tag{3.8}$$

For each unit vector $\mathbf{h_i}$ such that $(\mathbf{h_i})_j = \delta_{ij}$, we find $\mathbf{g_i} = M^{-1}\mathbf{h_i}$. Then we define our pseudo Wannier function for stie i as

$$\mathcal{W}_i(\mathbf{r}) = \sum_{s=1}^{Q}(\mathbf{g_i})_s\Psi_s(\mathbf{r}). \tag{3.9}$$

Note that for a periodic potential $V(\mathbf{r}) = V(\mathbf{r}+\mathbf{a_1}) = V(\mathbf{r}+\mathbf{a_2})$, this expression represent exact Wannier functions which satisfy $\int_{\mathcal{A}} \mathcal{W}_i^*(\mathbf{r})\mathcal{W}_j(\mathbf{r})d^2\mathbf{r} = \delta_{ij}$.

To find the tunneling strengths between sites (m,n) and $(m+1,n)$, we find the pseudo Wannier function for the large region $\mathcal{A} = \mathcal{A}_{(m-1,n-1)(m+2,n+1)}$. Then the tunneling strength between these sites are given by

$$J_{(p,q)(p+1,q)} = \left| \int_{\mathcal{A}} \mathcal{W}^*_{m+1,n}(\mathbf{r}) \left[-\frac{1}{2M}\nabla^2 + V(\mathbf{r}) \right] \mathcal{W}_{m,n}(\mathbf{r}) d^2\mathbf{r} \right|. \tag{3.10}$$

To apply this method to our checker board lattice, we set $\mathbf{a_1} = a\hat{\mathbf{x}} + a\hat{\mathbf{y}}$, $\mathbf{a_2} = -a\hat{\mathbf{x}} + a\hat{\mathbf{y}}$, and $\mathbf{r_0} = \mathbf{0}$ $(a\hat{\mathbf{x}})$ for the upper (lower) layer. Let us denote the Wannier functions for the upper (lower) layer as $\mathcal{W}^{\uparrow(\downarrow)}_{p,q}(\mathbf{r})$. Intra-layer tunnelings in Fig. 3.2(c) can be evaluated with Eq. (3.10), while we use the potential in Eq. (3.2) with $V_0 = 5E_r$, $V_b = 25E_r$, and $V_r = \sqrt{(V_b + V_0/2)E_r} - \sqrt{V_0 E_r/2}$. We replace the regional function $A(\mathbf{r})$ with a function with the smooth boundary. For example, to target the lattice sites at $pa\hat{\mathbf{x}} + qa\hat{\mathbf{y}}$ ($p = p_1, p_1+1$ and $q = q_1, \cdots, q_2$), we use the following regional function

$$\begin{aligned} A(\mathbf{r}) &= h(x/a, p_1 - d, p_1 + 1 + d, w) h(y/a, q_1 - d, q_2 + d, w), \\ h(s, s_1, s_2, w_s) &= \begin{cases} 1 & \text{if } \left| s - \frac{s_1+s_2}{2} \right| < \frac{s_2 - s_1 - w_s}{2} \\ \frac{1+\sin\{\pi(s-s_1)/w_s\}}{2} & \text{if } |s - s_1| \le w_s/2 \\ \frac{1-\sin\{\pi(s-s_2)/w_s\}}{2} & \text{if } |s - s_2| \le w_s/2 \\ 0 & \text{if } \left| s - \frac{s_1+s_2}{2} \right| > \frac{s_2 - s_1 + w_s}{2} \end{cases} \end{aligned} \tag{3.11}$$

where we set $d = w = 0.1$ in Fig. 3.2(c).

3.6 Details of Supercurrent Flow Generation Simulation

As presented in Eq. (3.4), the mean-field description of the bosonic condensate is given by

$$i\hbar\partial_t\psi_{\mathbf{i}\rho} = -J\sum_{\langle\mathbf{j},\mathbf{k}\rangle}\psi_{\mathbf{j}\bar{\rho}}\delta_{\mathbf{ik}} - J\sum_{[\mathbf{j},\mathbf{k}]}\psi_{\mathbf{j}\rho}\delta_{\mathbf{ik}} + \left\{V_\rho(i_x,i_y,t) - \mu + U\left|\psi_{\mathbf{i}\rho}\right|^2\right\}\psi_{\mathbf{i}\rho}. \quad (3.12)$$

Here, $\psi_{\mathbf{i}\rho}$ is the condensate wave function at site $\mathbf{i} = (i_x, i_y)$ on layer ρ, where $i_x + i_y$ must be even (odd) for $\rho =\uparrow (\downarrow)$. $\bar{\rho} =\downarrow (\uparrow)$ for $\rho =\uparrow (\downarrow)$. $\langle\mathbf{j},\mathbf{k}\rangle$ indicate the nearest neighboring pairs of sites $\mathbf{j},\mathbf{k}$ that intersect with the line defects. $[\mathbf{j},\mathbf{k}]$ indicate pairs of sites $\mathbf{j},\mathbf{k}$ such that $|\mathbf{j}-\mathbf{k}|^2 = 2$ where the pairs do not intersect with the line defects. J is the tunneling strength, U is the on-site interaction energy, V_ρ is the stirring potential on layer ρ, and μ is the chemical potential.

For the numerical simulations in Fig. 3.3, the condensate wavefunction is initially prepared as the static solution of Eq. (3.12) for $V_\rho(i_x,i_y,t) = 0$ on a 120×120 square lattice so that the lattice site i_x, i_y is located at $x = (i_x-0.5)a, y = (i_y-0.5)a$. We set $\mu = 30J$ and $U = 0.004J$. The line defects are located at $x = 40a$ and $x = 80a$ for $y \in [40a, 80a]$. For the stirring sequences along the non-contractible

loop L_1, the stirring potential is set to be

$$V_\rho(i_x,i_y,t)|_{L_1} = V_0 R_1(t) \sum_{C=A,B} e^{-\{((i_x-0.5)a-X_{C,\rho}(t))^2+((i_y-0.5)a-Y_{C,\rho}(t))^2\}/(2r_0^2)},$$

$$R_1(t) = \begin{cases} t/\tau_1' & 0 \le t < \tau_1' \\ 1 & \tau_1' \le t < \tau_1 - \tau_1' \\ (\tau_1 - t)/\tau_1' & \tau_1 - \tau_1' \le t < \tau_1 \\ 0 & \tau_1 \le t \end{cases}, \quad \bar{t} = \mathrm{mod}(t,T),$$

$$X_{A,\uparrow}(t) = \begin{cases} x_1 + v\bar{t} & 0 \le \bar{t} < T_x \\ x_2 & T_x \le \bar{t} < T_x + T_y \\ x_2 - v(\bar{t} - T_x - T_y) & T_x + T_y \le \bar{t} < 2T_x + T_y \\ x_1 & 2T_x + T_y \le \bar{t} < 2T_x + 2T_y \end{cases},$$

$$Y_{A,\uparrow}(t) = \begin{cases} y_1 & 0 \le \bar{t} < T_x \\ y_1 + v(\bar{t} - T_x) & T_x \le \bar{t} < T_x + T_y \\ y_2 & T_x + T_y \le \bar{t} < 2T_x + T_y \\ y_1 + v(T - \bar{t}) & 2T_x + T_y \le \bar{t} < 2T_x + 2T_y \end{cases},$$

$$X_{B,\uparrow}(t) = 120a - X_{A,\uparrow}(t),\ Y_{B,\uparrow}(t) = Y_{A,\uparrow}(t),\ X_{A,\downarrow}(t) = X_{A,\uparrow}(t),$$

$$Y_{A,\downarrow}(t) = 120a - Y_{A,\uparrow}(t),\ X_{B,\downarrow}(t) = 120a - X_{A,\uparrow}(t),\ Y_{B,\downarrow}(t) = 120a - Y_{A,\uparrow}(t),$$

$$v = \frac{x_2 - x_1 + y_2 - y_1}{T/2},\ T_x = \frac{x_2 - x_1}{v},\ T_y = \frac{y_2 - y_1}{v}. \tag{3.13}$$

Here, $x_1 = 30a$, $x_2 = 50a$, $y_1 = 20a$, $y_2 = 100a$, $r_0 = 10a$. For the sequence that quantized v_1 to 1, $V_0 = 25J$, $\tau_1 = 320J^{-1}$, $\tau_1' = 32J^{-1}$, $T = 640J^{-1}$. For the sequence that quantized v_1 to 2, $V_0 = 26J$, $\tau_1 = 265J^{-1}$, $\tau_1' = 26.5J^{-1}$, $T = 530J^{-1}$.

The stirring potential for the sequences along the non-contractible loop L_2 is

$$V_\rho(i_x,i_y,t)|_{L_1} = V_0 R_2(t)\sum_{\rho'} S_{\rho\rho'}(t) \times \sum_{C=A,B} e^{-\{((i_x-0.5)a-X_{C,\rho'}(t))^2+((i_y-0.5)a-Y_{C,\rho'}(t))^2\}/(2r_0^2)},$$

$$R_2(t) = \begin{cases} t/\tau_2' & 0 \le t < \tau_2' \\ 1 & \tau_2' \le t < \tau_2 - \tau_2' \\ (\tau_2 - t)/\tau_2' & \tau_2 - \tau_2' \le t < \tau_2 \\ 0 & \tau_2 \le t \end{cases}, \qquad \bar{t} = \mathrm{mod}(t,T),$$

$$S_{\uparrow\uparrow}(t) = \begin{cases} \frac{1}{2} - (v\bar{t} - 40a + x_1)/\Delta & |40a - x_1 - v\bar{t}| \le \Delta/2 \\ 0 & |60a - x_1 - v\bar{t}| \le 20a - \Delta/2 \\ \frac{1}{2} + (v\bar{t} - 80a + x_1)/\Delta & |80a - x_1 - v\bar{t}| \le \Delta/2 \\ 1 & \text{elsewhere} \end{cases},$$

$$X_{A,\uparrow}(t) = \begin{cases} x_1 + v\bar{t} & 0 \le \bar{t} < T_x \\ x_2 & T_x \le \bar{t} < T_x + T_y \\ x_2 - v(\bar{t} - T_x - T_y) & T_x + T_y \le \bar{t} < 2T_x + T_y \\ x_1 & 2T_x + T_y \le \bar{t} < 2T_x + 2T_y \end{cases},$$

$$Y_{A,\uparrow}(t) = \begin{cases} y_1 & 0 \le \bar{t} < T_x \\ y_1 + v(\bar{t} - T_x) & T_x \le \bar{t} < T_x + T_y \\ y_2 & T_x + T_y \le \bar{t} < 2T_x + T_y \\ y_1 + v(T - \bar{t}) & 2T_x + T_y \le \bar{t} < 2T_x + 2T_y \end{cases},$$

$$S_{\downarrow\downarrow}(t) = S_{\uparrow\uparrow}(t),\ S_{\uparrow\downarrow}(t) = S_{\downarrow\uparrow}(t) = 1 - S_{\uparrow\uparrow}(t),$$

$$X_{B,\uparrow}(t) = X_{A,\uparrow}(t),\ Y_{B,\uparrow}(t) = 120a - Y_{A,\uparrow}(t),\ X_{A,\downarrow}(t) = 120a - X_{A,\uparrow}(t),$$

$$Y_{A,\downarrow}(t) = Y_{A,\uparrow}(t),\ X_{B,\downarrow}(t) = 120a - X_{A,\uparrow}(t),\ Y_{B,\downarrow}(t) = 120a - Y_{A,\uparrow}(t),$$

$$v = \frac{x_2 - x_1 + y_2 - y_1}{T/2}\ T_x = \frac{x_2 - x_1}{v},\ T_y = \frac{y_2 - y_1}{v}. \tag{3.14}$$

Here, $x_1 = 20a$, $x_2 = 100a$, $y_1 = 70a$, $y_2 = 90a$. For the sequence that quantized v_2 to 1, $V_0 = 18J$, $\tau_1 = 335J^{-1}$, $\tau_1' = 33.5J^{-1}$, $T = 670J^{-1}$. For the sequence that quantized v_2 to 2, $V_0 = 18J$, $\tau_1 = 320J^{-1}$, $\tau_1' = 32J^{-1}$, $T = 640J^{-1}$.

3.7 Laser-assisted Tunneling and Quantum Hall Hamiltonian

The Hamiltonian of the checker board lattice with a linear potential gradient is described by

$$H_0 = \sum_n n_y \Delta \left|W_n\right\rangle \left\langle W_n\right| - J_0 \left(\left|W_{n_x-1,n_y+1}\right\rangle \left\langle W_n\right| + \left|W_{n_x+1,n_y+1}\right\rangle \left\langle W_n\right| + \text{H.c.}\right), \tag{3.15}$$

where $|W_n\rangle = |W_{n_x,n_y}\rangle$ is the Wannier state at site $n = (n_x, n_y)$. In the limit that $J_0 \ll \Delta$, this Hamiltonian can be diagonalized as

$$H_0 = \sum_n n_y \Delta \left|n\right\rangle \left\langle n\right| + O\left(\frac{J_0^2}{\Delta}\right),$$
$$\text{where} \quad \left|n\right\rangle = \left|n_x, n_y\right\rangle \equiv \left|W_{n_x,n_y}\right\rangle + \sum_{p=\pm 1} \sum_{q=\pm 1} \frac{qJ_0}{\Delta} \left|W_{n_x+p,n_y+q}\right\rangle. \tag{3.16}$$

Now we apply a pair of Raman beams with detuning Δ and the momentum kick of $\delta\mathbf{k} = \delta k\hat{\mathbf{x}}$, $\delta ka \bmod 2\pi = \phi/2$. The time-dependent dipole potential by this beam

pair is $V(\mathbf{r},t) = \Omega\cos(\delta k x - \Delta t - \theta)$. By considering a transformation to a rotating frame $U = \exp(iHt)$, relevant components of this potential are $\langle n_x \pm 1, n_y + 1|V|n\rangle = (J_0/2\Delta)(e^{\pm i\delta k a} - 1)\left[e^{i(n_x\phi/2 - \Delta t - \theta)} + \text{c.c.}\right]$. In the perturbative Raman beam regime ($\Omega \ll \Delta$), we can get following effective Hamiltonian,

$$\begin{aligned} H_{\text{eff}} &= U(H+V)U^\dagger + i\left(\partial_t U\right)U^\dagger\Big|_{\Omega\ll\Delta} \\ &= \sum_n \sum_{p=\pm 1} e^{i\Delta t}\left\langle n_x + p, n_y + 1|V|n\right\rangle |n_x + p, n_y + 1\rangle\langle n| + \text{H.c.}\Big|_{\Omega\ll\Delta} \\ &= \sum_n \sum_{p=\pm 1} \frac{\Omega J_0}{\Delta}\sin\left(\frac{\delta k a}{2}\right) \\ &\qquad \times e^{i[n_x\phi/2 - \theta + p(\delta k a + \pi)/2]}|n_x + p, n_y + 1\rangle\langle n| + \text{H.c.}, \end{aligned} \tag{3.17}$$

which is equivalent to the non-interacting part of Eq. (3.6) in the region except line defects, up to some irrelevant constant phases.

3.8 Braiding of Twist Defects

To deal with a surface with $g+1$ pairs of twist defects, let us label the twist defects and non-contractible loops as in Fig. 3.5(a). Here, we only consider the twist defects and loops with natural number indices. With this convention, one can see that the counter-clockwise braiding of twist defect p and q, $R_{p,q} = R_{q,p}$, acts on each non-contractible loop as following:

$$\begin{aligned} R_{2k-1,2k} &: \begin{cases} \beta_{k-1} \to \beta_{k-1} + \alpha_{k-1} - \alpha_k \\ \beta_k \to \beta_k - \alpha_{k-1} + \alpha_k \end{cases} \quad (1 \le k \le g+1), \\ R_{2k,2k+1} &: \alpha_k \to \alpha_k - \beta_k \ (1 \le k \le g), \end{aligned} \tag{3.18}$$

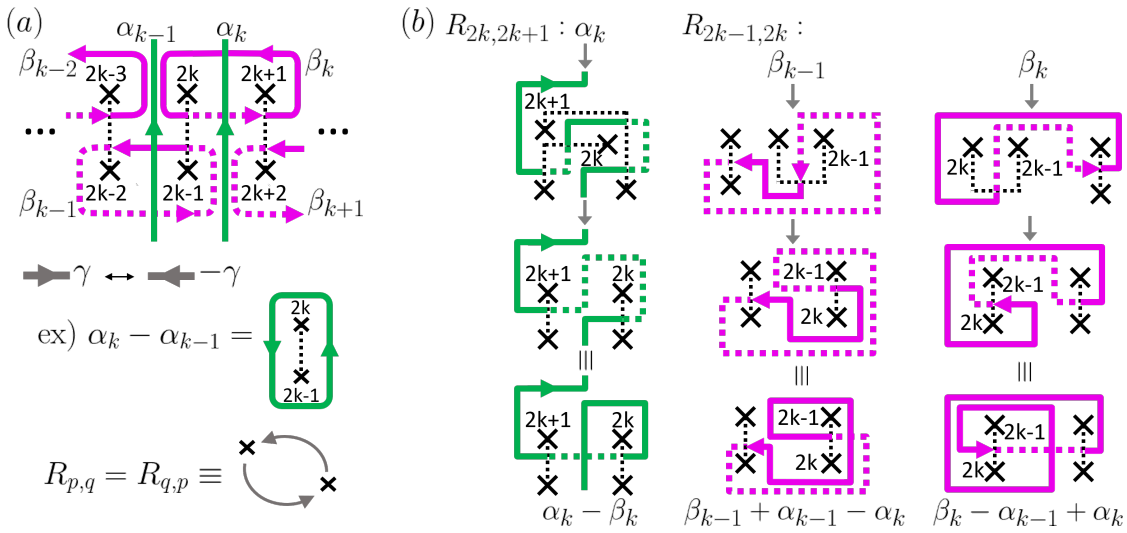

Figure 3.5: (a) Non-contractible loops around twist defects. (b) Transformation of non-contractible loops under the braiding of neighboring twist defects.

while other loops remain unchanged and $\alpha_0 = \beta_0 = \alpha_{g+1} = \beta_{g+1} = 0$. Also, braiding of distant twist defects can be expressed as

$$R_{i,j} = R^{-1}_{i,i+1} \cdots R^{-1}_{j-2,j-1} R_{j,j-1} \cdots R_{i+1,i} \ (i < j). \tag{3.19}$$

To see how these braiding operations change the FQH ground states in detail, let us consider the Laughlin states with filling fraction $\nu = 1/m$ from now on. If we denote the Wilson loop operator along the loop γ as $W(\gamma)$, $W(\gamma)W(\gamma') = \exp[-i(2\pi/m)]W(\gamma')W(\gamma)$ if γ pass through γ' from the left to the right. Therefore,

$$W(\alpha_i)W(\beta_j) = \exp[-i(2\pi/m)\delta_{ij}]W(\beta_j)W(\alpha_i), \tag{3.20}$$

where all the other pairs of Wilson loop operators commute to each other. Then W^m

commutes with any Wilson loop operator, so we can consider $W^m = \not\Vdash$. Since Wilson loop operator is unitary, eigenvalues of any W are restricted to $e^{i2\pi n/m}, n \in \mathbb{Z}_m$. Then we can choose bases for the ground states as

$$
\begin{aligned}
W(\alpha_i)\left|\cdots, n_j, \cdots\right\rangle_\alpha &= e^{i2\pi n_j/m}\left|\cdots, n_j, \cdots\right\rangle_\alpha, \\
W(\beta_i)\left|\cdots, n_j, \cdots\right\rangle_\alpha &= \left|\cdots, n_j - 1 \bmod m, \cdots\right\rangle_\alpha, \\
W(\alpha_i)\left|\cdots, n_j, \cdots\right\rangle_\beta &= \left|\cdots, n_j + 1 \bmod m, \cdots\right\rangle_\beta, \\
W(\beta_i)\left|\cdots, n_j, \cdots\right\rangle_\beta &= e^{i2\pi n_j/m}\left|\cdots, n_j, \cdots\right\rangle_\beta,
\end{aligned}
\tag{3.21}
$$

for $j = 1, \cdots, g, \quad n_j \in \mathbb{Z}_m$. Let $U_{p,q}$ be the unitary operation acts on the ground states by performing the braiding $R_{p,q}$. Since $R_{2k,2k+1} : \alpha_k \to \alpha_k - \beta_k$,

$$
\begin{aligned}
& U_{2k,2k+1} W(\alpha_k) U_{2k,2k+1}^\dagger = e^{i\chi} W(\alpha_k) W^\dagger(\beta_k) \\
& \to \ (\mathbb{Z}_2 \text{ layer-exchange symmetry}) \ \to \\
& U_{2k,2k+1} W^\dagger(\alpha_k) U_{2k,2k+1}^\dagger = e^{i\chi} W^\dagger(\alpha_k) W(\beta_k) \\
& \leftrightarrow \ U_{2k,2k+1} W(\alpha_k) U_{2k,2k+1}^\dagger = e^{-i(\chi + 2\pi/m)} W(\alpha_k) W^\dagger(\beta_k) \\
& \to e^{i2\chi} = e^{-i2\pi/m}, \quad \chi = r\pi - \pi/m \ (r \in \mathbb{Z}).
\end{aligned}
\tag{3.22}
$$

Since $W(\alpha)^m = W(\beta)^m = I$,

$$\begin{aligned} U_{2k,2k+1} W(\alpha_k)^m U_{2k,2k+1}^\dagger &= e^{im\chi} \left[W(\alpha_k) W^\dagger(\beta_k) \right]^m \\ &= e^{im\chi} e^{-i(2\pi/m)[m(m-1)/2]} W(\alpha_k)^m W^\dagger(\beta_k)^m \\ &= e^{i\pi m(r-1)} = U_{2k,2k+1} U_{2k,2k+1}^\dagger = I, \end{aligned} \tag{3.23}$$

so we can choose any r such that $r \equiv m \bmod 2$. Without loss of generality, we set $r = m$. Now this braiding acts non-trivially only on $\{|n_k\rangle_\beta \equiv |\cdots, n_k, \cdots\rangle_\beta \, | n_k \in \mathbb{Z}_m\}$, so

$$\begin{aligned} U_{2k,2k+1} |n_k\rangle_\beta &= U_{2k,2k+1} W(\alpha_k) |n_k - 1\rangle_\beta = e^{i\chi} W(\alpha_k) W^\dagger(\beta_k) U_{2k,2k+1} |n_k - 1\rangle_\beta \\ &= e^{in_k\chi} \left[W(\alpha_k) W^\dagger(\beta_k) \right]^{n_k} |0\rangle_\beta \\ &= e^{in_k\chi} e^{i(2\pi/m)[n_k(n_k+1)/2]} W^\dagger(\beta_k)^{n_k} W(\alpha_k)^{n_k} |0\rangle_\beta \\ &= e^{-i\pi(n_k^2/m + m n_k)} |n_k\rangle_\beta , \end{aligned} \tag{3.24}$$

with $U_{2k,2k+1} |0\rangle_\beta = |0\rangle_\beta$. We may repeat this procedure for braiding $R_{2k-1,2k}$ as

well,

$$U_{2k-1,2k}W(\beta_{k-1})U^{\dagger}_{2k-1,2k} = e^{i\chi'}W(\beta_{k-1})W(\alpha_{k-1})W^{\dagger}(\alpha_k)$$

$$\rightarrow \text{ ($\mathbb{Z}_2$ layer-exchange symmetry) } \rightarrow$$

$$U_{2k-1,2k}W^{\dagger}(\beta_{k-1})U^{\dagger}_{2k-1,2k} = e^{i\chi'}W^{\dagger}(\beta_{k-1})W^{\dagger}(\alpha_{k-1})W(\alpha_k)$$

$$\leftrightarrow U_{2k-1,2k}W(\beta_{k-1})U^{\dagger}_{2k-1,2k} = e^{-i(\chi'+2\pi/m)}W(\beta_{k-1})W(\alpha_{k-1})W^{\dagger}(\alpha_k)$$

$$\rightarrow e^{i2\chi'} = e^{-i2\pi/m}, \quad \chi' = r\pi - \pi/m \ (r \in \mathbb{Z}), \tag{3.25}$$

$$U_{2k-1,2k}W(\beta_{k-1})^m U^{\dagger}_{2k-1,2k} = e^{im\chi'}\left[W(\beta_{k-1})W^{\dagger}(\alpha_{k-1})\right]^m W^{\dagger}(\alpha_k)^m$$

$$= e^{im\chi}e^{i(2\pi/m)[m(m+1)/2]}W(\beta_{k-1})^m W^{\dagger}(\alpha_{k-1})^m W^{\dagger}(\alpha_k)^m$$

$$= e^{i\pi[m(r-1)+2]} = U_{2k,2k+1}U^{\dagger}_{2k,2k+1} = I, \tag{3.26}$$

so set $r = m$ again without loss of generality. These results hold for $k-1 \leftrightarrow k$. This braiding acts non-trivially only on $\{|n_{k-1}, n_k\rangle_\alpha \equiv |\cdots, n_{k-1}, n_k, \cdots\rangle_\alpha | n_{k-1}, n_k \in$

$\mathbb{Z}_m\}$, so

$$
\begin{aligned}
& U_{2k-1,2k} \left|n_{k-1}, n_k\right\rangle_\alpha \\
&= U_{2k-1,2k} W(\beta_{k-1}) \left|n_{k-1}+1, n_k\right\rangle_\alpha \\
&= e^{i\chi'} W(\beta_{k-1}) W(\alpha_{k-1}) W^\dagger(\alpha_k) U_{2k-1,2k} \left|n_{k-1}+1, n_k\right\rangle_\alpha \\
&= e^{i(m-n_{k-1})\chi'} \left[W(\beta_{k-1}) W(\alpha_{k-1}) W^\dagger(\alpha_k)\right]^{m-n_{k-1}} U_{2k-1,2k} \left|0, n_k\right\rangle_\alpha \\
&= e^{i(2m-n_{k-1}-n_k)\chi'} \left[W(\beta_{k-1}) W(\alpha_{k-1}) W^\dagger(\alpha_k)\right]^{m-n_{k-1}} \\
&\quad \times \left[W(\beta_k) W(\alpha_k) W^\dagger(\alpha_{k-1})\right]^{m-n_k} \left|0,0\right\rangle_\alpha \\
&= e^{i(2m-n_{k-1}-n_k)\chi'} e^{i(2\pi/m)[(m-n_{k-1})(m-n_{k-1}+1)/2]} e^{i(2\pi/m)[(m-n_k)(m-n_k+1)/2]} \\
&\quad \times W(\alpha_{k-1})^{m-n_{k-1}} W(\beta_{k-1})^{m-n_{k-1}} W^\dagger(\alpha_k)^{m-n_{k-1}} \\
&\quad \times W(\alpha_k)^{m-n_k} W(\beta_k)^{m-n_k} \left|0,0\right\rangle_\alpha \\
&= e^{i\pi[n_{k-1}^2/m + n_{k-1}^2/m - m(n_{k-1}+n_k)]} \\
&\quad \times W(\alpha_{k-1})^{m-n_{k-1}} W(\beta_{k-1})^{m-n_{k-1}} e^{i2\pi n_k(n_{k-1}-n_k)/m} \left|0, n_k\right\rangle_\alpha \\
&= e^{i\pi[n_{k-1}^2/m + n_{k-1}^2/m - m(n_{k-1}+n_k)]} e^{i2\pi n_{k-1}(m-n_{k-1})/m} e^{i2\pi n_k(n_{k-1}-n_k)/m} \left|n_{k-1}, n_k\right\rangle_\alpha \\
&= e^{-i\pi[(n_{k-1}+n_k)^2/m + m(n_{k-1}+n_k)]} \left|n_{k-1}, n_k\right\rangle_\alpha
\end{aligned}
\tag{3.27}
$$

with $U_{2k-1,2k} \left|0,0\right\rangle_\alpha = \left|0,0\right\rangle_\alpha$.

As the simplest example, consider the case of $\nu = 1/2$ Laughlin states with two pairs of twist defects. Then the braiding operations become

$$
\begin{aligned}
U_{1,2} &= \left|0\right\rangle\left\langle 0\right|_\alpha - i\left|1\right\rangle\left\langle 1\right|_\alpha = \frac{1-i}{2}\left(\left|0\right\rangle\left\langle 0\right|_\beta + \left|1\right\rangle\left\langle 1\right|_\beta\right) + \frac{1+i}{2}\left(\left|0\right\rangle\left\langle 1\right|_\beta + \left|1\right\rangle\left\langle 0\right|_\beta\right), \\
U_{2,3} &= \left|0\right\rangle\left\langle 0\right|_\beta - i\left|1\right\rangle\left\langle 1\right|_\beta .
\end{aligned}
\tag{3.28}
$$

3.9 Outlook

While we considered bilayer square lattice in this work, similar optical lattice construction may be created for different bilayer lattice geometries and twist defects within them. Such variety in lattice geometry would help to realize different kinds of lattice models on the topologically non-trivial surface.

Presence of long-ranged interactions, such as Rydberg interaction [163] or dipole interaction between polar molecules [164], can also help creating various quantum many-body states. For example, the presence of interaction between different spins on a FQH Hamiltonian can help generating Halperin states [165] which can have ground state degeneracy not accessible by Laughlin states [146, 147].

With further efforts in engineering different geometries and interactions, one may construct a Hamiltonian hosting non-Abelian states such as the Kitaev model [76]. If such non-Abelian states are prepared, the presence twist defects and braiding operations of them can realize the universal topological quantum computation [147].

Chapter 4: Optical Imprinting of Superlattices in Two-dimensional Materials

4.1 Introduction

A superlattice structure in two-dimensional (2D) materials has opened a new way to engineer electronic bands, starting with the investigation on a honeycomb superlattice structure in monolayer graphene [166]. Recently, Moiré pattern in a twisted-bilayer van der Waals heterostructure has been immensely successful in generating a variety of band structures, including Hofstadter butterfly [167, 168] and flat bands [169–173]. These bands can induce intriguing strongly correlated phases such as fractional Chern insulator [168], anomalous Hall phase [174, 175], Mott insulating phase [173, 176–178], nontrivial magnetic phases [174, 179–181], and superconductivity [172, 178, 182–184]. Yet, this passive way of creating a superlattice has been largely limited by the microscopic structure of the 2D materials since different samples should be prepared for different superlattice structures. Therefore, it is interesting to find alternative ways to synthesize a spatiotemporal structure in 2D materials.

At the same time, the recent progress in the beam-shaping technique has en-

abled the generation of arbitrary beam patterns with high resolution comparable to the optical wavelengths [94, 98–100, 119, 185], which already found remarkable successes in ultracold-atom systems [24–28]. This wide tunability of light can be naturally applied to 2D electronic systems to imprint arbitrary superlattices, regardless of the underlying microscopic lattice structure. This is particularly interesting in the context of the "Floquet topological insulator," where the illumination of circularly polarized (CP) light can turn a trivial system into a topological insulator [186–195].

In this chapter, we propose a method to create superlattice structures in a 2D material by shining spatially periodic laser beams, as schematically shown in Fig. 5.1. We illustrate the idea with an example of monolayer graphene irradiated by a circularly polarized beam with a superlattice structure, where the beam amplitude is spatially periodic. To demonstrate the tunability of this superlattice structure and unique physics originating from the superlattice, we first study the case of a square superlattice and explore the topological phase transition induced by varying the superlattice size. Then, we investigate the topological phase transitions, when the square superlattice is sheared to a stretched hexagonal one. In particular, we examine the relationship between this topological phase transition and the role of lattice geometry in creating complex tunneling phases. Further, we demonstrate the possibility of creating more exotic lattices by superposing multiple lattices, with an example of tuning between a hexagonal and a kagome lattice where the flat bands can be obtained. These flat bands particularly can harbor strongly correlated phenomena in Floquet systems.

4.2 Graphene with Spatially Patterned Light

Let us consider a monolayer graphene with the inter-atomic distance a and the tight-binding energy t between the nearest neighbors. The low-energy description for this monolayer graphene under the electromagnetic field $\mathbf{A}(\mathbf{r}, t)$ is given by

$$H = v\left[\mathbf{p} + e\mathbf{A}(\mathbf{r}, t)\right] \cdot \left(\tau_z \sigma_x \hat{\mathbf{x}} + \sigma_y \hat{\mathbf{y}}\right), \tag{4.1}$$

where $\sigma_x, \sigma_y, \sigma_z$ are Pauli matrices acting on sublattice degrees of freedom, $v = (3/2)ta$ is the Fermi velocity at Dirac points, and $\tau_z = \pm 1$ is the valley index [196]. In particular, if we shine the CP beam with spatial amplitude pattern $\mathbf{A}(\mathbf{r}, t) = A_0(\mathbf{r})e^{i\omega t}(\hat{\mathbf{x}} + i\hat{\mathbf{y}}) + \text{c.c.}$ (Fig. 5.1), the effective Floquet Hamiltonian to the first order in ω^{-1} becomes [78–81, 186, 197–199]

$$H_{\text{eff}} = v(\tau_z p_x \sigma_x + p_y \sigma_y) + \tau_z \frac{4e^2 v^2}{\omega} \left|A_0(\mathbf{r})\right|^2 \sigma_z. \tag{4.2}$$

We denote the peak amplitude of $A_0(\mathbf{r})$ as $\mathcal{A}_0$. Then, Eq. (4.2) becomes a valid description when frequency ω is high enough ($\omega \gg ev\mathcal{A}_0$) and the amplitude varies in length scale larger than a ($\mathcal{A}_0/\max\{|\nabla A_0(\mathbf{r})|\} \gg a$). For brevity, we set $\hbar = 1$ from here on.

We specifically study the superlattice structure created by a spatially periodic amplitude $|A_0(\mathbf{r})| = |A_0(\mathbf{r} + \mathbf{L}_1)| = |A_0(\mathbf{r} + \mathbf{L}_2)|$. While the 2D material with spatially modulated beams has been studied in the different contexts [200–202],

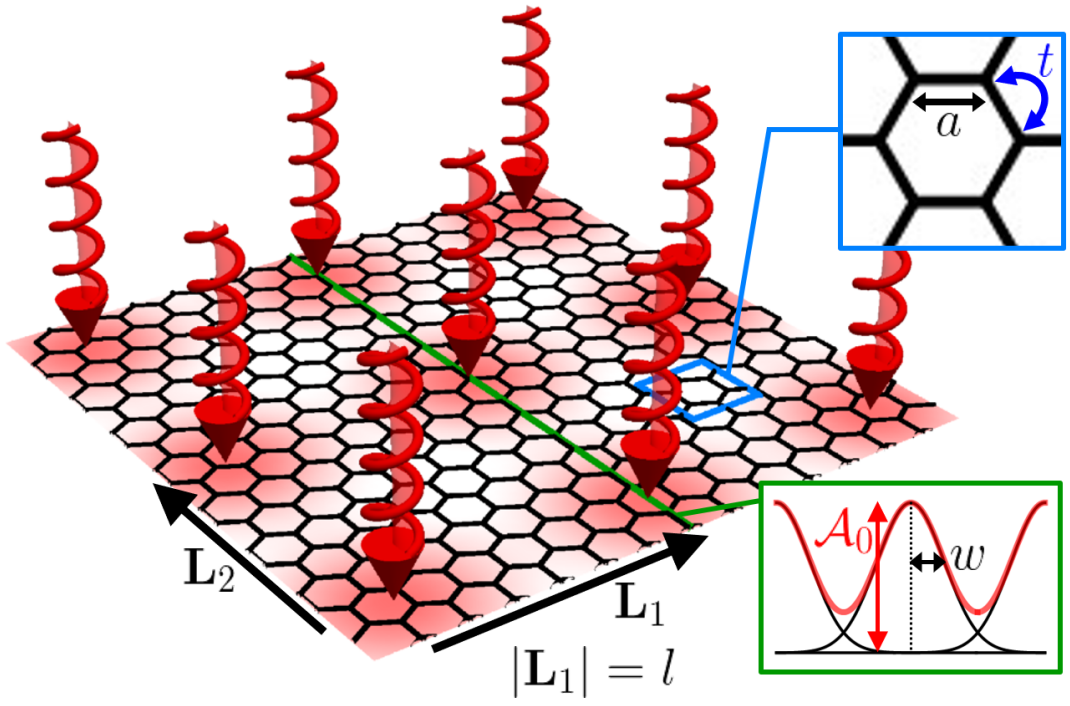

Figure 4.1: A 2D material irradiated by a spatially periodic CP light with frequency ω. Here, we use the example of a monolayer graphene. The superposition of multiple CP Gaussian beams generates a periodic amplitude pattern $A_0(\mathbf{r})$ with translation vectors $\mathbf{L}_1$ and $\mathbf{L}_2$. $|\mathbf{L}_1| = l$. Upper inset: We denote the interatomic distance of the graphene as a and the tight-binding energy between the nearest neighbors as t. Lower inset: Each Gaussian beam has a peak amplitude $\mathcal{A}_0$ and a half waist w (black lines). The overall beam amplitude (red line) results from the superposition of the Gaussian beams.

here we investigate the generation of a superalttice with spatially periodic beams. In particular, to make the beam experimentally relevant, we consider the superposition of CP Gaussian beams positioned on the superlattice,

$$A_0(\mathbf{r}) = \sum_{n_1,n_2} \mathcal{A}_0 \exp\left(-\frac{|\mathbf{r} - n_1\mathbf{L}_1 - n_2\mathbf{L}_2|^2}{2w^2}\right), \tag{4.3}$$

where w is the radius of each Gaussian beam. This beam configuration is achievable with recent progress in beam-shaping technologies [94, 98–100, 119, 185]. For the

cases $|\mathbf{L}_1|, |\mathbf{L}_2| = l \gg a$, the Brillouin-zone folding occurs on a momentum scale $1/l$. Furthermore, the hybridization of Floquet sidebands is suppressed for $v/l \ll \omega$ so that the low-energy description is captured by Eq. (4.2) (see Appendix A). We obtain Bloch eigenstates $|\psi_{m,\mathbf{k}}\rangle$ and eigenenergies $E_{m,\mathbf{k}}$, where m is the band index and $\mathbf{k}$ is the crystal momentum within the Brillouin zone set by reciprocal lattice vectors of $\mathbf{L}_1$ and $\mathbf{L}_2$. Note that Eq. (4.2) preserves particle-hole symmetry ($\sigma_x H^*_{\text{eff}} \sigma_x = -H_{\text{eff}}$) and therefore the energy spectrum is symmetric with respect to the zero energy. Also, $\sigma_y H_{\text{eff}} \sigma_y = H_{\text{eff}}|_{\tau_z \to -\tau_z}$, so two valleys have the same spectrum and eigenstates up to a unitary operation, σ_y. This also ensures that both valleys have the same Chern number. For brevity, let us only consider the $\tau_z = 1$ valley from now on.

4.3 Illumination of Square Superlattice

We first consider the simplest case of a square superlattice, $\mathbf{L}_1 = l\hat{\mathbf{x}}$ and $\mathbf{L}_2 = l\hat{\mathbf{y}}$. Before directly diagonalizing Eq. (4.2), we can make some speculations. First of all, the contribution from the spatial average of $|A_0(\mathbf{r})|$ opens up the gap around the zero energy (Δ_b) as in the case of the graphene under the CP uniform light, where the Chern number, $\mathcal{C}_1$, of the first band above $E = 0$ is nonzero [186–188, 200, 203]. $\mathcal{C}_1$ remains nonzero for small l, as far as the maximum kinetic energy within the Brillouin zone, which is of the order of v/l, is much larger than the spatial Fourier components of the σ_z term in Eq. (4.2), which is of the order of $e^2 v^2 \mathcal{A}_0^2/\omega$. On the other hand, as $l \to \infty$, the contribution of the kinetic term becomes negligible

and therefore the bands become flat. Also, the Bloch wavefunctions look similar regardless of $\mathbf{k}$ and therefore the bands become topologically trivial. Therefore, there must be a topological phase transition where $\mathcal{C}_1$ changes from a nonzero value to zero as we increase l. This topological transition would occur at a superlattice size that makes the two energy scales $e^2v^2\mathcal{A}_0^2/\omega$ and v/l comparable to each other. For a succinct description of this phase transition, we use the rescaled superlattice size

$$\chi = (ve^2\mathcal{A}_0^2/\omega)l \tag{4.4}$$

so that the critical superlattice size χ_c is $O(1)$. Here, χ represents the ratio of the effective superlattice potential over the kinetic energy.

To study the detail of this topological phase transition, we numerically diagonalize Eq. (4.2) as shown in Fig. 5.2(a). Along with the energy spectrum, we present the Chern number $\mathcal{C}$ of each band calculated based on Ref. [204]. In Fig. 5.2, we set $\mathcal{A}_0 = 0.006(ea)^{-1}$, $\omega = 0.06t$, and $w/l = 0.3$. With these parameters, we can check that the topological phase transition occurs at $\chi_c = 0.965$, which is close to 1. This topological transition accompanies the direct gap closing at $\mathbf{k} = \mathrm{M}$ and the band inversion between the first- and second-lowest positive-energy bands. To see this, we compare the particle and current densities of the lowest positive-energy band's wave function at the direct gap closing point. Here, for the Bloch wavefunction of

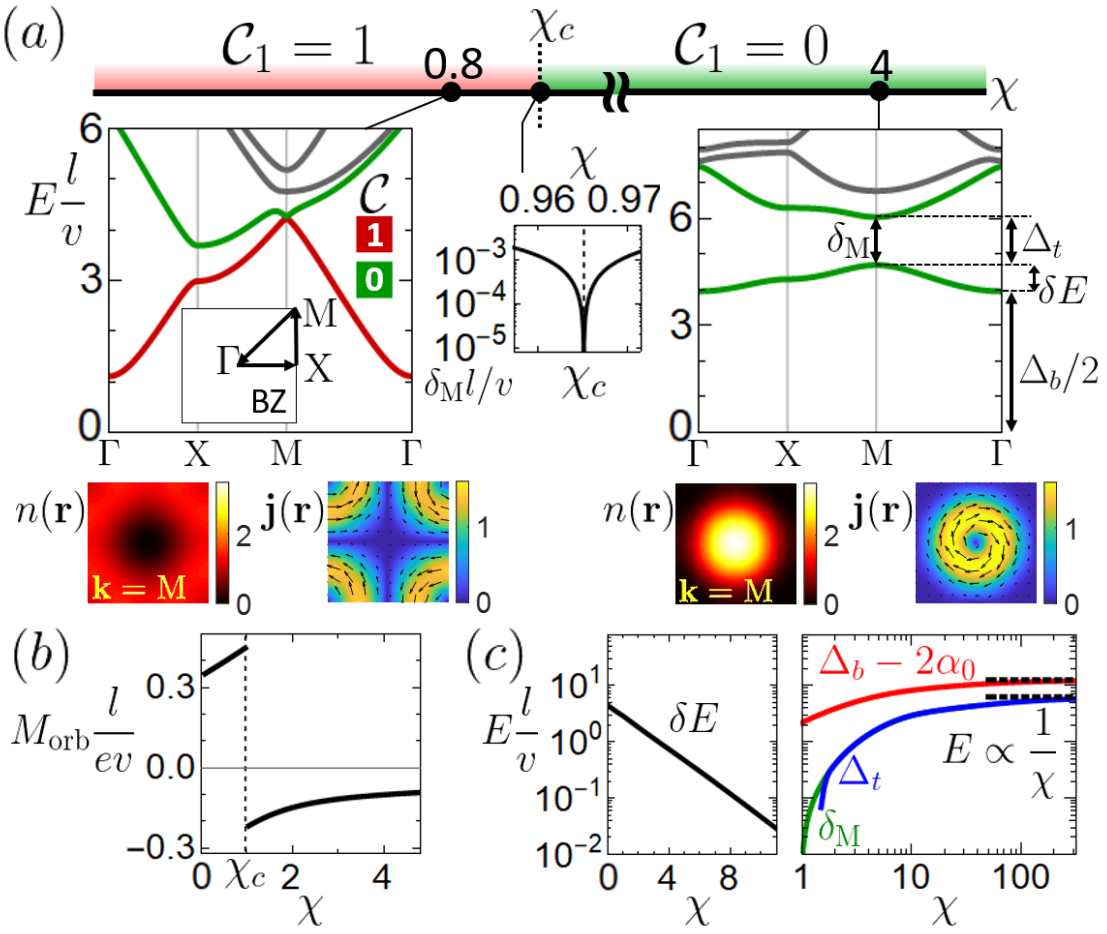

Figure 4.2: (a) Energy spectrum for square superlattices with different superlattice size χ. We set $\mathcal{A}_0 = 0.006(ea)^{-1}$, $\omega = 0.06t$, and $w/l = 0.3$. Only the positive-energy spectrum is shown for simplicity. The Chern numbers of low-lying bands, $\mathcal{C}$, are presented as colors. The topological phase transition occurs at $\chi_c = 0.965$. Upper inset: Direct gap at $\mathbf{k} = \mathrm{M}$ between the first- and the second-lowest positive band (δ_{M}) is plotted in the vicinity of χ_c. Lower insets: The particle density $n(\mathbf{r})$ and current density $\mathbf{j}(\mathbf{r})$ of the Bloch wavefunction of the lowest positive band at $\mathbf{k} = \mathrm{M}$ are shown for $\chi = 0.8 < \chi_c$ and $\chi = 4 > \chi_c$. In the density plots, the centers of the Gaussian beams are located at the corners of the plotted region. The particle density is shown in units of l^{-2}. The amplitude of the current density is presented with the color in units of ev/l^2 and the direction of $\mathbf{j}(\mathbf{r})$ is represented by arrows. (b) Orbital magnetization M_{orb} for the lowest positive band for different superlattice sizes. (c) For the lowest positive band, we plot the energy gap below the band (Δ_b), the energy gap above the band (Δ_t), the direct band gap at $\mathbf{k} = \mathrm{M}$ (δ_M), and the bandwidth (δE) with respect to the superlattice size χ. α_0 is the minimum value of $(4e^2v^2/\omega)|A_0(\mathbf{r})|^2$. The black dashed lines are asymptotic lines showing that El/v is constant, indicating $E \propto \chi^{-1}$.

the mth band, $\psi(\mathbf{r}) = \langle \mathbf{r}|\psi_{m,\mathbf{k}}\rangle$, the particle and current densities are given by

$$\begin{aligned} n(\mathbf{r}) &= \psi^\dagger(\mathbf{r})\psi(\mathbf{r}), \\ \mathbf{j}(\mathbf{r}) &= -e\psi^\dagger(\mathbf{r})\frac{\partial H_{\text{eff}}}{\partial \mathbf{p}}\psi(\mathbf{r}) = -ev\psi^\dagger(\mathbf{r})\left(\sigma_x\hat{\mathbf{x}} + \sigma_y\hat{\mathbf{y}}\right)\psi(\mathbf{r}). \end{aligned} \tag{4.5}$$

The comparison of $n(\mathbf{r})$ and $\mathbf{j}(\mathbf{r})$ before ($\chi = 0.8$) and after ($\chi = 4$) the transition point shows a drastic change in the wave function, which signifies that the band inversion has occurred in the phase transition. In the current density plot, one can also find that the circulation direction of the electron flips as the band inversion occurs. This phenomenon can also be captured in the calculation of the mth band contribution to the orbital magnetization [205–207],

$$M_{\text{orb}} = \text{Im}\int \frac{d^2\mathbf{k}}{(2\pi)^2} e \frac{\partial \langle u_{m,\mathbf{k}}|}{\partial k_x}\left(H_{\mathbf{k}} + E_{m,\mathbf{k}}\right)\frac{\partial |u_{m,\mathbf{k}}\rangle}{\partial k_y}, \tag{4.6}$$

where $|u_{m,\mathbf{k}}\rangle = e^{-i\mathbf{k}\cdot\mathbf{r}}|\psi_{m,\mathbf{k}}\rangle$ and $H_{\mathbf{k}} = e^{-i\mathbf{k}\cdot\mathbf{r}}H_{\text{eff}}e^{i\mathbf{k}\cdot\mathbf{r}}$. In Fig. 5.2(b), one can see that M_{orb} of the lowest positive band shows the sign flip at the phase transition point, agreeing with the observation in the current density plots. We also remark that even if this topological phase transition theoretically exists regardless of the Gaussian beam size, it is desirable to keep w comparable to l for experimental realizations since a fainter superlattice will imply a smaller direct band gap.

This topological phase transition could be experimentally detected in several ways. The change in $\mathcal{C}_1$ causes the difference in the Hall current carried by the chiral edge state, and such difference can be revealed by transport measurements, similar to

Ref. [190]. For the bulk property, one can measure the orbital magnetization, where the sudden jump would be observed at the phase transition shown in Fig. 5.2(b).

As the superlattice size χ increases, the electrons become localized at the local minima of $|A_0(\mathbf{r})|$. This provides an explanation for the exponential suppression of the bandwidth of the lowest positive-energy band (δE) in χ [Fig. 5.2(c)]. For well-localized electrons, the dynamics can effectively be described by a tight-binding model, and the tunneling energy of that model is approximately given by the WKB integrals. This integral decays exponentially with the distance between the superlattice sites, so the bandwidth decreases exponentially as well. The band gaps (Δ_b, Δ_t, δ_M) decay as $O(\chi^{-1})$, where the details of this band gap scaling are explained in the Appendix B.

4.4 Superlattice Shearing

To further investigate the role of the superlattice geometry, let us shear the square superlattice by angle θ so that $\mathbf{L}_1 = l\hat{\mathbf{x}}$ and $\mathbf{L}_2 = l(\tan\theta\hat{\mathbf{x}} + \hat{\mathbf{y}})$. From the perspective of the Floquet Chern insulator created by uniform CP light, in a large superlattice size limit where the tight-binding description is valid, we might interpret the electron tunneling between superlattice sites as the chiral currents around the strongly irradiated region. That is, the paths that these chiral currents flow would give the major contribution to the path integral from one superlattice site to another. In this viewpoint, two superlattice sites can have a *complex* tunneling phase between them if the system has no reflection symmetry along the line con-

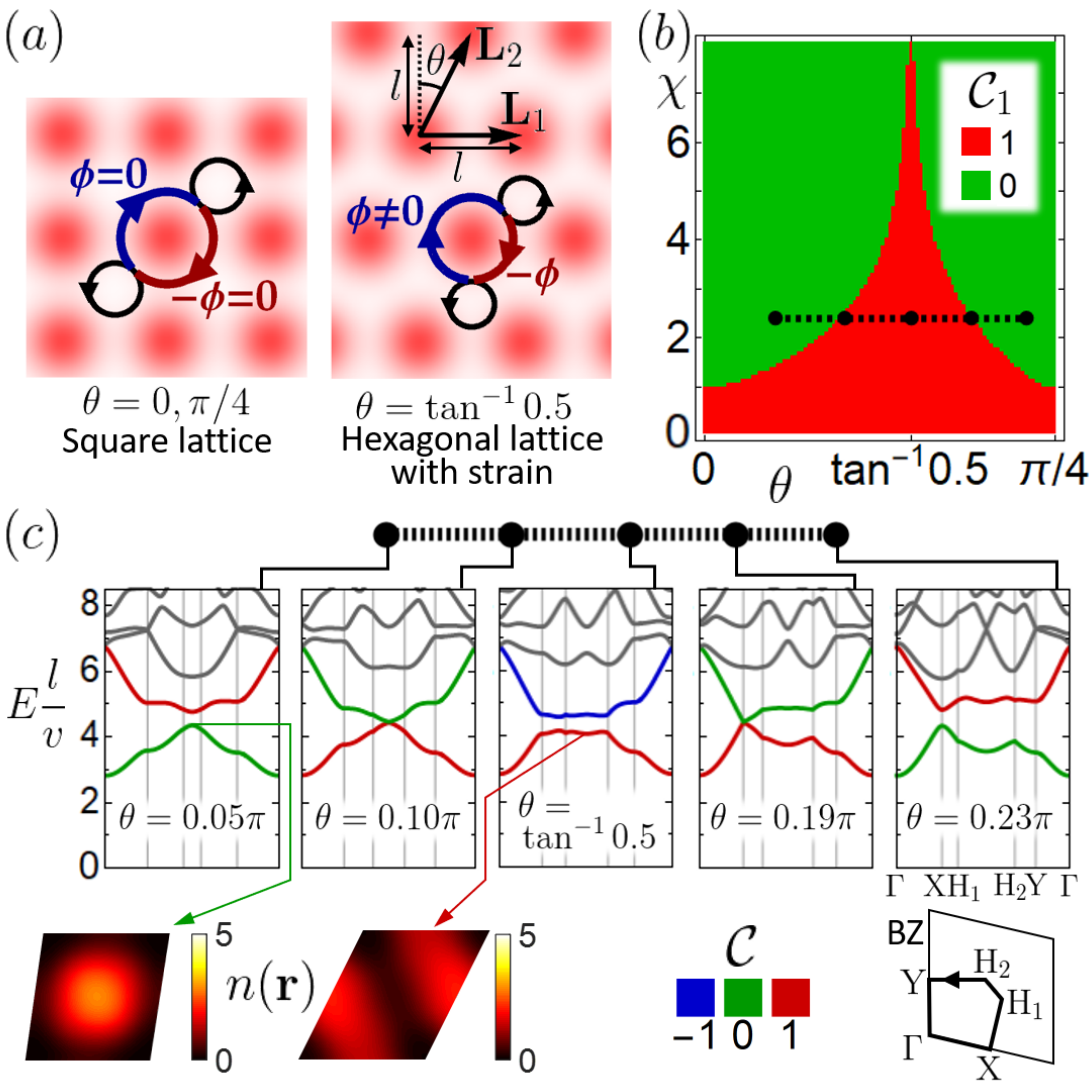

Figure 4.3: (a) We shear a square lattice by angle θ. Tunneling between two sites can be understood as the flow of chiral edge currents around each Gaussian CP beam. If the system has reflection symmetry around the line connecting the two sites, this tunneling should be real. Otherwise, the tunneling can have a complex phase. As examples, the next-nearest-neighbor tunnelings for the $\theta = 0, \pi/4$ case and the $\theta = \tan^{-1}(1/2)$ case are presented. (b) The Chern number of the lowest positive energy band $\mathcal{C}_1$ is shown as a phase diagram between the shearing angle θ and the superlattice size χ. (c) Energy spectra for $\chi = 2.4$ at selected angles are shown where the colors of low-lying bands represent the Chern numbers. The particle density in units of l^{-2} is plotted for angles before and after the phase transition.

necting the two sites [Fig. 5.3(a)], which is analogous to Ref. [16]. Then we can see that the tunneling terms of the tight-binding model for the square lattice ($\theta = 0$ and $\theta = \pi/4$) are real. At angles close to $\theta = \tan^{-1}(1/2)$, the localized electrons form a hexagonal superlattice under a uniform strain and can have complex tunneling phases between the next-nearest neighbors. Then we can construct a tight-binding model for the lowest positive band similar to the Haldane model [208], as explained in the Appendix C. Similar to the Haldane model, a complex tunneling phase in the next-nearest-neighbor tunneling makes $\mathcal{C}_1$ nonzero at this angle. With these considerations, we can predict successive topological phase transitions as we increase θ from 0 to $\pi/4$.

We obtain the phase diagram numerically in Fig. 5.3(b) by calculating the Chern number of the lowest positive-energy band for each value of χ and θ. As we predicted, we can observe the successive topological phase transitions at χ larger than a certain value, which corresponds to the phase transition point described in Fig. 5.2. Another salient feature is that the $\mathcal{C}_1 = 1$ regime very sharply blows up toward the angle $\theta = \tan^{-1}(1/2)$, at which the χ region for $\mathcal{C}_1 = 1$ diverges. This can be explained by combining the fact that the size of tunneling strengths decreases exponentially with the distance between the superlattice points and another fact that the Dirac cones can disappear and the topologically trivial gap opens in the extreme strain (see Appendix C). We can also see that the topological phase transition also accompanies the gap closing and the band inversion, as shown in the particle density plots [Fig. 4.3(c)].

4.5 Hexagonal Lattice to Kagome Lattice

To engineer favorable features such as flatter bands, we can create an even more complicated superlattice by superposing different kinds of lattices. For instance, we consider the superposition of the triangular lattice beam $A_{\text{tri}}(\mathbf{r})$ and the hexagonal lattice beam $rA_{\text{hex}}(\mathbf{r})$, where r is the amplitude ratio of the two lattices (Fig. 4.4). When the contribution from the hexagonal lattice beam is negligible, the localized electrons form a hexagonal superlattice and the lowest part of the positive-energy spectrum can be explained by a two-band model. As r increases, electrons are confined to a kagome superlattice [109] and the lowest part of the positive-energy spectrum can be explained by a three-band model including a flat band. Note that slight gaps are observed in both the two-band model for the hexagonal superlattice and the three-band model for the kagome superlattice. The gap in the two-band model can be explained with the Haldane model with complex phases in the next-nearest-neighbor tunneling, as shown in Fig. 5.3(a). The gap in the kagome lattice comes from the complex phase in the nearest-neighbor tunneling [81,209]. At $r = 0$, we can see that the third band is nearly flat, while it is gapped well from the other bands. This flat band can be potentially used to stabilize strongly correlated phases.

4.6 Experimental Feasibility

For numerical calculation, we have set $\mathcal{A}_0 = 0.006(ea)^{-1}$, $\omega = 0.06t$, and $w/l = 0.3$ for Fig. 5.2 and Fig. 5.3. With the typical values of $t = 3$ eV and $a = 0.142$ nm

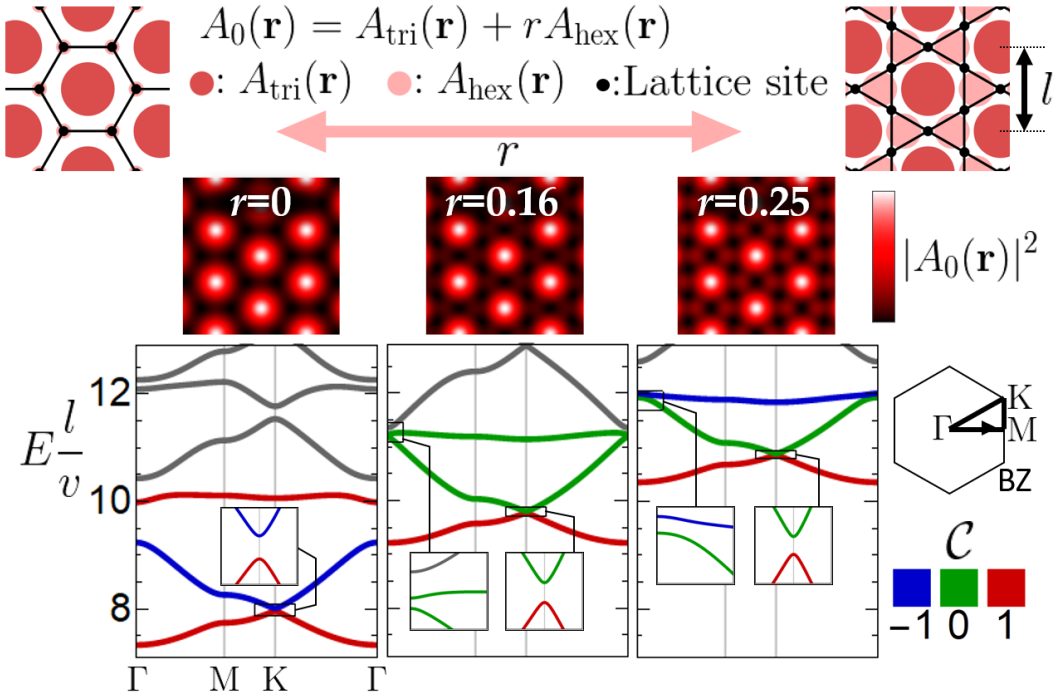

Figure 4.4: Superposition of the triangular lattice beam, $A_{\rm tri}(\mathbf{r})$, and the hexagonal lattice beam $rA_{\rm hex}(\mathbf{r})$. As we increase the ratio r, we effectively change the electron superlattice from the hexagonal lattice to the kagome lattice. Energy spectra for $\chi = 5.4$ at selected values of r are shown where the colors of low-lying bands represent the Chern numbers. By zooming in the spectrum, we can check the gaps in the two-band model and the three-band models in the lowest part of the spectrum.

for the monolayer graphene, these parameters of the laser field correspond to the field amplitude 7.6×10^6 V/m, the beam frequency 43.5 THz, and beam spot size 0.1μm (FWHM). This is similar to the beam frequency in a recent experiment [190] while the peak intensity is about 4% of the beam used in the same experiment. With these parameters, the typical size of the gap (Δ_b in Fig. 5.2) is 4 meV. Fig. 4.4 uses $\mathcal{A}_0 = 0.0015(ea)^{-1}$ and $\omega = 0.06t$ while $w/l = 0.3$ and $w/l = 0.15$ for $A_{\rm tri}(\mathbf{r})$ and $A_{\rm hex}(\mathbf{r})$, respectively. Finally, we remark that due to the injection of photons into the system, heating effects could eventually destroy the nontrivial topological behavior that is initially formed. Therefore, we only consider the prethermal regime where electron-electron and electron-phonon scatterings can be ignored [198]. In the past few years, the existence of this transient regime has been convincingly demonstrated in several pump-probe experiments [189, 190, 210].

4.7 Floquet Effective Hamiltonian in High Frequency Regime

Let us consider the Hamiltonian given by Eq. (4.1) with $\mathbf{A}(\mathbf{r},t) = A_0(\mathbf{r})e^{i\omega t}(\hat{\mathbf{x}} + i\hat{\mathbf{y}}) + \text{c.c.}$ Then we can write the time-dependent Hamiltonian as

$$\begin{aligned} H(t) &= v(\tau_z p_x \sigma_x + p_y \sigma_y) + 2ev\tau_z A_0(\mathbf{r}) \exp(i\tau_z \omega t)\sigma_+ \\ &\quad + 2ev\tau_z A_0(\mathbf{r}) \exp(-i\tau_z \omega t)\sigma_-, \end{aligned} \tag{4.7}$$

where $\sigma_\pm = (\sigma_x \pm i\sigma_y)/2$. For this Hamiltonian, the nonzero temporal Fourier components $H_q = (\omega/2\pi)\int_0^{2\pi/\omega} H(t)e^{-iq\omega\tau}d\tau$ are $H_0 = v(\tau_z p_x \sigma_x + p_y \sigma_y)$ and $H_{\pm\tau_z} = 2ev\tau_z A_0(\mathbf{r})\sigma_\pm$. Then the effective Hamiltonian in the high frequency regime is [78–

81, 186, 197, 198]

$$
\begin{aligned}
H_{\text{eff}} &= H_0 + \sum_{q>0} \frac{[H_q, H_{-q}]}{q\omega} + O(\omega^{-2}) \\
&= H_0 + \frac{H_1 H_{-1} - H_{-1} H_1}{\omega} + O(\omega^{-2}) \\
&= v(\tau_z p_x \sigma_x + p_y \sigma_y) + \tau_z \frac{4e^2 v^2}{\omega} |A_0(\mathbf{r})|^2 \sigma_z + O(\omega^{-2}). \qquad (4.8)
\end{aligned}
$$

The description in terms of Eq. (4.8) is valid as long as $H_q \ll \omega$ for every q. The condition $\omega \ll ev\mathcal{A}_0$ ensures that $H_{q=\pm 1} \ll \omega$. For $H_0 \ll \omega$, we require $v/l \ll \omega$ and the parameters we use in this chapter satisfy this condition. Yet, one may wonder if the band structure is affected by the hybridization of different Floquet sidebands [81, 191] since the driving frequency that we consider in this chapter ($\omega = 0.06t$) is much smaller than the original bandwidth of the graphene which is of the order of t. To see how much our band structure is affected by the Floquet sidebands' hybridization, we calculate the band structure presented in the left figure of Fig. 5.2(a) by diagonalizing the Floquet Hamiltonian, $H(t) - i\partial_t$. For the spatially periodic Hamiltonian $H(\mathbf{r}, t) = H(\mathbf{r} + \mathbf{L}_1, t) = H(\mathbf{r} + \mathbf{L}_2, t)$, we find the quasienergies $\epsilon_{s,\mathbf{k}}$ and the corresponding quasimode wavefunctions $\Psi_{s,\mathbf{k}}(\mathbf{r}, t) = \exp(-i\epsilon_s t)\Phi_{s,\mathbf{k}}(\mathbf{r}, t)$ through

$$
\begin{aligned}
& e^{-i\mathbf{k}\cdot\mathbf{r}} \left[H(t) - i\partial_t\right] e^{i\mathbf{k}\cdot\mathbf{r}} \Phi_{s,\mathbf{k}}(\mathbf{r}, t) = \epsilon_{s,\mathbf{k}} \Phi_{s,\mathbf{k}}(\mathbf{r}, t), \\
& \Phi_{s,\mathbf{k}}(\mathbf{r}, t) = \sum_{n,m_1,m_2} C^{(n)}_{s,m_1 m_2 \mathbf{k}} e^{i\{(m_1\mathbf{G}_1 + m_2\mathbf{G}_2 + \mathbf{k})\cdot\mathbf{r} - n\omega t\}}, \\
& \sum_{n,m_1,m_2} \left| C^{(n)}_{s,m_1 m_2 \mathbf{k}} \right|^2 = 1, \qquad (4.9)
\end{aligned}
$$

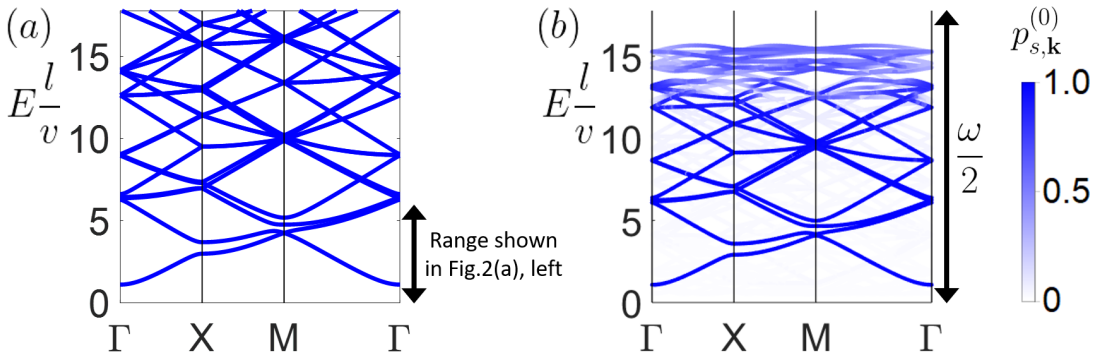

Figure 4.5: Calculated band structure of the square superlattice with $e\mathcal{A}_0 a = 0.006$, $\omega = 0.06t$, $w/l = 0.3$, and $\chi = 0.8$. (a) Calculation with Eq. (4.8). (b) Calculation with Eq. (4.9). The color of the plot represents the overlap with the zeroth Floquet sideband, $p^{(0)}_{s,\mathbf{k}}$.

where $\mathbf{G}_{i=1,2}$ are the reciprocal superlattice vectors satisfying $\mathbf{G}_i \cdot \mathbf{L}_j = 2\pi\delta_{ij}$. Here, the quasienergies are restricted to the zeroth Floquet sideband, $\epsilon_{s,\mathbf{k}} \in [-\omega/2, \omega/2]$. For the time-independent Hamiltonian $H(t) = H_0$, Eq. (4.9) becomes an eigenvalue equation for H_0 by fixing the Floquet sideband index n, and $n = 0$ corresponds to the eigenstates with energy in $[-\omega/2, \omega/2]$. Therefore, if we consider the case that oscillating terms are slowly turned on, the relevant quasimodes should have high overlaps with the zeroth Floquet sideband, which is quantified by

$$p^{(0)}_{s,\mathbf{k}} = \sum_{m_1,m_2} \left| C^{(0)}_{s,m_1 m_2 \mathbf{k}} \right|^2 . \tag{4.10}$$

For the comparison of the two descriptions given by Eq. (4.8) and Eq. (4.9), we calculate the band structure plotted in the left of Fig. 5.2(a) with these two descriptions, respectively (see Fig. 4.5). For the band structure calculated with Eq. (4.9), we represented the overlap with the zeroth Floquet sideband, $p^{(0)}_{s,\mathbf{k}}$, for each

state. In the energy much lower than $\omega/2$, the spectrum calculated with the high-frequency expansion and the quasienergies of the Floquet eigenstates with high overlaps with the zeroth Floquet sideband agree with each other. As the energy approaches $\omega/2$, the Floquet sideband hybridization due to the resonant process affects the band structure. Therefore, one can use the high-frequency expansion description in Eq. (4.8) for energies far smaller than the driving frequency.

4.8 Band Gap Scaling in Superlattice Size

We consider the eigenvalue problem of the effective Hamiltonian in Eq. (4.2),

$$\begin{pmatrix} \alpha(\mathbf{r}) & -iv(\partial_x - i\partial_y) \\ -iv(\partial_x + i\partial_y) & -\alpha(\mathbf{r}) \end{pmatrix} \begin{pmatrix} u_A \\ u_B \end{pmatrix} = E \begin{pmatrix} u_A \\ u_B \end{pmatrix}$$
$$\leftrightarrow -iv(\partial_x - i\partial_y)u_B = [E - \alpha(\mathbf{r})]u_A,\ -iv(\partial_x + i\partial_y)u_A = [E + \alpha(\mathbf{r})]u_B \quad (4.11)$$

where $\alpha(\mathbf{r}) = (4e^2v^2/\omega)|A_0(\mathbf{r})|^2$. This can lead to

$$\nabla^2 u_B + \frac{E^2 - \alpha(\mathbf{r})^2}{v^2}u_B + \frac{[(\partial_x + i\partial_y)\alpha(\mathbf{r})][(\partial_x - i\partial_y)u_B]}{E - \alpha(\mathbf{r})} = 0. \quad (4.12)$$

In the vicinity of minima of $\alpha(\mathbf{r})$, we can approximate this function as a harmonic potential with rotational symmetry. This is valid for the square lattice of the Gaussian beam with the fixed ratio $c = w/l$,

$$\alpha(\mathbf{r}) = \frac{4e^2v^2\mathcal{A}_0^2}{\omega}\left[\sum_{n_1,n_2} e^{-\{(x-n_1l)^2+(y-n_2l)^2\}/(2c^2l^2)}\right]^2. \quad (4.13)$$

For this case, one can show that

$$\left.\frac{\partial\alpha}{\partial x}\right|_{\mathbf{r}=(l/2,l/2)} = \left.\frac{\partial\alpha}{\partial y}\right|_{(l/2,l/2)} = \left.\frac{\partial^2\alpha}{\partial x\partial y}\right|_{(l/2,l/2)} = 0,$$
$$\alpha_0 \equiv \alpha|_{(l/2,l/2)} > 0, \alpha_1 \equiv \left.\frac{l^2}{2}\partial_x^2\alpha\right|_{(l/2,l/2)} = \left.\frac{l^2}{2}\partial_y^2\alpha\right|_{(l/2,l/2)} > 0,$$
$$\frac{\partial\alpha_0}{\partial l} = \frac{\partial\alpha_1}{\partial l} = 0. \tag{4.14}$$

Then we can write $\alpha(\mathbf{r}) = \alpha_0 + \alpha_1(r/l)^2$, where r is the distance from the minima of $\alpha(\mathbf{r})$. Now we can use polar coordinates (r,ϕ), with $\partial_x \pm i\partial_y = a^{-1}e^{\pm i\phi}(\partial_r \pm ir^{-1}\partial_\phi)$. Due to the rotational symmetry, we can impose $u_B(\mathbf{r}) = \beta(r)e^{im\phi}$. Then,

$$\frac{1}{r}\partial_r\left(r\partial_r\beta\right) - \frac{m^2}{r^2}\beta + \frac{1}{v^2}\left[E^2 - \alpha_0^2 - 2\alpha_0\alpha_1\left(\frac{r}{l}\right)^2 - \alpha_1^2\left(\frac{r}{l}\right)^4\right]\beta$$
$$+\frac{2\alpha_1(r\partial_r + m)\beta}{(E-\alpha_0)l^2 - \alpha_1 r^2} = 0. \tag{4.15}$$

Note that $l \to \infty$ limit corresponds to $\nabla^2 u_A + v^{-2}(E^2 - \alpha_0^2) = 0$. The positive spectrum in this limit is $[\alpha_0, \infty)$ with no gap in between. To study the behavior of the positive spectrum for large l, we may define $\delta E = E - \alpha_0$. For the low-lying spectrum, we can only consider the limit where $\delta E \ll \alpha_0$. Then we can simplify Eq. (4.15) into

$$\frac{1}{r}\partial_r\left(r\partial_r\beta\right) - \frac{m^2}{r^2}\beta + \frac{1}{v^2}\left[2\alpha_0\delta E - 2\alpha_0\alpha_1\left(\frac{r}{l}\right)^2\right]\beta + \frac{2(r\partial_r + m)\beta}{l^2\delta E/\alpha_1} = 0 \tag{4.16}$$

up to the correction terms of the order of $O(\delta E^2), O(\eta^{-4})$. Now the rescaling $r = (vl)^{1/2}(\alpha_0\alpha_1)^{-1/4}\xi$ and $\delta E = (\alpha_1/\alpha_0)^{1/2}(v/l)(\delta\epsilon)$ gives

$$\frac{1}{\xi}\partial_\xi\left(\xi\partial_\xi\beta\right) - \frac{m^2}{\xi^2}\beta + 2\left(\delta\epsilon - \xi^2\right)\beta + \frac{2(\xi\partial_\xi + m)\beta}{\delta\epsilon} = 0 \tag{4.17}$$

and this equation is independent of l. Then the spectrum of $\delta\epsilon$ is independent of l, so that δE should scale as l^{-1}. This means that $\Delta_b - 2\alpha_0$ and Δ_t should be proportional to l^{-1}. This explains the inverse proportionality of band gaps in $\chi = (ve^2\mathcal{A}_0^2/\omega)l$ shown in Fig. 5.2(b).

4.9 Tight-binding Model for Hexagonal Lattice under a Uniform Strain

Let us consider the effective lattice model for the sheared lattice in the vicinity of angle $\theta = \tan^{-1} 0.5$. By considering the terms up to the next-nearest neighbors, we can build a tight-binding model similar to the Haldane model,

$$\begin{aligned} H_{\mathrm{SH}} \quad &= \sum_{m,n}\left(-t_1 c_{m,n}^{(B)\dagger} - t_2 c_{m-1,n}^{(B)\dagger} - t_3 c_{m,n-1}^{(B)\dagger}\right) c_{m,n}^{(A)} \\ &+ \left(s_1 c_{m+1,n}^{(A)\dagger} + s_2 c_{m,n-1}^{(A)\dagger} + s_3 c_{m-1,n+1}^{(A)\dagger}\right) c_{m,n}^{(A)} \\ &+ \left(s_1 c_{m-1,n}^{(B)\dagger} + s_2 c_{m,n+1}^{(B)\dagger} + s_3 c_{m+1,n-1}^{(B)\dagger}\right) c_{m,n}^{(B)} + \mathrm{H.c.}. \end{aligned} \tag{4.18}$$

Here, $c_{m,n}^{(A/B)\dagger}$ creates an electron in the sublattice A or B at the unit cell (m, n) and $t_{i=1,2,3}$ ($s_{i=1,2,3}$) is the nearest- (next-nearest)-neighbor tunneling amplitude, as shown in Fig. 4.6. This model can be thought of as a hexagonal lattice under a

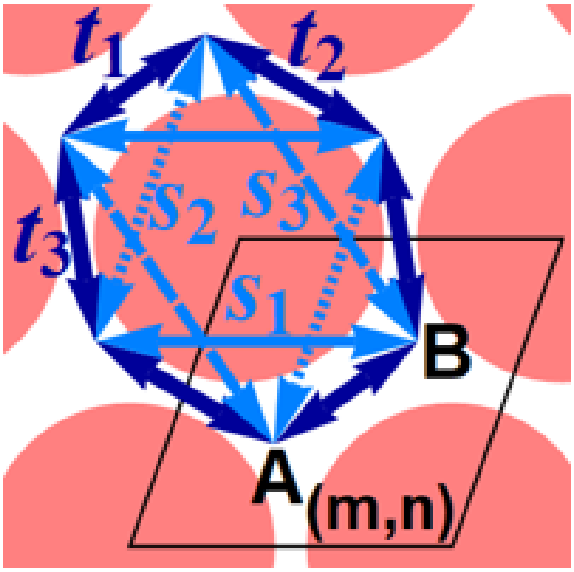

Figure 4.6: Tight-binding model for the hexagonal lattice under a uniform strain, in the vicinity of angle $\theta = \tan^{-1} 0.5$ in the sheared lattice.

uniform strain. By considering the inversion symmetry of the corresponding pairs of lattice sites, we can find that $\mathrm{Im}(t_1) = \mathrm{Im}(t_2) = \mathrm{Im}(t_3) = 0$. Now we can write the Bloch Hamiltonian of this tight-binding model as

$$
\begin{aligned}
\mathcal{H}(\mathbf{k}) &= V(\mathbf{k}) + h_x(\mathbf{k})\sigma_x + h_y(\mathbf{k})\sigma_y + h_z(\mathbf{k})\sigma_z, \\
V(\mathbf{k}) &= 2\mathrm{Re}\left[s_1 \cos(\mathbf{k}\cdot(\mathbf{L}_2 - \mathbf{L}_1)) + s_2 \cos(\mathbf{k}\cdot\mathbf{L}_2) + s_3 \cos(\mathbf{k}\cdot\mathbf{L}_1)\right], \\
h_x(\mathbf{k}) &= -t_1 \cos\left(\mathbf{k}\cdot\frac{\mathbf{L}_1+\mathbf{L}_2}{3}\right) - t_2 \cos\left(\mathbf{k}\cdot\frac{\mathbf{L}_2-2\mathbf{L}_1}{3}\right) - t_3 \cos\left(\mathbf{k}\cdot\frac{\mathbf{L}_1-2\mathbf{L}_2}{3}\right), \\
h_y(\mathbf{k}) &= -t_1 \sin\left(\mathbf{k}\cdot\frac{\mathbf{L}_1+\mathbf{L}_2}{3}\right) - t_2 \sin\left(\mathbf{k}\cdot\frac{\mathbf{L}_2-2\mathbf{L}_1}{3}\right) - t_3 \sin\left(\mathbf{k}\cdot\frac{\mathbf{L}_1-2\mathbf{L}_2}{3}\right), \\
h_z(\mathbf{k}) &= 2\mathrm{Im}\left[s_1 \sin(\mathbf{k}\cdot(\mathbf{L}_2 - \mathbf{L}_1)) + s_2 \sin(\mathbf{k}\cdot\mathbf{L}_2) + s_3 \sin(\mathbf{k}\cdot\mathbf{L}_1)\right], \qquad (4.19)
\end{aligned}
$$

where the $\sigma_z = \pm 1$ corresponds to the sublattice A or B. In the absence of the next-nearest-neighbor tunnelings, $V = h_z = 0$ and the location of the Dirac points is determined by $h_x(\mathbf{k}) = h_y(\mathbf{k}) = 0$. If this equation has two solutions, we denote

those solutions as $\mathbf{k} = \pm\mathbf{K}_D$. In Eq. (4.19), we can see that the second-neighbor tunnelings solely determine the σ_z component of the Bloch Hamiltonian and do not affect the σ_x and σ_y components. By turning on the second-neighbor tunnelings, we effectively turn on the mass term around each of the Dirac points $\pm\mathbf{K}_D$. Since $h_z(-\mathbf{K}_D) = -h_z(\mathbf{K}_D)$, the sign of the effective mass term is opposite at the two different Dirac points. Then, each Dirac point equally contributes 1/2 to the Chern number, just as in the Haldane model. Therefore, if the two Dirac points exist in the absence of the next-nearest-neighbor tunneling, the lowest positive band has nonzero Chern number when the next-nearest-neighbor tunneling is turned on. Regarding this condition, the equation $h_x(\mathbf{k}) = h_y(\mathbf{k}) = 0$ has two solutions as long as $|t_i - t_j| < |t_k|$ for every $i \neq j \neq k \neq i$. Since the tunneling strength decreases exponentially in the intersite distance, t_1, t_2, and t_3 become very different as the superlattice size gets larger. Then there is no Dirac point after some value of χ, as shown in the square-lattice case. Yet, at angle $\theta = \tan^{-1} 0.5$, $t_1 = t_2$, so that $|t_i - t_j| < |t_k|$ is satisfied as long as $t_3 \neq 0$, and therefore $\mathcal{C}_1$ can remain nonzero at this angle.

4.10 Gauge-Independent Calculation of Orbital Magnetization

We want to numerically calculate the orbital magnetization of the mth band expressed in Eq. (4.6),

$$\begin{aligned} M_{\text{orb}} &= \text{Im} \int \frac{d^2\mathbf{k}}{(2\pi)^2} e \frac{\partial \langle u_{m,\mathbf{k}}|}{\partial_{k_x}} (H_\mathbf{k} + E_{m,\mathbf{k}}) \frac{\partial |u_{m,\mathbf{k}}\rangle}{\partial_{k_y}} \\ &= \text{Im} \int \frac{d^2\mathbf{k}}{(2\pi)^2} e \frac{\partial \langle u_{m,\mathbf{k}}|}{\partial_{k_x}} H_\mathbf{k} \frac{\partial |u_{m,\mathbf{k}}\rangle}{\partial_{k_y}} + \frac{1}{2} \int \frac{d^2\mathbf{k}}{(2\pi)^2} e E_{m,\mathbf{k}} \mathcal{A}_{m,\mathbf{k}}, \end{aligned} \tag{4.20}$$

where $\mathcal{A}_{m,\mathbf{k}} = 2\mathrm{Im}\left(\partial_{k_x}\langle u_{m,\mathbf{k}_j}|\right)\partial_{k_y}|u_{m,\mathbf{k}_j}\rangle$ is the Berry curvature. To numerically calculate it, we first need to discretize the Brillouin zone and calculate the Bloch state $|\psi_{m,\mathbf{k}_j}\rangle$. Although the orbital magnetization is gauge independent, we need local gauge fixing to make $|\psi_{m,\mathbf{k}}\rangle$ differentiable. While this local gauge fixing works well for smooth $\mathcal{A}_{m,\mathbf{k}}$, it can work badly for the system in the vicinity of the topological phase transition. To avoid this subtlety, let us find a way to calculate this quantity in a gauge-independent way. For Berry curvature $\mathcal{A}_{m,\mathbf{k}}$, a method for gauge-independent calculation is known [204]. Similar to this method, we can calculate the first integral of Eq. (4.20). For this, let us consider a square patch whose four corners are $\mathbf{q}_{l,j} \equiv \mathbf{k}_l + (\delta k/2)(s_j\hat{\mathbf{x}} + w_j\hat{\mathbf{y}})$, where $(s_1, w_1) = (-1, -1)$,

$(s_2, w_2) = (1, -1)$, $(s_3, w_3) = (1, 1)$, and $(s_4, w_4) = (-1, 1)$. Now

$$
\begin{aligned}
&|u_{m,\mathbf{q}_{l,j}}\rangle = |u_{m,\mathbf{k}_l}\rangle + \frac{\delta k}{2}\left(s_j \partial_{k_x} |u_{m,\mathbf{k}_l}\rangle + w_j \partial_{k_y} |u_{m,\mathbf{k}_l}\rangle\right) \\
&\qquad + \frac{\delta k^2}{8}\left(\partial_{k_x}^2 |u_{m,\mathbf{k}_l}\rangle + 2 s_j w_j \partial_{k_x}\partial_{k_y} |u_{m,\mathbf{k}_l}\rangle + \partial_{k_y}^2 |u_{m,\mathbf{k}_l}\rangle\right) + O(\delta k^3), \\
&E_{m,\mathbf{k}_l}^{-4} \prod_{j=1}^{4} \langle u_{m,\mathbf{q}_{l,j}} | H_{\mathbf{k}_l} | u_{m,\mathbf{q}_{l,(j \bmod 4)+1}} \rangle \\
&= 1 + \delta k \mathrm{Re} \sum_{j=1}^{4} \left(s_j \langle u_{m,\mathbf{k}_l} | \partial_{k_x} | u_{m,\mathbf{k}_l}\rangle + w_j \langle u_{m,\mathbf{k}_l} | \partial_{k_y} | u_{m,\mathbf{k}_l}\rangle\right) \\
&\quad + \delta k^2 \mathrm{Re} \langle u_{m,\mathbf{k}_l} | \nabla_{\mathbf{k}}^2 | u_{m,\mathbf{k}_l}\rangle + \delta k^2 \mathrm{Re} \sum_j \frac{s_j w_j}{2} \langle u_{m,\mathbf{k}_l} | \partial_{k_x}\partial_{k_y} | u_{m,\mathbf{k}_l}\rangle \\
&\quad + \frac{\delta k^2}{4 E_{m,\mathbf{k}_l}} \sum_{j=1}^{4} \Big[s_j s_{(j \bmod 4)+1} \left(\partial_{k_x} \langle u_{m,\mathbf{k}_l}|\right) H_{\mathbf{k}_l} \partial_{k_x} |u_{m,\mathbf{k}_l}\rangle \\
&\qquad\qquad + s_j w_{(j \bmod 4)+1} \left(\partial_{k_x} \langle u_{m,\mathbf{k}_l}|\right) H_{\mathbf{k}_l} \partial_{k_y} |u_{m,\mathbf{k}_l}\rangle \\
&\qquad\qquad + w_j s_{(j \bmod 4)+1} \left(\partial_{k_y} \langle u_{m,\mathbf{k}_l}|\right) H_{\mathbf{k}_l} \partial_{k_x} |u_{m,\mathbf{k}_l}\rangle \\
&\qquad\qquad + w_j w_{(j \bmod 4)+1} \left(\partial_{k_y} \langle u_{m,\mathbf{k}_l}|\right) H_{\mathbf{k}_l} \partial_{k_y} |u_{m,\mathbf{k}_l}\rangle \Big] + O(\delta k^3) \\
&= 1 + 2\delta k^2 \mathrm{Re} \langle u_{m,\mathbf{k}_l} | \nabla_{\mathbf{k}}^2 | u_{m,\mathbf{k}_l}\rangle \\
&\quad + i \frac{2\delta k^2}{E_{m,\mathbf{k}_l}} \mathrm{Im} \left(\partial_{k_x} \langle u_{m,\mathbf{k}_l}|\right) H_{\mathbf{k}_l} \partial_{k_y} |u_{m,\mathbf{k}_l}\rangle + O(\delta k^3),
\end{aligned}
\tag{4.21}
$$

and therefore

$$
\begin{aligned}
&\frac{e E_{m,\mathbf{k}_l}}{8\pi^2} \mathrm{Arg}\left(\prod_{j=1}^{4} \langle u_{m,\mathbf{q}_{l,j}} | H_{\mathbf{k}_l} | u_{m,\mathbf{q}_{l,(j \bmod 4)+1}} \rangle\right) \\
&= \frac{e}{4\pi^2} \mathrm{Im} \left(\partial_{k_x} \langle u_{m,\mathbf{k}_l}|\right) H_{\mathbf{k}_l} \partial_{k_y} |u_{m,\mathbf{k}_l}\rangle \, \delta k^2 + O(\delta k^3),
\end{aligned}
\tag{4.22}
$$

and this corresponds to the first integral of Eq. (4.20) over the square patch that we considered. One can easily check that this expression is invariant under any gauge transformation, $|u_{m,\mathbf{k}}\rangle \to \exp[i\lambda(\mathbf{k})]\,|u_{m,\mathbf{k}}\rangle$, $\forall \lambda(\mathbf{k})$, and does not require any local

gauge fixing.

4.11 Outlook

By considering Coulomb interaction in our nearly flat and topologically non-trivial bands, one could potentially induce strongly correlated phases such as fractional Chern insulators [168, 211–213], superconductors [172, 178, 182–184, 214, 215], or magnetic phases [174, 179–181]. Moreover, by irradiating with frequencies comparable to the bare tunneling strength, instead of the high-frequency regime considered here, higher-order terms become relevant [81], and therefore, one can induce a wider class of structures. While we focus on the Dirac semimetal system in this chapter, our scheme can also be applied to other 2D materials such as semiconductors [216]. Our approach can be combined with other methods, such as surface acoustic waves in a solid-state platform [217], for trapping, cooling, and controlling charged particles, and for simulation of quantum many-body systems. Finally, these ideas could be used to engineer a new class of dielectric materials for potential applications in optical devices [218].

Chapter 5: Floquet Vortex States Induced by Light Carrying the Orbital Angular Momentum

5.1 Introduction

Quantum vortices and localized quantum states associated with them have long a subject of active interest in diverse areas of physics [219–224]. To create and observe such quantum vortex states, numerous efforts have been made in diverse systems such as Bose-Einstein condensates [225–230], superconductors [231, 232], and magnetic materials [233–235]. While the quantum vortex states themselves exhibit many exotic quantum and classical many-body phenomena [236–241], their stability as topological defects makes them a promising quantum platform for applications such as quantum information processing [5, 242, 243].

Recently, Floquet systems have become popular as a useful way to engineer exotic quantum states [15, 79, 186, 188, 190, 197, 200, 201, 244–246]. Moreover, there have been many recent advancements in the spatial control of optical beams in atomic systems [94, 98, 100, 119]. These techniques have the potential to be applied to electronic systems and can provide a wide range of tunability in quantum state engineering.

In this chapter, we present a scheme to create Flouqet quantum vortex states by shining a light field carrying orbital angular momentum (OAM) on a two-dimensional (2D) semiconductor, as illustrated in Fig.5.1. In small detuning and the weak field limit, we show that electronic Floquet vortex states are localized around the optical vortices with localization length bounded by the shape and intensity of the optical field. We also show that the number of vortex state branches is directly given by the vorticity of the light, which quantifies the OAM carried by each photon. Such close relation with OAM of light distinguish these vortex states from the edge states of the uniform Floquet Chern insulator [188] or the vortex states introduced in Ref. [200, 201]. While many characteristics of these Floquet vortex states carry close analogy with superconducting systems, we show that the Floquet vortex states in the current system benefit from a very broad range of tunability. For example, the freedom to choose the size of the optical vortex can be used as a knob to control the non-linearity of the vortex state spectrum. To demonstrate how such tunability can be exploited for quantum state engineering, we construct a scheme of quantum information processing based on optically manipulating Floquet vortex states, with simple single-qubit and two-qubit operations.

5.2 Model

We consider $H_0 = (vk_x, vk_y, M) \cdot \sigma$ as our model for a spinless 2D semiconductor [32, 247]. For brevity, we have set $\hbar = 1$. Here, $\sigma = (\sigma_x, \sigma_y, \sigma_z)$ are Pauli matrices. M is a half of the band gap and v is a parameter determining the cur-

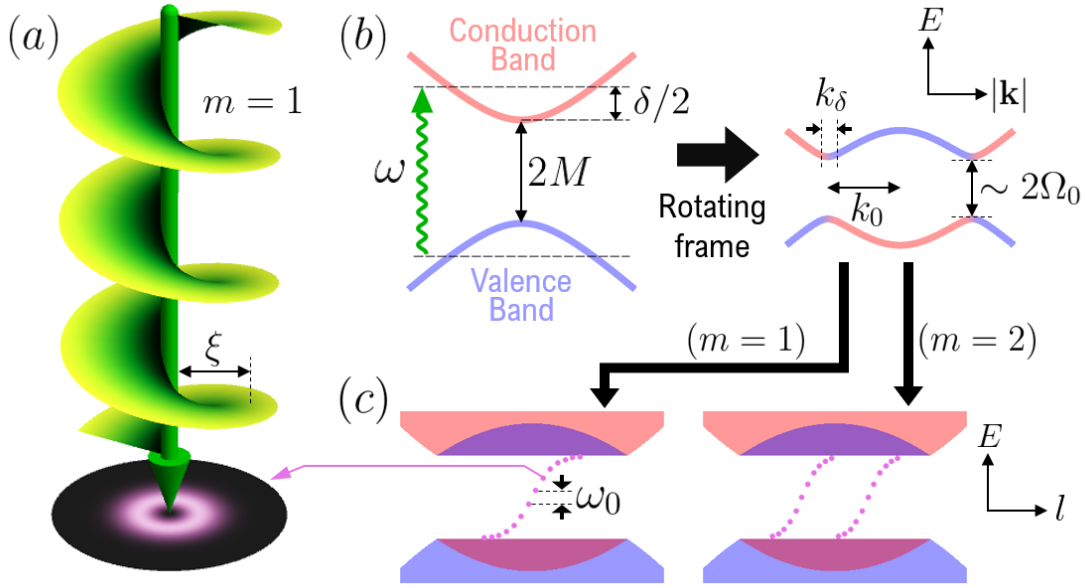

Figure 5.1: (a) A 2D semiconductor illuminated by a laser light carrying OAM. The applied light field has the optical vortex structure of size ξ. The figure illustrates the case of vorticity $m = 1$. (b) The laser field has frequency ω, and couples the conduction and the valence bands of the semiconductor with the gap $2M$. The detuning is $\delta = \omega - 2M$. In the rotating frame, the hybridization gap of about $2\Omega_0$ develops around the resonance ring whose radius and thickness are k_0 and k_δ, respectively. (c) For the light field with non-zero vorticity m, $|m|$ branches of Floquet vortex states develop in the middle of the hybridization gap. Around the zero energy, each branch has linear dispersion with energy separation ω_0 between nearby states in the branch. Note that the energy spectrum is illustrated with respect to the electronic pseudo-OAM, l.

vature of the band dispersion $\pm\sqrt{M^2 + v^2(k_x^2 + k_y^2)}$, where the positive (negative) energy states correspond to the conduction (valence) band. We vertically shine a linearly-polarized laser field with a non-zero orbital angular momentum (OAM), $\mathcal{A}(\mathbf{r}, t) = A(\mathbf{r})e^{i\omega t}\hat{\mathbf{x}} + \text{c.c.}$ on a semiconductor, as illustrated in Fig. 5.1 where ω is the frequency of the laser field. The OAM of the laser field is represented in the azimuthal phase factor of $A(\mathbf{r}) = A_0(r)e^{im\phi}$, where $r = \sqrt{x^2 + y^2}$ and $\phi = \arctan(y/x)$. The integer m here is the vorticity of the field, and we refer the vortex structure with non-zero vorticity in the light field as an optical vortex. Due to this vortex

structure, $A_0(r)$ should vanish at $r = 0$. We set the size of optical vortex to ξ, which means that $A_0(r)$ smoothly saturates to $A_{\max}$ at $r \geq \xi$. With the minimal coupling $\mathbf{k} = (k_x, k_y) \to \mathbf{k} + e\mathcal{A}(\mathbf{r}, t)$, we obtain the time-periodic Hamiltonian

$$H(t) = H_0 + ev\mathcal{A}(\mathbf{r}, t) \cdot \sigma. \tag{5.1}$$

When $\omega > 2M$, the frequency detuning $\delta = \omega - 2M$ becomes positive and the conduction and valence bands become resonant at the resonance ring of momentum, $|\mathbf{k}| = k_0 = v^{-1}\sqrt{\omega^2/4 - M^2}$. From Eq. (5.1), the applied laser field generates position-dependent Rabi frequency $\Omega(r) = evA_0(r)$ and hybridizes the conduction and valence bands while opening an energy gap about $2\Omega_0$ around the resonance ring, where $\Omega_0 = \lim_{r\to\infty} \Omega(r)$. To describe these hybridized bands, we consider the transformation into the rotating frame, $U(t) = P_c e^{-i\omega t/2} + P_v e^{i\omega t/2}$, where P_c (P_v) is the projection operator into the conduction (valence) band. In the weak field limit $\Omega_0 \ll \sqrt{\omega\delta}$, we can drop the fast oscillating terms from the rotated Hamiltonian $-iU^\dagger(t)\partial_t U(t) + U^\dagger(t)H(t)U(t)$ and obtain the effective Hamiltonian under the rotating wave approximation (RWA). Furthermore, we consider the small detuning regime $\delta \ll \omega$. In this regime, we can write $\delta \simeq v^2 k_0^2/M$ and $vk_0 \ll M$. Then, for the small momenta $|\mathbf{k}| = O(k_0)$ (see Sec. 5.5),

$$H_{\text{RWA}} = \frac{\delta}{2}\left(\frac{\mathbf{k}^2}{k_0^2} - 1\right)\sigma_z + \left[\Omega(r)e^{-im\phi}\sigma_+ + \text{H.c.}\right], \tag{5.2}$$

where $\sigma_\pm = (\sigma_x \pm i\sigma_y)/2$.

5.3 Floquet Vortex States

Because of the breaking of the translational symmetry by the optically-induced vortex, it is possible to have electronics states with energies inside the spectral gap that are localized in the vicinity of the vortex. From Eq. (5.2), we can estimate the spatial extent of such states. First, one can readily observe that the diagonal components are dominant over off-diagonal elements for most of **k**s except the vicinity of the resonance ring. This means that the hybridization mostly occurs at the momenta in the narrow region near the resonance ring, and the thickness of this region can be estimated by finding the range of $|\mathbf{k}|$ that makes the off-diagonal elements of Eq. (5.2) comparable to or larger than the diagonal elements. We find that the hybridization of the two bands occurs at $|\mathbf{k}| - k_0 = O(k_\delta)$ where $k_\delta \equiv k_0\Omega_0/\delta$, that characterizes the momentum range over which the Rabi frequency and dispersion of Eq.5.2 are comparable around the resonant momentum ring. If any intragap state develops within this hybridization gap, such a state should be a superposition of the Bloch states within this momentum region. Therefore k_δ^{-1} serves as a lower bound for the spatial size of such intragap state. If a localized intragap state develops around the optical vortex, this state cannot extend to the region where $A_0(r)$ saturates to $A_{\max}$ since the field is nearly uniform and therefore the system remains gapped. Therefore such a localized intragap state has an upper bound $O\left(k_\delta^{-1} + \xi\right)$ for its size.

By using the semiclassical argument introduced in Ref. [248], one can show that $|m|$ branches of intragap states develop around the optical vortex with vorticity

m (see Sec. 5.6). We call these states Floquet vortex states, and we can obtain a fully quantum-mechanical description of the dispersion and wavefunction of these states by applying mathematical methods used for superconducting vortices [222,249–251]. To do so, we note that while the effective Hamiltonian in Eq. (5.2) does not commute with the electronic OAM, $\hat{L} = -i\partial_\phi$, it does commute with the electronic pseudo-OAM, $\hat{l} = -i\partial_\phi + (m/2)\sigma_z$. Then the eigenstates of this effective Hamiltonian can be written in the form of vortex states,

$$\psi_{n,l}(\mathbf{r}) = \left(e^{i(l-m/2)\phi}u_{n,l,+}(r), e^{i(l+m/2)\phi}u_{n,l,-}(r)\right)^T. \tag{5.3}$$

Here, the branch index $n = 1, \cdots, m$ represents different branches of Floquet vortex states. One can also show that this system satisfies the particle-hole symmetry which requires $\psi_{n,-l}(\mathbf{r}) = i\sigma_y\psi^*_{|m|+1-n,l}(\mathbf{r})$ and $E_{n,-l} = -E_{|m|+1-n,l}$, where $E_{n,l}$ is the corresponding eigenenergy for $\psi_{n,l}(\mathbf{r})$. In the large optical vortex regime $k_\delta^{-1} \ll \xi$, the low-energy spectrum of these Floquet vortex states are given by [251]

$$\begin{aligned} E_{n,l} &= ml\omega_0 + [n - (|m|+1)/2]\tilde{\omega}_0, \text{ where} \\ \omega_0 &= \frac{\delta\int_0^\infty \frac{\Omega(r)}{r}e^{-(2k_0/\delta)\int_0^r \Omega(r')dr'}dr}{k_0\int_0^\infty e^{-(2k_0/\delta)\int_0^r \Omega(r')dr'}dr}, \quad \tilde{\omega}_0 = \frac{\delta(\pi/2)}{k_0\int_0^\infty e^{-(2k_0/\delta)\int_0^r \Omega(r')dr'}dr}. \end{aligned} \tag{5.4}$$

Here, the energy separation between nearby states and branches, ω_0 and $\tilde{\omega}_0$, respectively, are solely determined by the bulk properties and the details of the radial beam profile $A_0(r)$. These parameters are independent of the system size and therefore the energy separation between states remains in the thermodynamic limit.

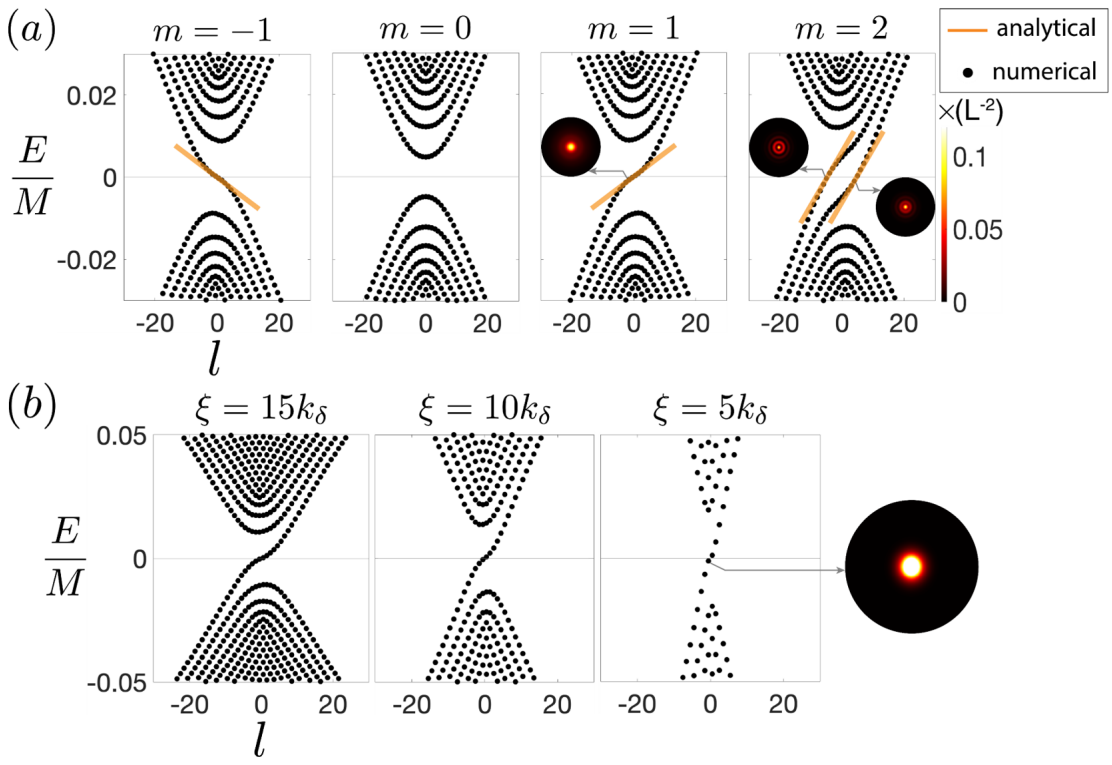

Figure 5.2: (a) Numerically calculated energy spectra in terms of pseudo-OAM l. We use $\omega = 2.05M$, $A_{\max} = 0.09M(ev)^{-1}$, and $A_0(r) = A_{\max}\left[1 - \exp\{-r^2/(2\xi^2)\}\right]$, $\xi = 20k_\delta$, and suppose a disk sample of radius 25ξ. The numerical spectra agree with the analytically expected dispersion in Eq. (5.4) including the number of intragap state branches and the slope of the linear dispersion for small $|E_l|$ and l. Electronic density profiles of selected states are presented in the insets. (b) Dispersions for $m = 1$ with identical parameters with (a) except the optical vortex size ξ and the disk size $500k_\delta$. As ξ reduces, the linear region of the spectrum shrinks while the energy separation between the nearby states increases.

This analytic expression of the dispersion is valid for the low-energy and the low-l regime, $|E_{n,l}| \ll \Omega_0$ and $|l| \ll \sqrt{\delta/\Omega_0}$. Fig. 5.2(a) presents how this analytically found dispersion agrees with the numerical dispersion obtained by diagonalizing Eq. (5.2) (see Sec. 5.9). As shown in the figure, the number of intragap state branches is given by $|m|$. The analytic dispersion and the numerical dispersion agree for the low-energy and low-l regime, and deviate from each other as the energy or l moves away from zero. Nevertheless, we can still use Eq. (5.4) to get a rough estimate of

the pseudo-OAM differences between different intragap state branches, in the large optical vortex regime (see Sec. 5.7). Assuming the entire intragap state branches are linearly dispersing, the different branches at the same energy would have the pseudo-OAM momentum difference of $\tilde{\omega}_0/\omega_0 = O\left(k_0 k_\delta^{-1}\sqrt{k_\delta \xi}\right)$. This large difference in the angular momentum prevents the vortex modes from different branches to hybridize each other. With the same assumption, the number of states in a single branch can be also estimated as $2\Omega_0/\omega_0 = O(k_0\xi)$.

Note that these Floquet vortex states around the optical vortex are distinguished from the edge states of topological Floquet Chern insulators [188] or the vortex states introduced in Ref. [200, 201]. For the edge state of the Floquet Chern insulator to develop, the bulk part of the system should have a non-zero Chern number, while the Floquet vortex states we are discussing appear regardless of the Chern number of the system. This point becomes clear by investigating the system under irradiation of a circularly-polarized light beam which also carries a non-zero OAM (see Sec. 5.8). While the bulk part of such system becomes a Floquet Chern insulator as explained in Ref. [188], there are still $|m|$ branches of Floquet vortex states in the middle of the hybridization gap. The Floquet vortex states in our system also differ from the vortex states in Ref. [200, 201] where the vortex structure does not couple with the electronic kinetic terms and has no trivial way to realize in experiments.

While many properties of the Floquet vortex states can be analyzed with the similar techniques used for superconducting vortex states, our Floquet vortex states have wider tunability due to the freedom to control the size of optical vortices. For

superconducting vortex states, the size of vortices is tied to $O\left(k_\delta^{-1}\right)$ since the BdG equation should be satisfied in a self-consistent way. However, Eq. (5.2) does not have such constraints and we have the freedom to choose the size of the optical vortex. To illustrate the consequence of this freedom, we display the numerical dispersion for different optical vortex sizes in Fig. 5.2(b). As shown in the figure, as the optical vortex size ξ gets smaller, the linear region of the spectrum shrinks and therefore the non-linearity of the spectrum is enhanced. This adjustable non-linear dispersion of Floquet vortex states invites the possibility of using them as a platform for quantum state engineering.

5.4 Quantum Information Processing with Floquet Vortex States

To illustrate the potential utility of the Floquet vortex states as a platform for quantum state engineering, we show how one and two-qubit operations can be performed in this system. As we have seen in the previous section, we can increase the energy level spacing and the spectral non-linearity by reducing the size of the optical vortex. It is this enhanced non-linearity that allows to create qubits out of the Floquet vortex states and manipulate them (Fig. 5.3).

Specifically, we consider two Floquet vortex states with pseudo-angular momentum l_0 and l_0+1 of an intragap branch with index n. That is, $\langle \mathbf{r}|0\rangle \equiv \psi_{n,l_0}(\mathbf{r})$ and $\langle \mathbf{r}|1\rangle \equiv \psi_{n,l_0+1}(\mathbf{r})$. (While here we choose the vortex states from the same intragap branch, alternatively vortex states from different branches can be also used.) To manipulate this qubit, we may apply an extra linearly-polarized field to create

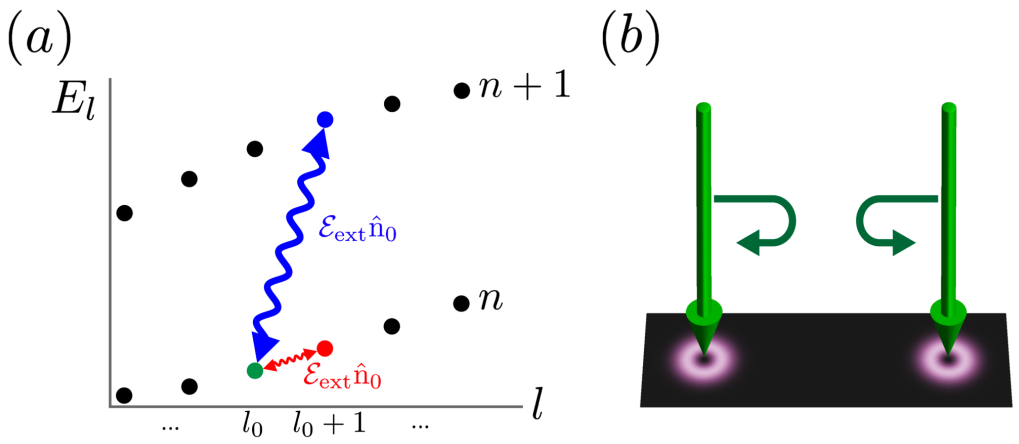

Figure 5.3: (a) The non-linearity of the dispersion allows one to encode different Floquet vortex states as qubits. For example, the vortex states with pseudo-OAM l_0 and l_0+1 from the vortex state branch with index n (red arrow) or the branches with indices n and $n+1$ can be used to encode a qubit (blue arrow). Arbitrary single-qubit rotation can be performed by shining an extra linearly polarized light. While the polarization $\hat{\mathbf{n}}_\mathbf{0}$ determines the rotation axis, the beam amplitude $\mathcal{E}_{\rm ext}$ and the irradiation time determines the rotation angle. (b) Two-qubit gates can be performed by bringing two vortices close to each other and then separating them back.

an oscillating potential

$$V_{\rm ext}(t) = e\mathcal{E}_{\rm ext}\hat{\mathbf{n}}_\mathbf{0}\cdot\mathbf{r}\cos(\Omega_{\rm ext}t), \tag{5.5}$$

where $\mathcal{E}_{\rm ext}$ is the amplitude of the applied electric field and $\hat{\mathbf{n}}_\mathbf{0} = \cos\phi_0\hat{\mathbf{x}} + \sin\phi_0\hat{\mathbf{y}}$ is the polarization of the field. Then, in the rotating frame with frequency $\Omega_{\rm ext}$, the

effective Hamiltonian for this qubit space becomes

$$
\begin{aligned}
H_{\text{1-qubit}} &= \left(E_{l_0} + \frac{\Omega_{\text{ext}}}{2}\right)|0\rangle\langle 0| + \left(E_{l_0+1} - \frac{\Omega_{\text{ext}}}{2}\right)|1\rangle\langle 1| \\
&\quad + \left[e\mathcal{E}_{\text{ext}}\langle 1|r\cos(\phi-\phi_0)|0\rangle\,|1\rangle\langle 0| + \text{H.c.}\right], \\
\langle 1|r\cos(\phi-\phi_0)|0\rangle &= \int d^2\mathbf{r}\,\psi^\dagger_{n,l_0+1}(\mathbf{r})r\cos(\phi-\phi_0)\psi_{n,l_0}(\mathbf{r}) \\
&= \pi e^{i\phi_0}\sum_{s=\pm}\int_0^\infty u^*_{n,l_0+1,s}(r)u_{n,l_0,s}(r)r^2dr. \qquad (5.6)
\end{aligned}
$$

By setting $\Omega_{\text{ext}} = E_{n,l_0+1} - E_{n,l_0}$, we can effectively tune $H_{\text{1-qubit}}$ to be a superposition of σ_x and σ_y with an arbitrary ratio between them. Then this extra field implements an arbitrary single-qubit rotation where the rotation angle is tuned by the field amplitude $\mathcal{E}_{\text{ext}}$ and the irradiation time, while the rotational axis is set by the polarization $\hat{\mathbf{n}}_\mathbf{0}$. Note that this qubit is isolated from other vortex states because the field with frequency matched to the energy difference $E_{n,l_0+1} - E_{n,l_0}$ cannot couple to other modes due to the non-linear dispersion of the vortex states.

For two-qubit operations, we can move two vortices close to one another. This will lead to a hybridization, J, between the modes with the same quantum numbers on the two vortices. Yet, single-electron hopping from one vortex to another may be energetically unfavorable due to the on-site interaction energy U. This will generate an effective superexchange interaction $\sim J^2/U$, with the corresponding two-qubit Hamiltonian,

$$
H_{\text{2-qubit}} = -\frac{J^2}{U}\left[|01\rangle\langle 01| + |10\rangle\langle 10| + (|10\rangle\langle 01| + \text{H.c.})\right], \qquad (5.7)
$$

where $|s_1 s_2\rangle = |s_1\rangle \otimes |s_2\rangle$ $(s_{1,2} = 0, 1)$ are the computational basis for the two-qubit space. Since we have full control over the location of the vortices, we can tune our time-evolution operator to act as a $\sqrt{\text{SWAP}}$ gate up to some single-qubit σ_z operations, as shown in Sec. 5.10. This $\sqrt{\text{SWAP}}$ gate and previously introduced single-qubit rotations constitute a gate set for universal quantum computation [252, 253]. We stress again that this proximity-based scheme of two-qubit gate is only possible because the current system allows enhanced freedom to change the locations of Floquet vortex states. This is a big advantage that Floquet vortex state qubits have over other qubits based on solid-state systems such as quantum dots [254–256].

While the state preparation in Floquet systems is a challenging problem in general, one may be able to prepare the desired Floquet state by using proper bosonic and fermionic reservoirs through dissipative engineering [197,199,257]. Once the initialization method is established, the desired qubit state can be prepared by controlling the backgate voltage, similar to the initialization procedure in quantum-dot qubit systems.

5.5 Application of Rotating Wave Approximation

As stated in the main text, we consider following model Hamiltonian $H_0 = (vk_x, \pm vk_y, M) \cdot \sigma = \mathbf{D_k} \cdot \sigma$ for our semiconductor. We now consider the electromagnetic radiation $\mathcal{A}(\mathbf{r}, t)$. Then the minimal coupling $\mathbf{k} \to \mathbf{k} + e\mathcal{A}(\mathbf{r}, t)$ leads to the

following time-dependent Hamiltonian,

$$H(t) \;=\; H_0 + ev\mathcal{A}(\mathbf{r},t)\cdot\sigma = H_0 + V(t) = H_0 + \left[\mathbf{V}e^{i\omega t} + \text{c.c.}\right]\cdot\sigma. \qquad (5.8)$$

Then the projection operators to conduction and valence bands are

$$P_c = \int d^2\mathbf{k} P_{c,\mathbf{k}} = \int d^2\mathbf{k}(1+\mathbf{d_k})/2, \quad P_v = \int d^2\mathbf{k} P_{v,\mathbf{k}} = \int d^2\mathbf{k}(1-\mathbf{d_k})/2, \quad (5.9)$$

where $\mathbf{d_k} = \mathbf{D_k}/|\mathbf{D_k}|$. Considering the rotating frame $U(t) = P_c e^{-i\omega t} + P_v e^{i\omega t}$, the rotated Hamiltonian is

$$\begin{aligned} H_{\text{rot}} &= -iU^\dagger(t)\partial_t U(t) + U^\dagger(t)H(t)U(t) \\ &= \frac{\omega}{2}(P_v - P_c) + \mathbf{D_k}\cdot\sigma + P_c V(t) P_c + P_v V(t) P_v \\ &\quad + e^{i\omega t} P_c V(t) P_v + e^{-i\omega t} P_v V(t) P_c. \end{aligned} \qquad (5.10)$$

In the weak field regime $evA_{\max} = \Omega_0 \ll \omega$, we can obtain RWA Hamiltonian by dropping fast oscillating terms from H_{rot},

$$H_{\text{RWA}} = \left(\mathbf{D_k} - \frac{\omega}{2}\mathbf{d_k}\right)\cdot\sigma + \mathcal{V}_\mathbf{k}, \qquad (5.11)$$

where

$$\begin{aligned}
\mathcal{V}_{\mathbf{k}} &= P_{c,\mathbf{k}}(\mathbf{V}^*\cdot\sigma)P_{v,\mathbf{k}} + P_{v,\mathbf{k}}(\mathbf{V}\cdot\sigma)P_{c,\mathbf{k}} \\
&= \left\{\mathrm{Re}\mathbf{V}\cdot\sigma + i[\mathrm{Im}\mathbf{V}\cdot\sigma, \mathbf{d}_{\mathbf{k}}\cdot\sigma] - (\mathbf{d}_{\mathbf{k}}\cdot\sigma)(\mathrm{Re}\mathbf{V}\cdot\sigma)(\mathbf{d}_{\mathbf{k}}\cdot\sigma)\right\}/2 \\
&= \frac{1}{2}\left[\mathrm{Re}\mathbf{V} + (\mathbf{d}_{\mathbf{k}}\times\mathrm{Im}\mathbf{V} - \mathrm{Im}\mathbf{V}\times\mathbf{d}_{\mathbf{k}}) - (\mathbf{d}_{\mathbf{k}}\cdot\mathrm{Re}\mathbf{V})\mathbf{d}_{\mathbf{k}} + (\mathbf{d}_{\mathbf{k}}\times\mathrm{Re}\mathbf{V})\times\mathbf{d}_{\mathbf{k}}\right]\cdot\sigma \\
&\quad + \frac{i}{2}\left[\mathrm{Im}\mathbf{V}\cdot\mathbf{d}_{\mathbf{k}} - \mathbf{d}_{\mathbf{k}}\cdot\mathrm{Im}\mathbf{V} - (\mathbf{d}_{\mathbf{k}}\times\mathrm{Re}\mathbf{V})\cdot\mathbf{d}_{\mathbf{k}}\right]. \qquad (5.12)
\end{aligned}$$

For small detuning regime $\delta = \omega - 2M \ll \omega$, $\delta \simeq v^2k_0^2/M$ and $vk_0 \ll M$. Then, for small momenta $|\mathbf{k}| = O(k_0)$,

$$\begin{aligned}
\mathbf{d}_{\mathbf{k}} &= (d_{x,\mathbf{k}}, d_{y,\mathbf{k}}, d_{z,\mathbf{k}}) = \frac{1}{\sqrt{M^2+v^2\mathbf{k}^2}}(vk_x, vk_y, M) \\
&= \left(\frac{vk_x}{M}, \frac{vk_y}{M}, 1 - \frac{v^2\mathbf{k}^2}{2M^2}\right) + O\left(\frac{v^3k_0^3}{M^3}\right), \qquad (5.13)
\end{aligned}$$

$$\begin{aligned}
\left(\mathbf{D}_{\mathbf{k}} - \frac{\omega}{2}\mathbf{d}_{\mathbf{k}}\right)\cdot\sigma &= \left(1 - \frac{\omega/2}{\sqrt{M^2+v^2\mathbf{k}^2}}\right)(vk_x, vk_y, M)\cdot\sigma \\
&= \frac{v^2}{2M}(\mathbf{k}^2 - k_0^2)\sigma_z + O\left(\frac{v^3k_0^3}{M^2}\right). \qquad (5.14)
\end{aligned}$$

Now we consider a linearly polarized light carrying OAM. The magnetic potential of this field is $\mathcal{A}(\mathbf{r},t) = \left[A_0(r)e^{im\phi}e^{i\omega t} + \text{c.c.}\right]\hat{\mathbf{x}}$. With this, $V_y = 0$, and from Eq.

(5.12),

$$\begin{aligned}
\mathcal{V}_{\mathbf{k}} &= \frac{1}{2}\left[\left(\mathrm{Re}V_x + d_{z,\mathbf{k}}\mathrm{Re}V_x d_{z,\mathbf{k}} - d_{x,\mathbf{k}}\mathrm{Re}V_x d_{x,\mathbf{k}} + d_{y,\mathbf{k}}\mathrm{Re}V_x d_{y,\mathbf{k}}\right)\sigma_x\right. \\
&\quad + \left(d_{z,\mathbf{k}}\mathrm{Im}V_x + \mathrm{Im}V_x d_{z,\mathbf{k}} - d_{x,\mathbf{k}}\mathrm{Re}V_x d_{y,\mathbf{k}} - d_{y,\mathbf{k}}\mathrm{Re}V_x d_{x,\mathbf{k}}\right)\sigma_y \\
&\quad \left. + \left(-d_{y,\mathbf{k}}\mathrm{Im}V_x - d_{x,\mathbf{k}}\mathrm{Re}V_x d_{z,\mathbf{k}} - d_{z,\mathbf{k}}\mathrm{Re}V_x d_{x,\mathbf{k}}\right)\sigma_z\right] \\
&\quad + \frac{i}{2}\left(\mathrm{Im}V_x d_{x,\mathbf{k}} - d_{x,\mathbf{k}}\mathrm{Im}V_x - d_{z,\mathbf{k}}\mathrm{Re}V_x d_{y,\mathbf{k}} + d_{y,\mathbf{k}}\mathrm{Re}V_x d_{z,\mathbf{k}}\right) \\
&= \mathrm{Re}V_x\sigma_x + \mathrm{Im}V_x\sigma_y + O\left(evA_{\max}\frac{vk_0}{M}\right). \qquad (5.15)
\end{aligned}$$

Therefore, with further assumption of weak field $\Omega_0 \ll \sqrt{\delta M}$, the RWA Hamiltonian becomes

$$\begin{aligned}
H_{\mathrm{RWA}} &= \frac{v^2}{2M}\left(\mathbf{k}^2 - k_0^2\right)\sigma_z + \left[evA_0(r)e^{-im\phi}\sigma_+ + \mathrm{H.c.}\right] + O\left(evA_{\max}\frac{vk_0}{M}\right) \\
&= \frac{\delta}{2}\left(\frac{\mathbf{k}^2}{k_0^2} - 1\right)\sigma_z + \left[\Omega(r)e^{-im\phi}\sigma_+ + \mathrm{H.c.}\right] + O\left(\Omega_0\sqrt{\frac{\delta}{M}}\right), \qquad (5.16)
\end{aligned}$$

so we derived the RWA Hamiltonian in Eq. (5.2).

Due to the OAM of the light, the RWA Hamiltonian H_{RWA} and the static semiconductor Hamiltonian H_0 have different symmetries. While H_0 commutes with electronic OAM $-i\partial_\phi$, H_{RWA} commutes with pseudo-OAM $\hat{l} = -i\partial_\phi + (m/2)\sigma_z$. To demonstrate this, we use $[-i\partial_\phi, k_x] = ik_y$ and $[-i\partial_\phi, k_y] = -ik_x$. These yield $[-i\partial_\phi, k_x \pm ik_u] = \pm(k_x \pm ik_y)$ and $[-i\partial_\phi, \mathbf{k}^2] = 0$, therefore

$$\begin{aligned}
[-i\partial_\phi, H_{\mathrm{RWA}}] &= -m\left(\Omega(r)e^{-im\phi}\sigma_+ - \mathrm{H.c.}\right), \\
[\sigma_z, H_{\mathrm{RWA}}] &= 2\left(\Omega(r)e^{-im\phi}\sigma_+ - \mathrm{H.c.}\right), \qquad (5.17)
\end{aligned}$$

so $[-i\partial_\phi + (m/2)\sigma_z, H_{\rm RWA}] = 0$. Since l is a good quantum number, the wave functions for each l have the form of

$$\psi_{n,l}(\mathbf{r}) = \left(e^{i(l-m/2)\phi}u_{n,+}(r), e^{i(l+m/2)\phi}u_{n,-}(r)\right)^T, \tag{5.18}$$

where n is the branch index. With this, $H_{\rm RWA}$ leads to following eigenvalue problem for each l,

$$\begin{aligned} E_{n,l}u_{n,l,\pm}(r) &= \mp\frac{\delta^2}{2k_0^2}\left(\partial_r^2 + \frac{1}{r}\partial_r - \frac{(l\mp m/2)^2}{r^2} + k_0^2\right)u_{n,l,\pm}(r) \\ &\quad +\Omega(r)u_{n,l,\mp}(r). \end{aligned} \tag{5.19}$$

By observing this Hamiltonian, one can see this Hamiltonian preserves the particle-hole symmetry $\psi_{n,-l}(\mathbf{r}) = i\sigma_y\psi^*_{|m|+1-n,l}(\mathbf{r})$ and $E_{n,-l} = -E_{|m|+1-n,l}$. Here the branch index n should alter to $|m|+1-n$ as l changes to $-l$.

5.6 Number of Floquet Vortex States Branches

Since $H_{\rm RWA}(\mathbf{k})$ in Eq. (5.2) is particle-hole symmetric and gapped except the vortex core, the intragap modes develop around the vortex core are expected to cross the zero energy, if any exists. We may use the semiclassical approach introduced in Ref. [248] to investigate the number of such intragap modes. Let us consider the Hamiltonian in the classical regime, $H_{\rm RWA} \to \mathbf{H}\cdot\sigma$, where the momentum and the position commute each other. This semiclassical treatment is justified as long as $k_0\xi \gg 1$. Here, the vector $\mathbf{H} = \mathbf{H}(k, r, \phi)$ resides on the 3D parameter

space (k, r, ϕ). Now such Hamiltonian yields energy $E^2(k, r, \phi) = |\mathbf{H}(k, r, \phi)|^2 = \delta^2(k^2/k_0^2 - 1)^2/4 + \Omega(r)^2$ and $E = 0$ is achieved at $k = k_0$ and $r = 0$. To consider the surface surrounds this zero point, let us consider the surface $|E| = \Delta E$ for small energy ΔE. Such surface would be located in the vicinity of that zero point, so we can write $k = k_0 + \Delta k$ and $r = \Delta r$. To the leading order, This surface can be written as $\Delta E^2 = (\delta/k_0)^2 \Delta k^2 + \Omega(\Delta r)^2$. Without loss of generality, we can regard $\Omega(\Delta r) = \lambda \Delta r$. Now the surface $|E| = \Delta E$ becomes an ellipsoid and can be parameterized by the polar angle θ and the azimuthal angle ϕ: $\Delta k = (k_0 \Delta E/\delta) \cos\theta$, $\Delta r = (\Delta E/\lambda) \sin\theta$, $\Delta x = \Delta r \cos\phi$, $\Delta y = \Delta r \sin\phi$. Then the skyrmion number of $\mathbf{H}$ on this ellipsoid is equal to the number of branches that passes the zero energy in the intragap spectrum. Since the skyrmion number is a topological invariant, we did not lose the generality even if the actual behavior of $\Omega(r)$ for small r is not linear. For the current parameterization,

$$\begin{aligned} \mathbf{H}|_{|E|=\Delta E, \phi_k} &= \Omega(r) \left[\cos(m\phi)\hat{\mathbf{x}} + \sin(m\phi)\hat{\mathbf{y}}\right] + \frac{\delta}{2}\left(\frac{k^2}{k_0^2} - 1\right)\hat{\mathbf{z}}\Big|_{|E|=\Delta E, \phi_k} \\ &= \Delta E \left[\sin\theta \left(\cos(m\phi)\hat{\mathbf{x}} + \cos(m\phi)\hat{\mathbf{y}}\right) + \cos\theta \hat{\mathbf{z}}\right] = \Delta E \ \hat{\mathbf{H}}(\theta, \phi), \quad (5.20) \end{aligned}$$

and now the skyrmion number is calculated as

$$N_{\text{mid}} = \frac{1}{4\pi} \int_0^{2\pi} d\phi \int_0^{\pi} d\theta \left(\frac{\partial \hat{\mathbf{H}}}{\partial \theta} \times \frac{\partial \hat{\mathbf{H}}}{\partial \phi}\right) \cdot \hat{\mathbf{H}} = \frac{1}{4\pi} \int_0^{2\pi} d\phi \int_0^{\pi} d\theta \ m \sin\theta = m. \quad (5.21)$$

Note that the number of intragap branches N_{mid} is solely determined by the winding number of the applied field, regardless of the winding number along the momentum

direction. Yet, the presence of intragap branches crossing the zero energy does not guarantee the existence of the exact zero mode, since the mini gap can develop within each branch in the process of quantization. For further analysis, a fully quantum mechanical approach is required.

5.7 Estimation of Energy Separations in Large Optical Vortex Regime

Following the formalism in Ref. [251], we find the energy separations between the Floquet vortex states and the intragap state branches, respectively,

$$\omega_0 = \frac{\int_0^\infty \frac{\Omega(r)}{r} e^{-(2k_0/\delta)\int_0^r \Omega(r')dr'} dr}{k_0 \int_0^\infty e^{-(2k_0/\delta)\int_0^r \Omega(r')dr'} dr}, \quad \tilde{\omega}_0 = \frac{\delta(\pi/2)}{k_0 \int_0^\infty e^{-(2k_0/\delta)\int_0^r \Omega(r')dr'} dr}, \tag{5.22}$$

for low energy, low pseudo-OAM, and large optical vortex regime, as explained in Eq. (5.4).

In this appendix, we demonstrate how these energy separations depend on radiation parameters such as Ω_0, δ, ω as well as the radial profile of the applied light beam. For this, we estimate ω_0 and $\tilde{\omega}_0$ for variants of radial beam profile. Specifically, we consider the radial profile

$$\Omega(r) = \begin{cases} \Omega_0(r/\xi)^q & \text{for } r \leq \xi \\ \Omega_0 & \text{for } r > \xi \end{cases}, \quad q \geq 1. \tag{5.23}$$

With this, we define $\mathcal{F}(r) \equiv \exp\left[-(2k_0/\delta)\int_0^r \Omega(r')dr'\right]$ and it becomes

$$\mathcal{F}(r) = \begin{cases} \exp\left[-\frac{2k_\delta\xi}{q+1}\left(\frac{r}{\xi}\right)^{q+1}\right] & \text{for } r \le \xi \\ \exp\left[-2k_\delta\left(r - \frac{q}{q+1}\xi\right)\right] & \text{for } r > \xi \end{cases}. \tag{5.24}$$

With $k_\delta\xi \gg 1$, this $\mathcal{F}(r)$ can be roughly estimated by a step function $\theta(x) \equiv [\mathrm{sgn}(x)+1]/2$,

$$\mathcal{F}(r) \simeq \theta\left(r_{\rm cut} - r\right),\ r_{\rm cut} = O\left(\xi\left(\frac{q+1}{2k_\delta\xi}\right)^{1/(q+1)}\right). \tag{5.25}$$

With this,

$$\begin{aligned} \int_0^\infty \frac{\Omega(r)}{r}\mathcal{F}(r)dr &\simeq \int_0^{r_{\rm cut}} \Omega_0 \frac{r^{q-1}}{\xi^q}dr = \frac{\Omega_0 r_{\rm cut}^q}{q\xi^q} = O\left(\Omega_0[k_\delta\xi]^{-q/(q+1)}\right), \\ \int_0^\infty \mathcal{F}(r)dr &\simeq r_{\rm cut} = O\left(\xi(k_\delta\xi)^{-1/(q+1)}\right), \end{aligned} \tag{5.26}$$

then

$$\begin{aligned} \omega_0 &= \frac{\int_0^\infty r^{-1}\Omega(r)\mathcal{F}(r)dr}{k_0\int_0^\infty \mathcal{F}(r)dr} \simeq O\left(\Omega_0(k_0\xi)^{-1}(k_\delta\xi)^{-(q-1)/(q+1)}\right) \\ \tilde{\omega}_0 &= \frac{\delta(\pi/2)}{k_0\int_0^\infty \mathcal{F}(r)dr} \simeq O\left(\delta(k_0\xi)^{-1}(k_\delta\xi)^{1/(q+1)}\right). \end{aligned} \tag{5.27}$$

As seen in this estimation, energy separations ω_0 and $\tilde{\omega}_0$ depend not only on radiation parameters like Ω_0, δ, ω, but also on parameters related to the size (ξ) and shape (q) of the radial profile of the beam.

From these results, we can further estimate the number of vortex modes in a

branch as

$$2\Omega_0/\omega_0 = O\left(k_0\xi(k_\delta\xi)^{(q-1)/(q+1)}\right). \tag{5.28}$$

Also, we can estimate the angular momentum difference between branches as

$$\tilde{\omega}_0/\omega_0 = O\left(\frac{k_0}{k_\delta}(k_\delta\xi)^{q/(q+1)}\right). \tag{5.29}$$

With $q \geq 1$, the lower bound of these estimations are given as $2\Omega_0/\omega_0 = O\left(k_0\xi\right)$ and $\tilde{\omega}_0/\omega_0 = O\left(k_0 k_\delta^{-1}\sqrt{k_\delta\xi}\right)$.

5.8 Illumination of Circularly Polarized Light

The hybridization gap for the bulk part of systems with linearly polarized light is in the order of Ω_0. For the most of systems with different beam polarization, it is still true and therefore results in similar RWA Hamiltonian with Eq. (5.2). However, the situation is different for circularly polarized light. As explained in Ref. [188], a semiconductor valley with valley Hamiltonian $H_{0,\pm} = (vk_x, \pm vk_y, M)$ becomes a Floquet Chern insulator when illuminated by circularly polarized light $\mathcal{A}_\pm(\mathbf{r}, t) = A(\mathbf{r})(\hat{\mathbf{x}} \pm i\hat{\mathbf{y}})e^{i\omega t} + \text{c.c.}$. In such Floquet Chern insulator, the size of hybridization gap is in the order of $\delta\Omega_0/M$, instead of Ω_0. In this appendix, we derive the RWA Hamiltonian for the light carrying OAM with this circular polarization. Then we calculate the wavefunctions and dispersion of Floquet vortex states given by that Hamiltonian. For simplicity, we only consider the valley Hamiltonian $H_0 = H_{0,+}$

and the field $\mathcal{A}(\mathbf{r},t)=\mathcal{A}_+(\mathbf{r},t)$ from now on.

The RWA Hamiltonian derived in appendix A is valid regardless of $\mathcal{A}(\mathbf{r},t)$ up to Eq. (5.14). By using $\mathcal{A}(\mathbf{r},t)=A(\mathbf{r})(\hat{\mathbf{x}}+i\hat{\mathbf{y}})e^{i\omega t}+\text{c.c.}$, we have $V_y=iV_x$. This yields

$$\begin{aligned}\mathcal{V}_{\mathbf{k}} &= \frac{1}{2}\left[\mathrm{Re}\mathbf{V}+(\mathbf{d_k}\times\mathrm{Im}\mathbf{V}-\mathrm{Im}\mathbf{V}\times\mathbf{d_k})-(\mathbf{d_k}\cdot\mathrm{Re}\mathbf{V})\mathbf{d_k}+(\mathbf{d_k}\times\mathrm{Re}\mathbf{V})\times\mathbf{d_k}\right]\cdot\sigma \\ &\quad +\frac{i}{2}\left[\mathrm{Im}\mathbf{V}\cdot\mathbf{d_k}-\mathbf{d_k}\cdot\mathrm{Im}\mathbf{V}-(\mathbf{d_k}\times\mathrm{Re}\mathbf{V})\cdot\mathbf{d_k}\right] \\ &= (1-d_{z,\mathbf{k}})(\mathrm{Re}V_x\sigma_x-\mathrm{Im}V_x\sigma_y)(1-d_{z,\mathbf{k}})/2 \\ &\quad -\frac{1}{2}\left[(d_{x,\mathbf{k}}-id_{y,\mathbf{k}})(\mathrm{Re}V_x-i\mathrm{Im}V_x)(d_{x,\mathbf{k}}-id_{y,\mathbf{k}})\sigma_+ +\text{H.c.}\right]+O\left(\frac{evA_{\max}v^3k_0^3}{M^3}\right).\end{aligned} \tag{5.30}$$

Then the RWA Hamiltonian becomes

$$\begin{aligned}H_{\mathrm{RWA}} &= -\frac{ev^3}{2M^2}\left[(k_x+ik_y)A_0(r)e^{im\phi}(k_x+ik_y)\sigma_- +\text{H.c.}\right] \\ &\quad +\frac{v^2}{2M}(\mathbf{k}^2-k_0^2)\sigma_z+O\left(\frac{v^3k_0^3}{M^2}\right) \\ &= -\frac{\delta}{2M}\left[\frac{(k_x+ik_y)}{k_0}\Omega(r)e^{im\phi}\frac{(k_x+ik_y)}{k_0}\sigma_- +\text{H.c.}\right] \\ &\quad +\frac{\delta}{2}\left(\frac{\mathbf{k}^2}{k_0^2}-1\right)\sigma_z+O\left(\delta\sqrt{\frac{\delta}{M}}\right).\end{aligned} \tag{5.31}$$

In the bulk far from $r=0$, this system becomes a Floquet Chern insulator and therefore hosts edge states in the middle of hybridization gap. These states are localized at the boundary of the sample and has nothing to do with the OAM of the beam. We aim to find fully quantum mechanical solution for intragap states localized around the optical vortex. For this, we use a similar method used in

Ref. [222, 249–251]. Note that, due to scale change, we redefine $k_\delta = k_0\Omega_0/M$ for this section.

For the simplicity of discussion, we normalize the RWA Hamiltonian as $h = (M/v^2)H_{\rm RWA}$. We first demonstrate that h commutes with pseudo-OAM $\hat{l} = -i\partial_\phi + (m/2+1)\sigma_z$. Note that the pseudo-OAM operator here differs from the pseudo-OAM operator for the systems with non-circularly polarized light by an extra term of σ_z. Similar to the linear polarization case, we use $[-i\partial_\phi, k_x] = ik_y$, $[-i\partial_\phi, k_y] = -ik_x$, $[-i\partial_\phi, k_x \pm ik_u] = \pm(k_x \pm ik_y)$, and $[-i\partial_\phi, \mathbf{k}^2] = 0$, therefore

$$\begin{aligned}
[-i\partial_\phi, h] &= -(m+2)\frac{\Omega(r)}{2M}\left[(k_x - ik_y)e^{-im\phi}(k_x - ik_y)\sigma_+ - \text{H.c.}\right], \\
[\sigma_z, h] &= \frac{\Omega(r)}{M}\left[(k_x - ik_y)e^{-im\phi}(k_x - ik_y)\sigma_+ - \text{H.c.}\right],
\end{aligned} \tag{5.32}$$

so we eventually have $[-i\partial_\phi + (m/2+1)\sigma_z, h] = 0$. Therefore, l is a conserved quantity and we can block-diagonalize h along this l. Within the block for l, wavefunctions can be written as in Eq. (5.3),

$$\psi_l(\mathbf{r}) = \left(e^{il_+\phi}u_+(r), e^{il_-\phi}u_-(r)\right)^T, \tag{5.33}$$

where $l_\pm = l \mp (m/2+1)$. The eigenstates satisfy

$$\begin{aligned}
\epsilon u_+(r) &= -\frac{1}{2}\left(\partial_r^2 + \frac{1}{r}\partial_r - \frac{l_+^2}{r^2} + k_0^2\right) u_+(r) + \frac{\Omega(r)}{2M}\left(\partial_r^2 + \frac{2l+1}{r}\partial_r + \frac{l_+ l_-}{r^2}\right) u_-(r) \\
&\quad + \frac{\Omega'(r)}{2M}\left(\partial_r + \frac{l_-}{r}\right) u_-(r), \\
\epsilon u_-(r) &= \frac{1}{2}\left(\partial_r^2 + \frac{1}{r}\partial_r - \frac{l_-^2}{r^2} + k_0^2\right) u_-(r) + \frac{\Omega(r)}{2M}\left(\partial_r^2 - \frac{2l-1}{r}\partial_r + \frac{l_+ l_-}{r^2}\right) u_+(r) \\
&\quad + \frac{\Omega'(r)}{2M}\left(\partial_r - \frac{l_+}{r}\right) u_+(r). \qquad (5.34)
\end{aligned}$$

As in the system with linearly polarized light, this RWA Hamiltonian preserves the particle-hole symmetry. By replacing l by $-l$ in this equation, $l_\pm \to -l_\mp$, so one can readily show that $\psi_{-l}(\mathbf{r}) = i\sigma_y \psi_l^*(\mathbf{r})$ with $\epsilon|_{-l} = -\epsilon|_l$. Equivalent to Eq. (5.34),

$$\begin{aligned}
\left(\epsilon + \frac{\beta}{2r^2}\right) u_+(r) &= -\frac{1}{2}\left(\partial_r^2 + \frac{1}{r}\partial_r - \frac{\alpha^2}{r^2} + k_0^2\right) u_+(r) + \frac{\Omega'(r)}{2M}\left(\partial_r + \frac{l_-}{r}\right) u_-(r) \\
&\quad + \frac{\Omega(r)}{2M}\left(\partial_r^2 + \frac{2l+1}{r}\partial_r + \frac{l_+ l_-}{r^2}\right) u_-(r), \\
\left(\epsilon + \frac{\beta}{2r^2}\right) u_-(r) &= \frac{1}{2}\left(\partial_r^2 + \frac{1}{r}\partial_r - \frac{\alpha^2}{r^2} + k_0^2\right) u_-(r) + \frac{\Omega'(r)}{2M}\left(\partial_r - \frac{l_+}{r}\right) u_+(r) \\
&\quad + \frac{\Omega(r)}{2M}\left(\partial_r^2 - \frac{2l-1}{r}\partial_r + \frac{l_+ l_-}{r^2}\right) u_+(r), \qquad (5.35)
\end{aligned}$$

where $\alpha = \sqrt{l^2 + (m/2+1)^2}$ and $\beta = l(m+2)$. While it is difficult to find the generic solution for this equation, we can find the low-energy solution for the regime $l^2/k_0 \ll k_\delta^{-1} \ll \xi$. Let us consider a radius r^* such that $l^2/k_0 \ll r^* \ll k_\delta^{-1}$. For $r \ll r^*$, $\Omega(r) \to 0$ and therefore we can decouple $u_+(r)$ and $u_-(r)$ in Eq. (5.34),

$$\left(\partial_r^2 + \frac{1}{r}\partial_r - \frac{l_\pm^2}{r^2} + k_0^2 \pm 2\epsilon\right) u_\pm(r) = 0, \qquad (5.36)$$

which yields the solution

$$u_{\pm}(r) = C_{\pm} J_{l\mp(m/2+1)} \left(\sqrt{(k_0^2 \pm 2\epsilon)} r \right) \tag{5.37}$$

where $J_\nu(r)$ is the Bessel function of the first kind. The Bessel function of the second kind can be ruled out since the solution should be finite at $r = 0$. In the low-energy theory, $\epsilon \ll k_0^2$, we can write $\sqrt{k_0^2 \pm 2\epsilon} \simeq k_0 \pm p$ where $p = \epsilon/k_0 \ll k_0$.

For $r \gg r^*$, we take the ansatz

$$u_{\pm}(r) = f_{\pm}(r) H_\alpha^{(1)}(k_0 r) + g_{\pm}(r) H_\alpha^{(2)}(k_0 r) \tag{5.38}$$

where $H_\nu^{(1)}(x), H_\nu^{(2)}(x)$ are the Hankel functions of the first kind and the second kind. Let us deal with the solutions for $f_\pm(r)$ first. Let us denote $H_\alpha^{(1)}(x) = H(x)$ for short. Denoting that $(\partial_r^2 + r^{-1}\partial_r - \alpha^2/r^2 + k_0^2) H(k_0 r) = 0$, Eq. (5.35) can be written as

$$\begin{aligned}
&\left(\epsilon + \frac{\beta}{2r^2}\right) f_+ H \\
&= -\frac{1}{2}\left(f_+'' H + 2 f_+' H' + \frac{f_+' H}{r} \right) + \frac{\Omega'}{2M}\left(f_-' H + f_- H' + \frac{l_-}{r} \right) \\
&\quad + \frac{\Omega}{2M}\left(f_-'' H + 2 f_-' H' + f_- H'' + \frac{2l+1}{r}(f_-' H + f_- H') + \frac{l_+ l_-}{r^2} f_- H \right), \\
&\left(\epsilon + \frac{\beta}{2r^2}\right) f_- H \\
&= \frac{1}{2}\left(f_-'' H + 2 f_-' H' + \frac{f_-' H}{r} \right) + \frac{\Omega'}{2M}\left(f_+' H + f_+ H' - \frac{l_+}{r} \right) \\
&\quad + \frac{\Omega}{2M}\left(f_+'' H + 2 f_+' H' + f_+ H'' - \frac{2l-1}{r}(f_+' H + f_+ H') + \frac{l_+ l_-}{r^2} f_+ H \right).
\end{aligned} \tag{5.39}$$

To simplify these equations, we estimate and compare the magnitude of different terms in these equations around $r = k_\delta^{-1}$. For this, we take the ansatz $f_\pm(r) = f_{\pm,(0)}(r)\exp[i\eta_\pm(r)]$ where $f'_{\pm,(0)}/f_{\pm,(0)} = O(k_\delta)$, $\eta_\pm = O(k_\delta/k_0)$, and $\eta'_\pm/\eta_\pm = O(k_\delta)$ around $r = (k_\delta)^{-1}$. We further restrict the eigenenergy to be $\epsilon = O\left(k_\delta^2\right)$. Assuming $|f_{+,(0)}/f_{-,(0)}| = O(1)$ and noting that $\partial_r H_\alpha^{(1)}(k_0 r) \simeq i k_0 H_\alpha^{(1)}(k_0 r)$ for $k_0 r \gg l^2$, the lowest order equations of Eq. (5.39) become

$$
\begin{aligned}
&O(k_0 k_\delta) : \mp i k_0 f'_{\pm,(0)} - k_0^2 \Omega (2M)^{-1} f_{\mp,(0)} = 0, \\
&O\left(k_\delta^2\right) : \left(\epsilon + \frac{\beta}{2r^2}\right) f_{\pm,(0)} = k_0 f'_{\pm,(0)}\eta_\pm + k_0 f_{\pm,(0)}\eta'_\pm \mp \frac{f'_{\pm,(0)}}{2r} \\
&\qquad\qquad \pm i\frac{k_0^2\Omega}{2M} f_{\mp,(0)}\eta_\mp \pm i\frac{k_0\Omega}{2Mr}(2l \pm 1) f_{\mp,(0)}.
\end{aligned}
\tag{5.40}
$$

By solving the equations of the order of $O(k_0 k_\delta)$, we get

$$
f_{+,(0)} = B\exp\left(-\frac{1}{2}(k_0/M)\int_0^r \Omega(r')dr'\right) = -i f_{-,(0)}. \tag{5.41}
$$

This solution indeed satisfies the supposition $f'_{\pm,(0)}/f_{\pm,(0)} = O(k_\delta)$. Then the equations of the order of $O\left(k_\delta^2\right)$ become

$$
k_0\eta'_\pm - \frac{k_0^2\Omega}{2M}(\eta_+ + \eta_-) = \epsilon + \frac{\beta}{2r^2} + \frac{k_0\Omega}{Mr}\left(l \pm \frac{1}{4}\right), \tag{5.42}
$$

or equivalently,

$$
\begin{aligned}
k_0\partial_r(\eta_+ + \eta_-) - \frac{k_0^2\Omega}{M}(\eta_+ + \eta_-) &= 2\epsilon + \frac{\beta}{r^2} + 2l\frac{k_0\Omega}{Mr}, \\
k_0\partial_r(\eta_+ - \eta_-) &= \frac{k_0\Omega}{2Mr}.
\end{aligned} \tag{5.43}
$$

The solutions of these equations can be found as

$$
\begin{aligned}
\eta_+(r) + \eta_-(r) &= -\frac{2}{k_0}e^{\frac{k_0}{M}\int_0^r \Omega(r')dr'}\int_r^\infty dr'\left(\epsilon + \frac{\beta}{2r'^2} + l\frac{k_0\Omega(r')}{Mr'}\right)e^{-\frac{k_0}{M}\int_0^{r'}\Omega(r'')dr''}, \\
\eta_+(r) - \eta_-(r) &= \int_0^r \frac{\Omega(r')}{2Mr'}dr'.
\end{aligned} \tag{5.44}
$$

We have $(k_0/M)\int_0^{1/k_\delta}\Omega(r)dr = O(1)$, $\epsilon + \beta/(2r^2) + lk_0\Omega(r)/(Mr) \leq O\left(k_\delta^2\right)$ for $r \geq O(k_\delta^{-1})$, and $\lim_{r\to 0}\Omega(r)/r < \infty$, so the suppositions $\eta_\pm = O(k_\delta/k_0)$ and $\eta_\pm'/\eta_\pm = O(k_\delta)$ are justified around $r = (k_\delta)^{-1}$. One might worry that $\eta_+(r) - \eta_-(r)$ diverges as $r \to \infty$, but $\eta_+(r) - \eta_-(r)$ is bounded to $O(k_\delta/k_0)$ as long as $r \leq O\left(k_\delta^{-1}\right)$ and the wavefunction vanishes for $r \gg k_\delta^{-1}$ due to the behaviors of $f_{\pm,(0)}(r)$, so the solutions become consistent.

We can also obtain the solutions for $g_\pm(r)$ by taking the complex conjugate on Eq. (5.39) since $\partial_r H_\alpha^{(2)}(k_0 r) \simeq -ik_0 H_\alpha^{(2)}(k_0 r)$, therefore $g_\pm(r) = f_\pm^*(r)$. Finally, we can write down $u_\pm(r)$ for $r \gg r^*$ as

$$
\begin{aligned}
u_\pm(r) &= i^{(1\mp 1)/2}Be^{-\frac{1}{2}(k_0/M)\int_0^r \Omega(r')dr'} \\
&\quad \times\left(e^{\pm i[\eta_\pm(r)\pm\kappa]}H_\alpha^{(1)}(k_0 r) \pm e^{\mp i[\eta_\pm(r)\pm\kappa]}H_\alpha^{(2)}(k_0 r)\right)
\end{aligned} \tag{5.45}
$$

for some relative phase κ. Now let us match the solutions in Eq. (5.37) and Eq. (5.45) at $r = r^*$. For this, with $k_0 r^* \gg l^2$, we can use the asymptotic forms of Bessel functions,

$$J_\nu(x) \simeq \sqrt{\frac{2}{\pi x}} \cos\left(x - \frac{2\nu+1}{4}\pi + \frac{4\nu^2-1}{8x}\right), \tag{5.46}$$
$$H_\nu^{(1),(2)}(x) \simeq \sqrt{\frac{2}{\pi x}} \exp\left[\pm i\left(x - \frac{2\nu+1}{4}\pi + \frac{4\nu^2-1}{8x}\right)\right],$$

for $\nu = O(l)$. Now from Eq. (5.37),

$$u_\pm(r^*) \simeq C_\pm \sqrt{\frac{2}{\pi(k_0 \pm p) r^*}} \tag{5.47}$$
$$\times \cos\left((k_0 \pm p) r^* - \frac{2l \mp m \mp 2 + 1}{4}\pi + \frac{(2l \mp m \mp 2)^2 - 1}{8(k_0 \pm p) r^*}\right).$$

By matching the constant factor in Eq. (5.45) as $B = C_+$, we have

$$u_\pm(r^*) \simeq C_+ \sqrt{\frac{2}{\pi k_0 r^*}} e^{-\frac{1}{2}(k_0/M)\int_0^{r^*}\Omega(r)dr}$$
$$\times \cos\left(\pm\eta_\pm(r^*) + \kappa + k_0 r^* - \frac{2\alpha+1}{4}\pi + \frac{4\alpha^2-1}{8k_0 r^*} + \frac{1 \mp 1}{2}\left(n - \frac{1}{2}\right)\pi\right) \tag{5.48}$$

where n is odd integer. Now by comparing Eq. (5.47) and Eq. (5.48), we have

$$\pm\eta_\pm(r^*) + \kappa \mp p r^* + \frac{2l - 2\alpha \mp m \mp 2}{4}\pi \pm \frac{\beta}{2k_0 r^*} + \frac{1 \mp 1}{2}\left(n - \frac{1}{2}\right)\pi$$
$$= O\left(\frac{p}{k_0^2 r^*}\right). \tag{5.49}$$

Here, we now let n be any integer by using the freedom to choose the sign of

C_+/C_-. In fact, this n serves as the branch index, so we put this branch index for each state from now on. That is, ψ_l $to\psi_{n,l}$, $u_\pm \to u_{n,\pm}$, $\eta_\pm \to \eta_{n,\pm}$, and $\epsilon \to \epsilon_n$. We now drop $O(\frac{p}{k_0^2 r^*})$ terms from Eq. (5.49) since $p/(k_0^2 r^*) = pr^*/(k_0 r^*)^2 \ll pr^*$, and $p/(k_0^2 r^*) = (p/k_0)/(k_0 r^*) \ll 1/(k_0 r^*) \ll 1$. Then, from Eq. (5.49), we get $\kappa = (\alpha - l - n + 1/2)(\pi/2) - \int_0^r dr' \Omega(r')/(4Mr')$ and

$$\eta_{n,+}(r) + \eta_{n,-}(r) = \frac{2\epsilon_n}{k_0} r^* - \frac{\beta}{k_0 r^*} + \left(n + \frac{m+1}{2}\right)\pi. \tag{5.50}$$

Now to match Eq. (5.44) and Eq. (5.50), let us evaluate the integrals in Eq. (5.44). First, we argue that the factor $\exp\left(\frac{k_0}{M}\int_0^{r^*} \Omega(r) dr\right)$ in Eq. (5.44) can be dropped out. To justify this, we suppose $\Omega(r)$ is a non-decreasing function that saturates to Ω_0 without loss of generality. Then

$$\begin{aligned} &\partial_{r^*}\left(\log e^{\frac{k_0}{M}\int_0^{r^*}\Omega(r)dr}\right) = \frac{k_0\Omega(r^*)}{M} < \frac{k_0\Omega_0}{M} \\ &\to\ 1 \le e^{\frac{k_0}{M}\int_0^{r^*}\Omega(r)dr} < e^{k_0\Omega_0 r^*/M} \simeq 1 \end{aligned} \tag{5.51}$$

since $r^* \ll k_\delta^{-1}$. This also matches the functional form of the slowly varying envelopes in Eq. (5.47) and Eq. (5.47). After getting rid of this factor from

$\eta_{n,+}(r) + \eta_{n,-}(r)$ in Eq. (5.44),

$$\begin{aligned}
\eta_{n,+}(r^*) + \eta_{n,-}(r^*) &= -\frac{2}{k_0}\int_{r^*}^{\infty}\left(\epsilon_n + \frac{\beta}{2r^2} + l\frac{k_0\Omega(r)}{Mr}\right)e^{-\frac{k_0}{M}\int_0^r \Omega(r')dr'}dr \\
&= \frac{2\epsilon_n r^*}{k_0} - \frac{2\epsilon_n}{k_0}\int_0^{\infty} e^{-\frac{k_0}{M}\int_0^r \Omega(r')dr'}dr + \left[\frac{\beta}{k_0 r}e^{-i\frac{k_0}{M}\int_0^r \Omega(r')dr'}\right]_{r=r^*}^{r=\infty} \\
&\quad + \int_{r^*}^{\infty}\frac{(\beta-2l)\Omega(r)}{Mr}e^{-\frac{k_0}{M}\int_0^r \Omega(r')dr'} \\
&= \frac{2\epsilon_n r^*}{k_0} - \frac{\beta}{k_0 r^*} - 2\epsilon_n\left(\frac{1}{k_0}\int_0^{\infty} e^{-\frac{k_0}{M}\int_0^r \Omega(r')dr'}dr\right) \\
&\quad + 2ml\left[R(\infty) - R(r^*)\right], \\
&\quad \text{where } R(r) = \int_0^r \frac{\Omega(r')}{2Mr'}e^{-\frac{k_0}{M}\int_0^{r'}\Omega(r'')dr''}dr'. \qquad (5.52)
\end{aligned}$$

We further argue that this $R(r^*)$ term can be dropped out from Eq. (5.52). For the estimation, we suppose $\Omega(r) = \Omega_0(r/\xi)^q$ for $r \le \xi$ and $\Omega(r) = \Omega_0$ for $r > \xi$, without loss of generality. Here, $1 \le q = O(1)$. Then $R(r^*) = O\left(\frac{k_\delta}{k_0}\left(\frac{r^*}{\xi}\right)^q\right)$ while $R\left(k_\delta^{-1}\right) = O\left(\frac{k_\delta}{k_0}\left(\frac{1}{k_\delta\xi}\right)^q\right)$. Since $r^* \ll k_\delta^{-1}$, $R(r^*) \ll R\left(k_\delta^{-1}\right) < R(\infty)$. Finally, by comparing Eq. (5.50) and Eq. (5.52), we obtain the low-energy spectrum as

$$\begin{aligned}
&E_{n,l} = ml\omega_0 + [n + (m+1)/2]\tilde{\omega}_0, \quad \text{where} \\
&\omega_0 = \frac{\delta\int_0^{\infty}\frac{\Omega(r)}{r}e^{-(k_0/M)\int_0^r \Delta(r')dr'}dr}{2Mk_0\int_0^{\infty}e^{-(k_0/M)\int_0^r \Delta(r')dr'}dr}, \quad \tilde{\omega}_0 = \frac{v^2 k_0(\pi/2)}{M\int_0^{\infty}e^{-(k_0/M)\int_0^r \Omega(r')dr'}dr}. \qquad (5.53)
\end{aligned}$$

Here, we recovered the factor (v^2/M) in $H_{\mathrm{RWA}} = (v^2/M)h$ as we restore $\epsilon_n \to E_{n,l}$. In Fig. 5.4(a), energy dispersion of circular polarized light for different vorticities m is shown. The non-linearity of dispersion for the illumination of CP light is also demonstrated in Fig. 5.4(b), as can be seen by decreasing the optical vortex size,

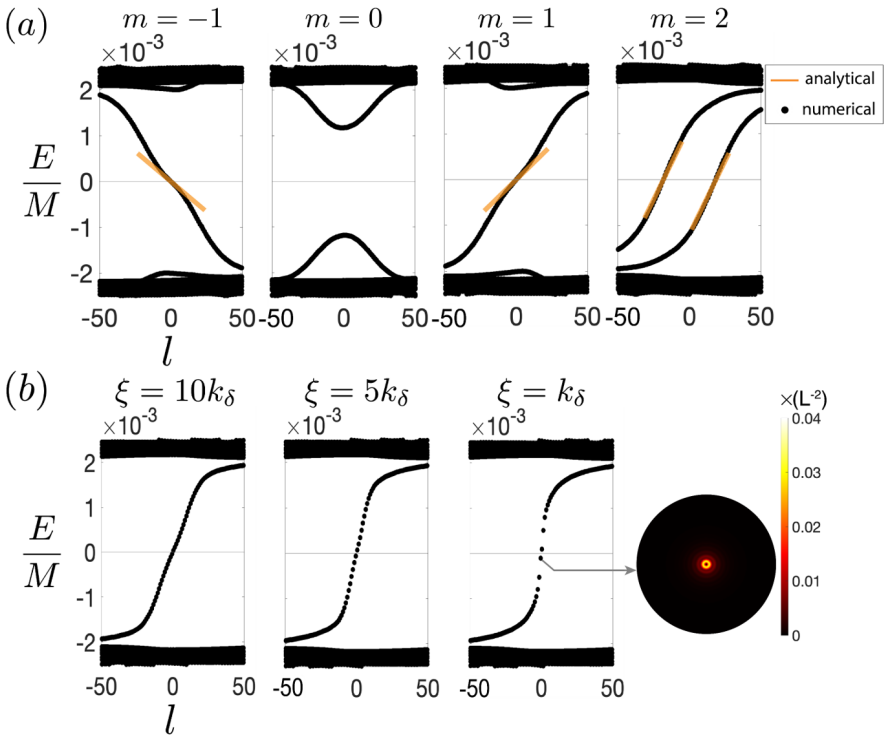

Figure 5.4: (a) Numerically calculated energy spectra as a function of pseudo-OAM l. We use $\omega = 2.05M$, $A_{\max} = 0.09M(ev)^{-1}$, and $A_0(r) = A_{\max}\,[1 - \exp\{-r^2/(2\xi^2)\}]$, $\xi = 20k_\delta$, and the disk sample of radius 25ξ. The numerical energy dispersions agree with the analytically expected spectra in that includes the number of intragap state branches and the slope of the linear dispersion for small $|E_l|$ and l. (b) Demonstration of dispersions' dependence on optical vortex size ξ for $m = 1$ with identical parameters with (a) except ξ and the disk size that the latter is fixed on $500k_\delta$. The linear region of the dispersion shrinks and the energy separation between subsequent states increases as ξ decreases. On the right-hand side, the electronic density profile of the vortex state for $m = 1$ just below the zero of the energy is illustrated.

the energy separation between subsequent vortex states increases.

5.9 Numerical Diagonalization for the Low-energy Spectrum

For more efficient numerical diagonalization of H_{RWA}, we can diagonalize the block-diagonalized Hamiltonian for each l, as presented in the eigenvalue problem

in Eq. (5.34). As shown in Eq. (5.18), wavefunctions for each l are written as

$$\psi_{n,l}(\mathbf{r}) = \left(e^{i(l-m/2)\phi}u_{n,+}(r), e^{i(l+m/2)\phi}u_{n,-}(r)\right)^T. \tag{5.54}$$

Yet, it is tricky to apply a naive finite difference method due to the boundary condition at $r = 0$. Rather, we use the basis which can diagonalize the Hamiltonian onto the space of $u_{n,+}(r)$ and $u_{n,-}(r)$, assuming the system is confined on a disk of radius R. That is, we use basis functions $\{u_{\pm,\alpha}(r)\}$ such that

$$\left[\partial_r^2 + \frac{1}{r}\partial_r - \frac{l_\pm^2}{r^2} + k_0^2 \pm 2\epsilon_{\pm,\alpha}\right] u_{\pm,\alpha}(r) = 0, \tag{5.55}$$

where eigenenergies $\epsilon_{\pm,\alpha}$ are set by the boundary condition $u_{\pm,\alpha}(R) = 0$. $\alpha \in \mathbb{N}$. Here, $l_\pm = l \mp m/2$. Indeed, Eq. (5.55) are the Bessel equations and we immediately find that $u_{\pm,\alpha}(r) = C_{\pm,\alpha}J_{l_\pm}(\sqrt{(k_0^2 \pm 2\epsilon_{\pm,\alpha})}r)$ since $u_{\pm,\alpha}(r)$ should be bounded at $r = 0$. The normalization factors $C_{\pm,\alpha}$ are determined by $\int_0^R |u_{\pm,\alpha}(r)|^2 r dr = 1$. Now suppose $z_\alpha^{(\nu)}$ is the αth non-negative zero of the Bessel function of order ν, $J_\nu(z)$. Then we have

$$\sqrt{(k_0^2 \pm 2\epsilon_{\pm,\alpha})}R = z_\alpha^{(l_\pm)} \leftrightarrow \epsilon_{\pm,\alpha} = \pm\frac{1}{2}\left(\frac{z_\alpha^{(l_\pm)}}{R}\right)^2 \mp \frac{k_0^2}{2}. \tag{5.56}$$

While there are infinitely many eigenfunctions $u_{\pm,\alpha}(r)$, we only take eigenfunctions with the N-smallest positive eigenenergies and the N-largest negative eigenenergies for each $u_{\pm,\alpha}(r)$, because we would like to calculate the low-energy spectrum around the zero energy. Since the eigenenergies are monotonic in α, we can label such

eigenfunctions as $\alpha = i_0 + 1, \cdots, i_0 + 2N$ for $u_{+,\alpha}(r)$ and $\alpha = j_0 + 1, \cdots, j_0 + 2N$ for $u_{-,\alpha}(r)$. Now we can calculate the rest part of the Hamiltonian from Eq. (5.34) as

$$M_{s,s'} = \int_0^\infty u_{+,i_0+s}(r)\Omega(r)u_{-,j_0+s'}(r)rdr.$$

Along with block-diagonal matrices $(H_+)_{s,s'} = v^2\epsilon_{+,i_0+s}\delta_{s,s'}/M$ and $(H_-)_{s,s'} = v^2\epsilon_{-,j_0+s}\delta_{s,s'}/M$, we can construct a $4N$-by-$4N$ matrix

$$H^{(l)}_{\text{eff,proj}} = \begin{pmatrix} H_+ & M \\ M^\dagger & H_- \end{pmatrix}, \tag{5.57}$$

and we can diagonalize this matrix to obtain the low-energy spectrum and wavefunctions.

5.10 Two-qubit Operation of Floquet Vortex State Qubits

For the separation d between the two vortices, the Hamiltonian regarding the two modes used for the qubit can be written as

$$\begin{aligned} H_{\text{d.v.}}(d) &= H_{\text{on}} + H_{\text{hop}}(d), \\ H_{\text{on}} &= \sum_{\text{P=L,R}} \left[\sum_{s=0,1} E_{n,l_0+s} c^\dagger_{s,\text{P}} c_{s,\text{P}} + U c^\dagger_{0,\text{P}} c_{0,\text{P}} c^\dagger_{1,\text{P}} c_{1,\text{P}} \right], \\ H_{\text{hop}}(d) &= \sum_{s=0,1} J_s(d) \left(c^\dagger_{s,\text{R}} c_{s,\text{L}} + \text{H.c.} \right), \end{aligned} \tag{5.58}$$

where $c^{\dagger}_{s,P}$ creates an electron on the left (P=L) or the right (P=R) vortex at the mode with pseudo-OAM $l_0 + s$. On-site interaction energy U is determined by the Coulomb repulsion between the two modes used for the qubit. While $J_0(d)$ and $J_1(d)$ are not strictly identical, we may regard them equally in practice since the amplitude of the tail part of the radial wavefunction is determined mostly by the radial profile of the beam rather than the pseudo-OAM. so, we set $J_{s=0,1}(d) = J(d)$ from now on. $H_{\rm hop}(d)$ in Eq. (5.58) can send a state to the outside of the two-qubit space, but such leakage is energetically unfavorable due to the on-site interaction energy U. Then the effective Hamiltonian in the two-qubit space can be obtained through the Schrieffer-Wolff transformation in the regime of $J(d) \ll U$. If we denote the projection operator onto the two-qubit space as P_2, the effective Hamiltonian can be written as

$$\begin{aligned} H_{\text{2-qubit}}(d) &= H_{\rm on}P_2 \\ &\quad + \frac{1}{2}\sum_{i,j,k}\left(\frac{\langle i|H_{\rm hop}|k\rangle\langle k|H_{\rm hop}|j\rangle}{\langle i|H_{\rm on}|i\rangle - \langle k|H_{\rm on}|k\rangle} + \frac{\langle i|H_{\rm hop}|k\rangle\langle k|H_{\rm hop}|j\rangle}{\langle j|H_{\rm on}|j\rangle - \langle k|H_{\rm on}|k\rangle}\right) P_2|i\rangle\langle j|P_2 \\ &= \frac{J(d)^2}{U}S + (E_{l_0} + E_{l_0+1})P_2, \\ S &= |01\rangle\langle 01| + |10\rangle\langle 10| + (|01\rangle\langle 10| + \text{H.c.})\,. \end{aligned} \tag{5.59}$$

For simplicity, we can drop the diagonal term $(E_{l_0} + E_{l_0+1})P_2$. Now, let us consider a dynamic sequence that approaches and then separtes two vortices, $d(t)$. The

time-evolution of this process is given by

$$\begin{aligned} U &= \exp\left[-i\int H_{\text{2-qubit}}(d(t))dt\right] \\ &= I\otimes I + \left(\frac{\exp[-iU^{-1}\int J(d(t))^2dt]-1}{2}\right)S \\ &= \begin{pmatrix} 1 & 0 & 0 & 0 \\ 0 & \frac{\exp(-i\Theta)+1}{2} & \frac{\exp(-i\Theta)-1}{2} & 0 \\ 0 & \frac{\exp(-i\Theta)-1}{2} & \frac{\exp(-i\Theta)+1}{2} & 0 \\ 0 & 0 & 0 & 1 \end{pmatrix}, \end{aligned} \tag{5.60}$$

where the matrix in the last row is written in computational basis $\{|00\rangle, |01\rangle, |10\rangle, |11\rangle\}$ and $\Theta = U^{-1}\int J(d(t))^2dt$. Here, I is an identity operation on a single qubit. Now, by controlling the dynamic sequence in a way that $e^{-i\Theta} = i$, we obtain

$$\begin{aligned} U &= \begin{pmatrix} 1 & 0 & 0 & 0 \\ 0 & \frac{1+i}{2} & -\frac{1-i}{2} & 0 \\ 0 & -\frac{1-i}{2} & \frac{1+i}{2} & 0 \\ 0 & 0 & 0 & 1 \end{pmatrix} \\ &= (I\otimes\sigma_z)\sqrt{\text{SWAP}}(I\otimes\sigma_z) \\ &= (\sigma_z\otimes I)\sqrt{\text{SWAP}}(\sigma_z\otimes I). \end{aligned} \tag{5.61}$$

5.11 Discussion and outlook

The most important challenge in using periodic driving in condensed matter systems are the heating effects. However, recently there have been several

theoretical proposals to restrain such destructive effects by using bath engineering techniques [197–199, 257–262]. In particular for Floquet topological insulators (FTI) [188] created by irradiating light to semiconductors as in our proposal, it has been demonstrated that in the weak-drive limit and in the presence of a phononic heat bath, heating effects produced by electron-electron and electron-phonon interactions can be suppressed provided that the bath-induced relaxation rates are sufficiently large [199]. For such baths key features of FTIs such as the existence of protected edge states can be preserved in the steady state which can make our proposal also stable in the steady state. Also, recent experiments [190,246] on the irradiated 2D material also provide another evidence that quantum states engineered by periodic driving on condensed matter systems can be stabilized in the lab.

While vortex states can also be engineered in cold atoms [226–230], there are several advantages to engineer them in electronic systems. One main advantage is the possibility of creating and manipulating multiple vortex states more conveniently, as demonstrated in the aforementioned qubit manipulation. While this is in principle possible in BEC systems too [263], controlling the transition of numerous atoms can be more challenging than manipulating a single electron. Also, our Floquet vortex state is spin-independent unlike the cold atom systems with spin-orbit-angular-momentum coupling [229, 230, 264–267], and this spin degrees of freedom can provide extra knobs for state engineering such as the Zeeman field.

To further elaborate the scheme for the quantum information processing, it would be interesting to study the possible measurement protocols for the OAM of the Floquet vortex states. One potential candidate for such protocol is through the

measurement of optical Hall conductivity, which might have different responses on the states with different OAM. Also, since our system has multiple non-linearly-dispersed Floquet vortex states, the extension to the qudit system is a natural topic for future study. While we briefly examined the possibility of such vortex state as a qubit, there are a lot of unanswered questions such as the heating, decoherence, and sensing in this platform. While we treated the vortex state of a single electron, it would be interesting to study how the presence of Coulomb interactions can change the vortex state structure or even help to create exotic many-body states. Another interesting direction is to investigate lattices of optical vortices and other field patterns such as electromagnetic skyrmions [268]. It would be also interesting to investigate how our approach can help to control optical properties of materials like van der Waals layered magnetic insulators.

Chapter 6: Discussion and Outlook

In this dissertation, we have investigated several schemes to engineer topological quantum states of matter with spatially patterned light. In this chapter, We compare ultracold atom schemes with each other and highlight their advantages and disadvantages. We also suggest some ideas to further develop the schemes.

The closed surface construction in Chapter 2 and the open boundary surface construction in Chapter 3 have different advantages. The closed surface construction can avoid unwanted effects of the boundary. For example, the measurement of ground state degeneracy of the Laughlin states via spectral flow in Chapter 2 is only possible in the intermediate-sized systems since it is a finite size effect. If one creates a system of such size with an open boundary, the effect of the boundary would ruin the desired physics in the bulk. On the other hand, the open boundary surface construction has the same orientation in both layers. This implements orientation-sensitive states easier compared to the closed surface construction where the two layers have the opposite orientation. For example, the FQH Hamiltonian could be built with far fewer laser beams in Chapter 3 since the same set of laser beams worked for both layers.

Schemes in Chapter 2 and Chapter 3 not only differ in the existence of bound-

ary but also differ in their methods to implement the bilayer structure. The real space implementation in Chapter 2 does not require an external magnetic field as well as laser-assisted tunnelings which have dangers to heat up the system. On the other hand, the spin-dependent implementation in Chapter 3 has better control over the interlayer tunneling and can easily image each layer separately. Also, the spin-dependent implementation does not have to maintain the intensity profile in the perpendicular direction. This can give better resolution and control for the beam pattern.

	Closed surface	Open boundary surface
Boundary effect	No	Yes
Orientation of layers	Opposite	Identical

Table 6.1: Comparison of the closed surface construction and the open boundary surface construction.

	Real space	Spin-dependent
Need an external magnetic field	No	Yes
Need laser-assisted tunneling	No	Yes
Interlayer tunneling control	More difficult	Easier
Single layer imaging	More difficult	Easier
Uniform intensity in perpendicular direction	Required	Not required

Table 6.2: Comparison of bilayer implementation schemes.

Different advantages of each construction and implementation schemes discussed so far are summarized in Table 6.1 and Table 6.2. Based on these characteristics, one may mix and match different construction and implementation schemes that fit best with the goal of the experiment. For example, if one is not interested

in achieving the quantum Hall states but wishes to control the interlayer tunneling better, one may try the closed surface construction with the spin-dependent implementation of the bilayer structure.

As we discussed in Chapters 4 and 5, it is intriguing to see how such optical patterning can be also implemented in solid-state systems. The optical imprinting scheme in Chapter 4 not only provides a wide variety of spatial patterns on the 2D materials but also can provide dynamically changing patterns as well. For example, the topological phase transitions investigated in Chapter 4 can be demonstrated in real-time. Dynamically changing spatial patterns may even implement the spacetime crystals [87, 88].

Bibliography

[1] K. v. Klitzing, G. Dorda, and M. Pepper. New method for high-accuracy determination of the fine-structure constant based on quantized hall resistance. *Phys. Rev. Lett.*, 45:494–497, Aug 1980.

[2] Evgenii Mikhailovich Lifshitz and Lev Petrovich Pitaevskii. *Statistical physics: theory of the condensed state*, volume 9. Elsevier, 2013.

[3] Xiao-Gang Wen. Topological orders and edge excitations in fractional quantum hall states. *Advances in Physics*, 44(5):405–473, 1995.

[4] W Poirier and F Schopfer. Resistance metrology based on the quantum hall effect. *The European Physical Journal Special Topics*, 172(1):207–245, 2009.

[5] Chetan Nayak, Steven H. Simon, Ady Stern, Michael Freedman, and Sankar Das Sarma. Non-abelian anyons and topological quantum computation. *Rev. Mod. Phys.*, 80:1083–1159, Sep 2008.

[6] Sankar Das Sarma, Michael Freedman, and Chetan Nayak. Majorana zero modes and topological quantum computation. *npj Quantum Information*, 1(1):1–13, 2015.

[7] M. Aidelsburger, M. Atala, M. Lohse, J. T. Barreiro, B. Paredes, and I. Bloch. Realization of the hofstadter hamiltonian with ultracold atoms in optical lattices. *Phys. Rev. Lett.*, 111:185301, Oct 2013.

[8] Hirokazu Miyake, Georgios A. Siviloglou, Colin J. Kennedy, William Cody Burton, and Wolfgang Ketterle. Realizing the harper hamiltonian with laser-assisted tunneling in optical lattices. *Phys. Rev. Lett.*, 111:185302, Oct 2013.

[9] Monika Aidelsburger, Michael Lohse, Christian Schweizer, Marcos Atala, Julio T Barreiro, Sylvain Nascimbène, NR Cooper, Immanuel Bloch, and Nathan Goldman. Measuring the chern number of hofstadter bands with ultracold bosonic atoms. *Nature Physics*, 11(2):162–166, 2015.

[10] B. K. Stuhl, H.-I. Lu, L. M. Aycock, D. Genkina, and I. B. Spielman. Visualizing edge states with an atomic bose gas in the quantum hall regime. *Science*, 349(6255):1514–1518, 2015.

[11] Pedram Roushan, C Neill, Yu Chen, M Kolodrubetz, C Quintana, N Leung, M Fang, R Barends, B Campbell, Z Chen, et al. Observation of topological transitions in interacting quantum circuits. *Nature*, 515(7526):241–244, 2014.

[12] E. Flurin, V. V. Ramasesh, S. Hacohen-Gourgy, L. S. Martin, N. Y. Yao, and I. Siddiqi. Observing topological invariants using quantum walks in superconducting circuits. *Phys. Rev. X*, 7:031023, Aug 2017.

[13] W. Cai, J. Han, Feng Mei, Y. Xu, Y. Ma, X. Li, H. Wang, Y. P. Song, Zheng-Yuan Xue, Zhang-qi Yin, Suotang Jia, and Luyan Sun. Observation of topological magnon insulator states in a superconducting circuit. *Phys. Rev. Lett.*, 123:080501, Aug 2019.

[14] KJ Satzinger, Y Liu, A Smith, C Knapp, M Newman, C Jones, Z Chen, C Quintana, X Mi, A Dunsworth, et al. Realizing topologically ordered states on a quantum processor. *arXiv preprint arXiv:2104.01180*, 2021.

[15] Mikael C Rechtsman, Julia M Zeuner, Yonatan Plotnik, Yaakov Lumer, Daniel Podolsky, Felix Dreisow, Stefan Nolte, Mordechai Segev, and Alexander Szameit. Photonic floquet topological insulators. *Nature*, 496(7444):196, 2013.

[16] Mohammad Hafezi, Eugene A Demler, Mikhail D Lukin, and Jacob M Taylor. Robust optical delay lines with topological protection. *Nature Physics*, 7(11):907, 2011.

[17] Mohammad Hafezi, S Mittal, J Fan, A Migdall, and JM Taylor. Imaging topological edge states in silicon photonics. *Nature Photonics*, 7(12):1001–1005, 2013.

[18] Sunil Mittal, Sriram Ganeshan, Jingyun Fan, Abolhassan Vaezi, and Mohammad Hafezi. Measurement of topological invariants in a 2d photonic system. *Nature Photonics*, 10(3):180–183, 2016.

[19] Sunil Mittal, Venkata Vikram Orre, Guanyu Zhu, Maxim A Gorlach, Alexander Poddubny, and Mohammad Hafezi. Photonic quadrupole topological phases. *Nature Photonics*, 13(10):692–696, 2019.

[20] Sabyasachi Barik, Aziz Karasahin, Christopher Flower, Tao Cai, Hirokazu Miyake, Wade DeGottardi, Mohammad Hafezi, and Edo Waks. A topological quantum optics interface. *Science*, 359(6376):666–668, 2018.

[21] Sabyasachi Barik, Hirokazu Miyake, Wade DeGottardi, Edo Waks, and Mohammad Hafezi. Two-dimensionally confined topological edge states in photonic crystals. 18(11):113013, nov 2016.

[22] Haitan Xu, David Mason, Luyao Jiang, and JGE Harris. Topological energy transfer in an optomechanical system with exceptional points. *Nature*, 537(7618):80–83, 2016.

[23] Hengjiang Ren, Tirth Shah, Hannes Pfeifer, Christian Brendel, Vittorio Peano, Florian Marquardt, and Oskar Painter. Topological phonon transport in an optomechanical system. In *CLEO: Science and Innovations*, pages STu2H–3. Optical Society of America, 2021.

[24] M Eric Tai, Alexander Lukin, Matthew Rispoli, Robert Schittko, Tim Menke, Dan Borgnia, Philipp M Preiss, Fabian Grusdt, Adam M Kaufman, and Markus Greiner. Microscopy of the interacting harper–hofstadter model in the two-body limit. *Nature*, 546(7659):519, 2017.

[25] Alexander Lukin, Matthew Rispoli, Robert Schittko, M Eric Tai, Adam M Kaufman, Soonwon Choi, Vedika Khemani, Julian Léonard, and Markus Greiner. Probing entanglement in a many-body–localized system. *Science*, 364(6437):256–260, 2019.

[26] Christie S Chiu, Geoffrey Ji, Annabelle Bohrdt, Muqing Xu, Michael Knap, Eugene Demler, Fabian Grusdt, Markus Greiner, and Daniel Greif. String patterns in the doped hubbard model. *Science*, 365(6450):251–256, 2019.

[27] Jacob P. Covey, Ivaylo S. Madjarov, Alexandre Cooper, and Manuel Endres. 2000-times repeated imaging of strontium atoms in clock-magic tweezer arrays. *Phys. Rev. Lett.*, 122:173201, May 2019.

[28] Ivaylo S. Madjarov, Alexandre Cooper, Adam L. Shaw, Jacob P. Covey, Vladimir Schkolnik, Tai Hyun Yoon, Jason R. Williams, and Manuel Endres. An atomic-array optical clock with single-atom readout. *Phys. Rev. X*, 9:041052, Dec 2019.

[29] B. I. Halperin. Quantized hall conductance, current-carrying edge states, and the existence of extended states in a two-dimensional disordered potential. *Phys. Rev. B*, 25:2185–2190, Feb 1982.

[30] R. B. Laughlin. Quantized hall conductivity in two dimensions. *Phys. Rev. B*, 23:5632–5633, May 1981.

[31] D. J. Thouless, M. Kohmoto, M. P. Nightingale, and M. den Nijs. Quantized hall conductance in a two-dimensional periodic potential. *Phys. Rev. Lett.*, 49:405–408, Aug 1982.

[32] B. Andrei Bernevig, Taylor L. Hughes, and Shou-Cheng Zhang. Quantum spin hall effect and topological phase transition in hgte quantum wells. *Science*, 314(5806):1757–1761, 2006.

[33] Markus König, Steffen Wiedmann, Christoph Brüne, Andreas Roth, Hartmut Buhmann, Laurens W. Molenkamp, Xiao-Liang Qi, and Shou-Cheng Zhang. Quantum spin hall insulator state in hgte quantum wells. *Science*, 318(5851):766–770, 2007.

[34] Chaoxing Liu, Taylor L. Hughes, Xiao-Liang Qi, Kang Wang, and Shou-Cheng Zhang. Quantum spin hall effect in inverted type-ii semiconductors. *Phys. Rev. Lett.*, 100:236601, Jun 2008.

[35] Ivan Knez, Rui-Rui Du, and Gerard Sullivan. Evidence for helical edge modes in inverted InAs/GaSb quantum wells. *Phys. Rev. Lett.*, 107:136603, Sep 2011.

[36] David Hsieh, Dong Qian, Lewis Wray, YuQi Xia, Yew San Hor, Robert Joseph Cava, and M Zahid Hasan. A topological dirac insulator in a quantum spin hall phase. *Nature*, 452(7190):970, 2008.

[37] Yuqi Xia, Dong Qian, David Hsieh, L Wray, Arijeet Pal, Hsin Lin, Arun Bansil, DHYS Grauer, Yew San Hor, Robert Joseph Cava, et al. Observation of a large-gap topological-insulator class with a single dirac cone on the surface. *Nature physics*, 5(6):398–402, 2009.

[38] David Hsieh, Yuqi Xia, Dong Qian, L Wray, JH Dil, Fedorov Meier, J Osterwalder, L Patthey, JG Checkelsky, Nai Phuan Ong, et al. A tunable topological insulator in the spin helical dirac transport regime. *Nature*, 460(7259):1101–1105, 2009.

[39] Jason Alicea. New directions in the pursuit of majorana fermions in solid state systems. *Reports on Progress in Physics*, 75(7):076501, jun 2012.

[40] T D Stanescu and S Tewari. Majorana fermions in semiconductor nanowires: fundamentals, modeling, and experiment. *Journal of Physics: Condensed Matter*, 25(23):233201, may 2013.

[41] Roman M. Lutchyn, Jay D. Sau, and S. Das Sarma. Majorana fermions and a topological phase transition in semiconductor-superconductor heterostructures. *Phys. Rev. Lett.*, 105:077001, Aug 2010.

[42] Yuval Oreg, Gil Refael, and Felix von Oppen. Helical liquids and majorana bound states in quantum wires. *Phys. Rev. Lett.*, 105:177002, Oct 2010.

[43] V. Mourik, K. Zuo, S. M. Frolov, S. R. Plissard, E. P. A. M. Bakkers, and L. P. Kouwenhoven. Signatures of majorana fermions in hybrid superconductor-semiconductor nanowire devices. *Science*, 336(6084):1003–1007, 2012.

[44] S. Murakawa, Y. Tamura, Y. Wada, M. Wasai, M. Saitoh, Y. Aoki, R. Nomura, Y. Okuda, Y. Nagato, M. Yamamoto, S. Higashitani, and K. Nagai. New anomaly in the transverse acoustic impedance of superfluid ^{3}He$-\mathbf{B}$ with a wall coated by several layers of ^{4}He. *Phys. Rev. Lett.*, 103:155301, Oct 2009.

[45] P. M. R. Brydon, Andreas P. Schnyder, and Carsten Timm. Topologically protected flat zero-energy surface bands in noncentrosymmetric superconductors. *Phys. Rev. B*, 84:020501, Jul 2011.

[46] Andreas P. Schnyder and Shinsei Ryu. Topological phases and surface flat bands in superconductors without inversion symmetry. *Phys. Rev. B*, 84:060504, Aug 2011.

[47] Zhijun Wang, Yan Sun, Xing-Qiu Chen, Cesare Franchini, Gang Xu, Hongming Weng, Xi Dai, and Zhong Fang. Dirac semimetal and topological phase transitions in A_3bi (a = Na, k, rb). *Phys. Rev. B*, 85:195320, May 2012.

[48] Zhijun Wang, Hongming Weng, Quansheng Wu, Xi Dai, and Zhong Fang. Three-dimensional dirac semimetal and quantum transport in cd_3as_2. *Phys. Rev. B*, 88:125427, Sep 2013.

[49] Xiangang Wan, Ari M. Turner, Ashvin Vishwanath, and Sergey Y. Savrasov. Topological semimetal and fermi-arc surface states in the electronic structure of pyrochlore iridates. *Phys. Rev. B*, 83:205101, May 2011.

[50] Ching-Kai Chiu, Jeffrey C. Y. Teo, Andreas P. Schnyder, and Shinsei Ryu. Classification of topological quantum matter with symmetries. *Rev. Mod. Phys.*, 88:035005, Aug 2016.

[51] Xie Chen, Zheng-Cheng Gu, and Xiao-Gang Wen. Local unitary transformation, long-range quantum entanglement, wave function renormalization, and topological order. *Phys. Rev. B*, 82:155138, Oct 2010.

[52] Andreas P. Schnyder, Shinsei Ryu, Akira Furusaki, and Andreas W. W. Ludwig. Classification of topological insulators and superconductors in three spatial dimensions. *Phys. Rev. B*, 78:195125, Nov 2008.

[53] Alexei Kitaev. Periodic table for topological insulators and superconductors. *AIP Conference Proceedings*, 1134(1):22–30, 2009.

[54] Shinsei Ryu, Andreas P Schnyder, Akira Furusaki, and Andreas W W Ludwig. Topological insulators and superconductors: tenfold way and dimensional hierarchy. *New Journal of Physics*, 12(6):065010, jun 2010.

[55] Ching-Kai Chiu, Hong Yao, and Shinsei Ryu. Classification of topological insulators and superconductors in the presence of reflection symmetry. *Phys. Rev. B*, 88:075142, Aug 2013.

[56] Takahiro Morimoto and Akira Furusaki. Topological classification with additional symmetries from clifford algebras. *Phys. Rev. B*, 88:125129, Sep 2013.

[57] Liang Fu. Topological crystalline insulators. *Phys. Rev. Lett.*, 106:106802, Mar 2011.

[58] Chen Fang, Matthew J. Gilbert, and B. Andrei Bernevig. Bulk topological invariants in noninteracting point group symmetric insulators. *Phys. Rev. B*, 86:115112, Sep 2012.

[59] A. Alexandradinata, Chen Fang, Matthew J. Gilbert, and B. Andrei Bernevig. Spin-orbit-free topological insulators without time-reversal symmetry. *Phys. Rev. Lett.*, 113:116403, Sep 2014.

[60] Liang Fu and C. L. Kane. Topological insulators with inversion symmetry. *Phys. Rev. B*, 76:045302, Jul 2007.

[61] Yuan-Ming Lu and Dung-Hai Lee. Inversion symmetry protected topological insulators and superconductors. *arXiv preprint arXiv:1403.5558*, 2014.

[62] Liang Fu, C. L. Kane, and E. J. Mele. Topological insulators in three dimensions. *Phys. Rev. Lett.*, 98:106803, Mar 2007.

[63] Ying Ran, Yi Zhang, and Ashvin Vishwanath. One-dimensional topologically protected modes in topological insulators with lattice dislocations. *Nature Physics*, 5(4):298–303, 2009.

[64] R. B. Laughlin. Anomalous quantum hall effect: An incompressible quantum fluid with fractionally charged excitations. *Phys. Rev. Lett.*, 50:1395–1398, May 1983.

[65] F. D. M. Haldane. Fractional quantization of the hall effect: A hierarchy of incompressible quantum fluid states. *Phys. Rev. Lett.*, 51:605–608, Aug 1983.

[66] Alexei Kitaev and John Preskill. Topological entanglement entropy. *Phys. Rev. Lett.*, 96:110404, Mar 2006.

[67] Michael Levin and Xiao-Gang Wen. Detecting topological order in a ground state wave function. *Phys. Rev. Lett.*, 96:110405, Mar 2006.

[68] F. D. M. Haldane and E. H. Rezayi. Periodic laughlin-jastrow wave functions for the fractional quantized hall effect. *Phys. Rev. B*, 31:2529–2531, Feb 1985.

[69] V. Kalmeyer and R. B. Laughlin. Equivalence of the resonating-valence-bond and fractional quantum hall states. *Phys. Rev. Lett.*, 59:2095–2098, Nov 1987.

[70] R.B Laughlin. Spin hamiltonian for which quantum hall wavefunction is exact. *Annals of Physics*, 191(1):163–202, 1989.

[71] X. G. Wen. Vacuum degeneracy of chiral spin states in compactified space. *Phys. Rev. B*, 40:7387–7390, Oct 1989.

[72] X. G. Wen and Q. Niu. Ground-state degeneracy of the fractional quantum hall states in the presence of a random potential and on high-genus riemann surfaces. *Phys. Rev. B*, 41:9377–9396, May 1990.

[73] X.-G. Wen and A. Zee. Topological degeneracy of quantum hall fluids. *Phys. Rev. B*, 58:15717–15728, Dec 1998.

[74] X. G. Wen, Frank Wilczek, and A. Zee. Chiral spin states and superconductivity. *Phys. Rev. B*, 39:11413–11423, Jun 1989.

[75] Daniel Arovas, J. R. Schrieffer, and Frank Wilczek. Fractional statistics and the quantum hall effect. *Phys. Rev. Lett.*, 53:722–723, Aug 1984.

[76] Alexei Kitaev. Anyons in an exactly solved model and beyond. *Annals of Physics*, 321(1):2–111, 2006. January Special Issue.

[77] Hideo Sambe. Steady states and quasienergies of a quantum-mechanical system in an oscillating field. *Phys. Rev. A*, 7:2203–2213, Jun 1973.

[78] A. Gómez-León and G. Platero. Floquet-bloch theory and topology in periodically driven lattices. *Phys. Rev. Lett.*, 110:200403, May 2013.

[79] N. Goldman and J. Dalibard. Periodically driven quantum systems: Effective hamiltonians and engineered gauge fields. *Phys. Rev. X*, 4:031027, Aug 2014.

[80] André Eckardt and Egidijus Anisimovas. High-frequency approximation for periodically driven quantum systems from a floquet-space perspective. *New journal of physics*, 17(9):093039, 2015.

[81] Takahiro Mikami, Sota Kitamura, Kenji Yasuda, Naoto Tsuji, Takashi Oka, and Hideo Aoki. Brillouin-wigner theory for high-frequency expansion in periodically driven systems: Application to floquet topological insulators. *Phys. Rev. B*, 93:144307, Apr 2016.

[82] G. Floquet. Sur les équations différentielles linéaires à coefficients périodiques. *Annales scientifiques de l'École Normale Supérieure*, 2e série, 12:47–88, 1883.

[83] Gregory H. Wannier. Wave functions and effective hamiltonian for bloch electrons in an electric field. *Phys. Rev.*, 117:432–439, Jan 1960.

[84] Markus Glück, Andrey R. Kolovsky, and Hans Jürgen Korsch. Wannier–stark resonances in optical and semiconductor superlattices. *Physics Reports*, 366(3):103–182, 2002.

[85] J. R. Schrieffer and P. A. Wolff. Relation between the anderson and kondo hamiltonians. *Phys. Rev.*, 149:491–492, Sep 1966.

[86] Sergey Bravyi, David P. DiVincenzo, and Daniel Loss. Schrieffer–wolff transformation for quantum many-body systems. *Annals of Physics*, 326(10):2793–2826, 2011.

[87] Shenglong Xu and Congjun Wu. Space-time crystal and space-time group. *Phys. Rev. Lett.*, 120:096401, Feb 2018.

[88] Qiang Gao and Qian Niu. Floquet-bloch oscillations and intraband zener tunneling in an oblique spacetime crystal. *Phys. Rev. Lett.*, 127:036401, Jul 2021.

[89] Yang Peng and Gil Refael. Floquet second-order topological insulators from nonsymmorphic space-time symmetries. *Phys. Rev. Lett.*, 123:016806, Jul 2019.

[90] Fenner Harper, Rahul Roy, Mark S. Rudner, and S.L. Sondhi. Topology and broken symmetry in floquet systems. *Annual Review of Condensed Matter Physics*, 11(1):345–368, 2020.

[91] N B Delone and Vladimir P Krainov. AC stark shift of atomic energy levels. 42(7):669–687, jul 1999.

[92] Oliver Morsch and Markus Oberthaler. Dynamics of bose-einstein condensates in optical lattices. *Rev. Mod. Phys.*, 78:179–215, Feb 2006.

[93] Immanuel Bloch, Jean Dalibard, and Wilhelm Zwerger. Many-body physics with ultracold gases. *Rev. Mod. Phys.*, 80:885–964, Jul 2008.

[94] Philip Zupancic, Philipp M. Preiss, Ruichao Ma, Alexander Lukin, M. Eric Tai, Matthew Rispoli, Rajibul Islam, and Markus Greiner. Ultra-precise holographic beam shaping for microscopic quantum control. *Opt. Express*, 24(13):13881–13893, Jun 2016.

[95] Stefan Kuhr. Quantum-gas microscopes: a new tool for cold-atom quantum simulators. *National Science Review*, 3(2):170–172, 04 2016.

[96] Kevin J. Mitchell, Sergey Turtaev, Miles J. Padgett, Tomáš Čižmár, and David B. Phillips. High-speed spatial control of the intensity, phase and polarisation of vector beams using a digital micro-mirror device. *Opt. Express*, 24(25):29269–29282, Dec 2016.

[97] Dongliang Gao, Weiqiang Ding, Manuel Nieto-Vesperinas, Xumin Ding, Mahdy Rahman, Tianhang Zhang, ChweeTeck Lim, and Cheng-Wei Qiu. Optical manipulation from the microscale to the nanoscale: fundamentals, advances and prospects. *Light: Science & Applications*, 6(9):e17039–e17039, 2017.

[98] Daniel Barredo, Sylvain de Léséleuc, Vincent Lienhard, Thierry Lahaye, and Antoine Browaeys. An atom-by-atom assembler of defect-free arbitrary two-dimensional atomic arrays. *Science*, 354(6315):1021–1023, 2016.

[99] Manuel Endres, Hannes Bernien, Alexander Keesling, Harry Levine, Eric R. Anschuetz, Alexandre Krajenbrink, Crystal Senko, Vladan Vuletic, Markus Greiner, and Mikhail D. Lukin. Atom-by-atom assembly of defect-free one-dimensional cold atom arrays. *Science*, 354(6315):1024–1027, 2016.

[100] Daniel Barredo, Vincent Lienhard, Sylvain De Leseleuc, Thierry Lahaye, and Antoine Browaeys. Synthetic three-dimensional atomic structures assembled atom by atom. *Nature*, 561(7721):79–82, 2018.

[101] D. Jaksch, C. Bruder, J. I. Cirac, C. W. Gardiner, and P. Zoller. Cold bosonic atoms in optical lattices. *Phys. Rev. Lett.*, 81:3108–3111, Oct 1998.

[102] Markus Greiner, Olaf Mandel, Tilman Esslinger, Theodor W Hänsch, and Immanuel Bloch. Quantum phase transition from a superfluid to a mott insulator in a gas of ultracold atoms. *Nature (London)*, 415(6867):39–44, 2002.

[103] Belén Paredes, Artur Widera, Valentin Murg, Olaf Mandel, Simon Fölling, Ignacio Cirac, Gora V Shlyapnikov, Theodor W Hänsch, and Immanuel Bloch. Tonks–girardeau gas of ultracold atoms in an optical lattice. *Nature (London)*, 429(6989):277–281, 2004.

[104] M Greiner, I Bloch, O Mandel, TW Hänsch, and T Esslinger. Bose–einstein condensates in 1d-and 2d optical lattices. *Appl. Phys. B: Lasers and Optics*, 73(8):769–772, 2001.

[105] Thilo Stöferle, Henning Moritz, Christian Schori, Michael Köhl, and Tilman Esslinger. Transition from a strongly interacting 1d superfluid to a mott insulator. *Phys. Rev. Lett.*, 92:130403, Mar 2004.

[106] I. B. Spielman, W. D. Phillips, and J. V. Porto. Mott-insulator transition in a two-dimensional atomic bose gas. *Phys. Rev. Lett.*, 98:080404, Feb 2007.

[107] C Becker, P Soltan-Panahi, J Kronjäger, S Dörscher, K Bongs, and K Sengstock. Ultracold quantum gases in triangular optical lattices. *New Journal of Physics*, 12(6):065025, jun 2010.

[108] Leticia Tarruell, Daniel Greif, Thomas Uehlinger, Gregor Jotzu, and Tilman Esslinger. Creating, moving and merging dirac points with a fermi gas in a tunable honeycomb lattice. *Nature (London)*, 483(7389):302–305, 2012.

[109] Gyu-Boong Jo, Jennie Guzman, Claire K. Thomas, Pavan Hosur, Ashvin Vishwanath, and Dan M. Stamper-Kurn. Ultracold atoms in a tunable optical kagome lattice. *Phys. Rev. Lett.*, 108:045305, Jan 2012.

[110] A. Ramanathan, K. C. Wright, S. R. Muniz, M. Zelan, W. T. Hill, C. J. Lobb, K. Helmerson, W. D. Phillips, and G. K. Campbell. Superflow in a toroidal bose-einstein condensate: An atom circuit with a tunable weak link. *Phys. Rev. Lett.*, 106:130401, Mar 2011.

[111] Mateusz Łącki, Hannes Pichler, Antoine Sterdyniak, Andreas Lyras, Vassilis E. Lembessis, Omar Al-Dossary, Jan Carl Budich, and Peter Zoller. Quantum hall physics with cold atoms in cylindrical optical lattices. *Phys. Rev. A*, 93:013604, Jan 2016.

[112] F. D. M. Haldane. Many-particle translational symmetries of two-dimensional electrons at rational landau-level filling. *Phys. Rev. Lett.*, 55:2095–2098, Nov 1985.

[113] A.Yu. Kitaev. Fault-tolerant quantum computation by anyons. *Annals of Physics*, 303(1):2–30, 2003.

[114] Xiao-Gang Wen. Quantum orders and symmetric spin liquids. *Phys. Rev. B*, 65:165113, Apr 2002.

[115] Vadim Kalmeyer and R. B. Laughlin. Theory of the spin liquid state of the heisenberg antiferromagnet. *Phys. Rev. B*, 39:11879–11899, Jun 1989.

[116] Octavi Boada, Alessio Celi, Javier Rodríguez-Laguna, José I Latorre, and Maciej Lewenstein. Quantum simulation of non-trivial topology. *New Journal of Physics*, 17(4):045007, apr 2015.

[117] Fabian Grusdt and Michael H"oning. Realization of fractional chern insulators in the thin-torus limit with ultracold bosons. *Phys. Rev. A*, 90:053623, Nov 2014.

[118] J. C. Budich, A. Elben, M. Łącki, A. Sterdyniak, M. A. Baranov, and P. Zoller. Coupled atomic wires in a synthetic magnetic field. *Phys. Rev. A*, 95:043632, Apr 2017.

[119] Nathan Schine, Michelle Chalupnik, Tankut Can, Andrey Gromov, and Jonathan Simon. Electromagnetic and gravitational responses of photonic landau levels. *Nature*, 565(7738):173–179, 2019.

[120] Rudolf Grimm, Matthias Weidemüller, and Yurii B. Ovchinnikov. Optical dipole traps for neutral atoms. volume 42 of *Advances In Atomic, Molecular, and Optical Physics*, pages 95–170. Academic Press, 2000.

[121] C. Ryu, M. F. Andersen, P. Cladé, Vasant Natarajan, K. Helmerson, and W. D. Phillips. Observation of persistent flow of a bose-einstein condensate in a toroidal trap. *Phys. Rev. Lett.*, 99:260401, Dec 2007.

[122] K. C. Wright, R. B. Blakestad, C. J. Lobb, W. D. Phillips, and G. K. Campbell. Threshold for creating excitations in a stirred superfluid ring. *Phys. Rev. A*, 88:063633, Dec 2013.

[123] Anthony J. Leggett. Bose-einstein condensation in the alkali gases: Some fundamental concepts. *Rev. Mod. Phys.*, 73:307–356, Apr 2001.

[124] Eugene P Gross. Structure of a quantized vortex in boson systems. *Nuovo Cimento*, 20(3):454–477, 1961.

[125] LP Pitaevskii. Vortex lines in an imperfect bose gas. *Sov. Phys. JETP*, 13(2):451–454, 1961.

[126] Weizhu Bao, Dieter Jaksch, and Peter A Markowich. Numerical solution of the gross–pitaevskii equation for bose–einstein condensation. *J. Comput. Phys.*, 187(1):318–342, 2003.

[127] Yasuhiro Hatsugai, Mahito Kohmoto, and Yong-Shi Wu. Anyons on a torus: Braid group, aharonov-bohm period, and numerical study. *Phys. Rev. B*, 43:10761–10768, May 1991.

[128] M. Hafezi, A. S. Sørensen, M. D. Lukin, and E. Demler. Characterization of topological states on a lattice with chern number. *Europhysics Letters (EPL)*, 81(1):10005, nov 2007.

[129] A. E. Siegman. *Lasers*. University Science Books, Mill Valley, CA, 1986.

[130] Carsten Robens, Stefan Brakhane, Wolfgang Alt, Felix Kleißler, Dieter Meschede, Geol Moon, Gautam Ramola, and Andrea Alberti. High numerical aperture (na = 0.92) objective lens for imaging and addressing of cold atoms. *Optics letters*, 42(6):1043–1046, 2017.

[131] Markus Glück, Andrey R Kolovsky, and Hans Jürgen Korsch. Wannier–stark resonances in optical and semiconductor superlattices. *Physics Reports*, 366(3):103–182, 2002.

[132] Douglas R. Hofstadter. Energy levels and wave functions of bloch electrons in rational and irrational magnetic fields. *Phys. Rev. B*, 14:2239–2249, Sep 1976.

[133] Emil J. Bergholtz and Anders Karlhede. Half-filled lowest landau level on a thin torus. *Phys. Rev. Lett.*, 94:026802, Jan 2005.

[134] Maissam Barkeshli and Michael Freedman. Modular transformations through sequences of topological charge projections. *Phys. Rev. B*, 94:165108, Oct 2016.

[135] Guanyu Zhu, Mohammad Hafezi, and Maissam Barkeshli. Quantum origami: Transversal gates for quantum computation and measurement of topological order. *Phys. Rev. Research*, 2:013285, Mar 2020.

[136] I. M. Georgescu, S. Ashhab, and Franco Nori. Quantum simulation. *Rev. Mod. Phys.*, 86:153–185, Mar 2014.

[137] N. R. Cooper, J. Dalibard, and I. B. Spielman. Topological bands for ultracold atoms. *Rev. Mod. Phys.*, 91:015005, Mar 2019.

[138] P. S. Jessen and I. H. Deutsch. Optical lattices. *Adv. At. Mol. Opt. Phys.*, 37(C):95–138, December 1996.

[139] K. I. Petsas, A. B. Coates, and G. Grynberg. Crystallography of optical lattices. *Phys. Rev. A*, 50:5173–5189, Dec 1994.

[140] S. Trotzky, P. Cheinet, S. Fölling, M. Feld, U. Schnorrberger, A. M. Rey, A. Polkovnikov, E. A. Demler, M. D. Lukin, and I. Bloch. Time-resolved observation and control of superexchange interactions with ultracold atoms in optical lattices. *Science*, 319(5861):295–299, 2008.

[141] P. Cheinet, S. Trotzky, M. Feld, U. Schnorrberger, M. Moreno-Cardoner, S. Fölling, and I. Bloch. Counting atoms using interaction blockade in an optical superlattice. *Phys. Rev. Lett.*, 101:090404, Aug 2008.

[142] Marco Anderlini, Patricia J Lee, Benjamin L Brown, Jennifer Sebby-Strabley, William D Phillips, and James V Porto. Controlled exchange interaction between pairs of neutral atoms in an optical lattice. *Nature*, 448(7152):452–456, 2007.

[143] B. K. Stuhl, H.-I. Lu, L. M. Aycock, D. Genkina, and I. B. Spielman. Visualizing edge states with an atomic bose gas in the quantum hall regime. *Science*, 349(6255):1514–1518, 2015.

[144] Hwanmun Kim, Guanyu Zhu, J. V. Porto, and Mohammad Hafezi. Optical lattice with torus topology. *Phys. Rev. Lett.*, 121:133002, Sep 2018.

[145] H. Bombin. Topological order with a twist: Ising anyons from an abelian model. *Phys. Rev. Lett.*, 105:030403, Jul 2010.

[146] Maissam Barkeshli and Xiao-Liang Qi. Topological nematic states and non-abelian lattice dislocations. *Phys. Rev. X*, 2:031013, Aug 2012.

[147] Maissam Barkeshli, Chao-Ming Jian, and Xiao-Liang Qi. Twist defects and projective non-abelian braiding statistics. *Phys. Rev. B*, 87:045130, Jan 2013.

[148] Maissam Barkeshli, Chao-Ming Jian, and Xiao-Liang Qi. Theory of defects in abelian topological states. *Phys. Rev. B*, 88:235103, Dec 2013.

[149] Maissam Barkeshli, Chao-Ming Jian, and Xiao-Liang Qi. Classification of topological defects in abelian topological states. *Phys. Rev. B*, 88:241103, Dec 2013.

[150] Gavin K. Brennen, Carlton M. Caves, Poul S. Jessen, and Ivan H. Deutsch. Quantum logic gates in optical lattices. *Phys. Rev. Lett.*, 82:1060–1063, Feb 1999.

[151] D. Jaksch, H.-J. Briegel, J. I. Cirac, C. W. Gardiner, and P. Zoller. Entanglement of atoms via cold controlled collisions. *Phys. Rev. Lett.*, 82:1975–1978, Mar 1999.

[152] Olaf Mandel, Markus Greiner, Artur Widera, Tim Rom, Theodor W. Hänsch, and Immanuel Bloch. Coherent transport of neutral atoms in spin-dependent optical lattice potentials. *Phys. Rev. Lett.*, 91:010407, Jul 2003.

[153] P. J. Lee, M. Anderlini, B. L. Brown, J. Sebby-Strabley, W. D. Phillips, and J. V. Porto. Sublattice addressing and spin-dependent motion of atoms in a double-well lattice. *Phys. Rev. Lett.*, 99:020402, Jul 2007.

[154] Parvis Soltan-Panahi, Julian Struck, Philipp Hauke, Andreas Bick, Wiebke Plenkers, Georg Meineke, Christoph Becker, Patrick Windpassinger, Maciej Lewenstein, and Klaus Sengstock. Multi-component quantum gases in spin-dependent hexagonal lattices. *Nat. Phys.*, 7(5):434–440, 2011.

[155] Antoine Browaeys and Thierry Lahaye. Many-body physics with individually controlled rydberg atoms. *Nature Physics*, pages 1–11, 2020.

[156] G. Gauthier, I. Lenton, N. McKay Parry, M. Baker, M. J. Davis, H. Rubinsztein-Dunlop, and T. W. Neely. Direct imaging of a digital-micromirror device for configurable microscopic optical potentials. *Optica*, 3(10):1136–1143, Oct 2016.

[157] Anton Mazurenko, Christie S Chiu, Geoffrey Ji, Maxwell F Parsons, Márton Kanász-Nagy, Richard Schmidt, Fabian Grusdt, Eugene Demler, Daniel Greif, and Markus Greiner. A cold-atom fermi–hubbard antiferromagnet. *Nature*, 545(7655):462–466, 2017.

[158] Anders S. Sørensen, Eugene Demler, and Mikhail D. Lukin. Fractional quantum hall states of atoms in optical lattices. *Phys. Rev. Lett.*, 94:086803, Mar 2005.

[159] Ze-Pei Cian, Hossein Dehghani, Andreas Elben, Benoît Vermersch, Guanyu Zhu, Maissam Barkeshli, Peter Zoller, and Mohammad Hafezi. Many-body chern number from statistical correlations of randomized measurements. *Phys. Rev. Lett.*, 126:050501, Feb 2021.

[160] Hossein Dehghani, Ze-Pei Cian, Mohammad Hafezi, and Maissam Barkeshli. Extraction of the many-body chern number from a single wave function. *Phys. Rev. B*, 103:075102, Feb 2021.

[161] C. Repellin, J. Léonard, and N. Goldman. Fractional chern insulators of few bosons in a box: Hall plateaus from center-of-mass drifts and density profiles. *Phys. Rev. A*, 102:063316, Dec 2020.

[162] Hannes Pichler, Guanyu Zhu, Alireza Seif, Peter Zoller, and Mohammad Hafezi. Measurement protocol for the entanglement spectrum of cold atoms. *Phys. Rev. X*, 6:041033, Nov 2016.

[163] L. Santos, G. V. Shlyapnikov, P. Zoller, and M. Lewenstein. Bose-einstein condensation in trapped dipolar gases. *Phys. Rev. Lett.*, 85:1791–1794, Aug 2000.

[164] Bryce Gadway and Bo Yan. Strongly interacting ultracold polar molecules. *Journal of Physics B: Atomic, Molecular and Optical Physics*, 49(15):152002, jun 2016.

[165] Bertrand I Halperin. Theory of the quantized hall conductance. *Helvetica Physica Acta*, 56(1-3):75–102, 1983.

[166] Nobuyuki Shima and Hideo Aoki. Electronic structure of super-honeycomb systems: A peculiar realization of semimetal/semiconductor classes and ferromagnetism. *Phys. Rev. Lett.*, 71:4389–4392, Dec 1993.

[167] R. Bistritzer and A. H. MacDonald. Moiré butterflies in twisted bilayer graphene. *Phys. Rev. B*, 84:035440, Jul 2011.

[168] Eric M Spanton, Alexander A Zibrov, Haoxin Zhou, Takashi Taniguchi, Kenji Watanabe, Michael P Zaletel, and Andrea F Young. Observation of fractional chern insulators in a van der waals heterostructure. *Science*, 360(6384):62–66, 2018.

[169] Rafi Bistritzer and Allan H MacDonald. Moiré bands in twisted double-layer graphene. *Proceedings of the National Academy of Sciences*, 108(30):12233–12237, 2011.

[170] J. M. B. Lopes dos Santos, N. M. R. Peres, and A. H. Castro Neto. Continuum model of the twisted graphene bilayer. *Phys. Rev. B*, 86:155449, Oct 2012.

[171] Grigory Tarnopolsky, Alex Jura Kruchkov, and Ashvin Vishwanath. Origin of magic angles in twisted bilayer graphene. *Phys. Rev. Lett.*, 122:106405, Mar 2019.

[172] Yuan Cao, Valla Fatemi, Shiang Fang, Kenji Watanabe, Takashi Taniguchi, Efthimios Kaxiras, and Pablo Jarillo-Herrero. Unconventional superconductivity in magic-angle graphene superlattices. *Nature*, 556(7699):43, 2018.

[173] Yuan Cao, Valla Fatemi, Ahmet Demir, Shiang Fang, Spencer L Tomarken, Jason Y Luo, Javier D Sanchez-Yamagishi, Kenji Watanabe, Takashi Taniguchi, Efthimios Kaxiras, Ray C Ashoori, and Pablo Jarillo-Herrero. Correlated insulator behaviour at half-filling in magic-angle graphene superlattices. *Nature*, 556(7699):80, 2018.

[174] Aaron L Sharpe, Eli J Fox, Arthur W Barnard, Joe Finney, Kenji Watanabe, Takashi Taniguchi, MA Kastner, and David Goldhaber-Gordon. Emergent ferromagnetism near three-quarters filling in twisted bilayer graphene. *Science*, 365(6453):605–608, 2019.

[175] Jianpeng Liu, Zhen Ma, Jinhua Gao, and Xi Dai. Quantum valley hall effect, orbital magnetism, and anomalous hall effect in twisted multilayer graphene systems. *Phys. Rev. X*, 9:031021, Aug 2019.

[176] Youngjoon Choi, Jeannette Kemmer, Yang Peng, Alex Thomson, Harpreet Arora, Robert Polski, Yiran Zhang, Hechen Ren, Jason Alicea, Gil Refael, Felix von Oppen, Keni Watanabe, Takashi Taniguchi, and Stevan Nadj-Perge. Electronic correlations in twisted bilayer graphene near the magic angle. *Nat. Phys.*, 15:1174–1180, 2019.

[177] Guorui Chen, Lili Jiang, Shuang Wu, Bosai Lyu, Hongyuan Li, Bheema Lingam Chittari, Kenji Watanabe, Takashi Taniguchi, Zhiwen Shi, Jeil Jung, Yuanbo Zhang, and Feng Wang. Evidence of a gate-tunable mott insulator in a trilayer graphene moiré superlattice. *Nature Physics*, 15(3):237, 2019.

[178] Hoi Chun Po, Liujun Zou, Ashvin Vishwanath, and T. Senthil. Origin of mott insulating behavior and superconductivity in twisted bilayer graphene. *Phys. Rev. X*, 8:031089, Sep 2018.

[179] Luis A. Gonzalez-Arraga, J. L. Lado, Francisco Guinea, and Pablo San-Jose. Electrically controllable magnetism in twisted bilayer graphene. *Phys. Rev. Lett.*, 119:107201, Sep 2017.

[180] Alex Thomson, Shubhayu Chatterjee, Subir Sachdev, and Mathias S. Scheurer. Triangular antiferromagnetism on the honeycomb lattice of twisted bilayer graphene. *Phys. Rev. B*, 98:075109, Aug 2018.

[181] A. O. Sboychakov, A. V. Rozhkov, A. L. Rakhmanov, and Franco Nori. Externally controlled magnetism and band gap in twisted bilayer graphene. *Phys. Rev. Lett.*, 120:266402, Jun 2018.

[182] Matthew Yankowitz, Shaowen Chen, Hryhoriy Polshyn, Yuxuan Zhang, K Watanabe, T Taniguchi, David Graf, Andrea F Young, and Cory R Dean. Tuning superconductivity in twisted bilayer graphene. *Science*, 363(6431):1059–1064, 2019.

[183] Fengcheng Wu, A. H. MacDonald, and Ivar Martin. Theory of phonon-mediated superconductivity in twisted bilayer graphene. *Phys. Rev. Lett.*, 121:257001, Dec 2018.

[184] Biao Lian, Zhijun Wang, and B. Andrei Bernevig. Twisted bilayer graphene: A phonon-driven superconductor. *Phys. Rev. Lett.*, 122:257002, Jun 2019.

[185] Furqan M Fazal and Steven M Block. Optical tweezers study life under tension. *Nature photonics*, 5(6):318, 2011.

[186] Takashi Oka and Hideo Aoki. Photovoltaic hall effect in graphene. *Phys. Rev. B*, 79:081406, Feb 2009.

[187] Takuya Kitagawa, Takashi Oka, Arne Brataas, Liang Fu, and Eugene Demler. Transport properties of nonequilibrium systems under the application of light:

Photoinduced quantum hall insulators without landau levels. *Phys. Rev. B*, 84:235108, Dec 2011.

[188] Netanel H Lindner, Gil Refael, and Victor Galitski. Floquet topological insulator in semiconductor quantum wells. *Nature Physics*, 7(6):490, 2011.

[189] Y. H. Wang, H. Steinberg, P. Jarillo-Herrero, and N. Gedik. Observation of floquet-bloch states on the surface of a topological insulator. *Science*, 342(6157):453–457, 2013.

[190] James W McIver, Benedikt Schulte, F-U Stein, Toru Matsuyama, Gregor Jotzu, Guido Meier, and Andrea Cavalleri. Light-induced anomalous hall effect in graphene. *Nature Physics*, 16(1):38–41, 2020.

[191] Gonzalo Usaj, P. M. Perez-Piskunow, L. E. F. Foa Torres, and C. A. Balseiro. Irradiated graphene as a tunable floquet topological insulator. *Phys. Rev. B*, 90:115423, Sep 2014.

[192] Gabriel E. Topp, Gregor Jotzu, James W. McIver, Lede Xian, Angel Rubio, and Michael A. Sentef. Topological floquet engineering of twisted bilayer graphene. *Phys. Rev. Research*, 1:023031, Sep 2019.

[193] Yantao Li, H. A. Fertig, and Babak Seradjeh. Floquet-engineered topological flat bands in irradiated twisted bilayer graphene. *Phys. Rev. Research*, 2:043275, Nov 2020.

[194] Or Katz, Gil Refael, and Netanel H. Lindner. Optically induced flat bands in twisted bilayer graphene. *Phys. Rev. B*, 102:155123, Oct 2020.

[195] J. Karch, C. Drexler, P. Olbrich, M. Fehrenbacher, M. Hirmer, M. M. Glazov, S. A. Tarasenko, E. L. Ivchenko, B. Birkner, J. Eroms, D. Weiss, R. Yakimova, S. Lara-Avila, S. Kubatkin, M. Ostler, T. Seyller, and S. D. Ganichev. Terahertz radiation driven chiral edge currents in graphene. *Phys. Rev. Lett.*, 107:276601, Dec 2011.

[196] A. H. Castro Neto, F. Guinea, N. M. R. Peres, K. S. Novoselov, and A. K. Geim. The electronic properties of graphene. *Rev. Mod. Phys.*, 81:109–162, Jan 2009.

[197] Hossein Dehghani, Takashi Oka, and Aditi Mitra. Dissipative floquet topological systems. *Phys. Rev. B*, 90:195429, Nov 2014.

[198] Hossein Dehghani, Takashi Oka, and Aditi Mitra. Out-of-equilibrium electrons and the hall conductance of a floquet topological insulator. *Phys. Rev. B*, 91:155422, Apr 2015.

[199] Karthik I. Seetharam, Charles-Edouard Bardyn, Netanel H. Lindner, Mark S. Rudner, and Gil Refael. Steady states of interacting floquet insulators. *Phys. Rev. B*, 99:014307, Jan 2019.

[200] Yaniv Tenenbaum Katan and Daniel Podolsky. Modulated floquet topological insulators. *Phys. Rev. Lett.*, 110:016802, Jan 2013.

[201] Yaniv Tenenbaum Katan and Daniel Podolsky. Generation and manipulation of localized modes in floquet topological insulators. *Phys. Rev. B*, 88:224106, Dec 2013.

[202] Skender Morina, Kevin Dini, Ivan V Iorsh, and Ivan A Shelykh. Optical trapping of electrons in graphene. *ACS Photonics*, 5(4):1171–1175, 2018.

[203] Mark S. Rudner, Netanel H. Lindner, Erez Berg, and Michael Levin. Anomalous edge states and the bulk-edge correspondence for periodically driven two-dimensional systems. *Phys. Rev. X*, 3:031005, Jul 2013.

[204] Takahiro Fukui, Yasuhiro Hatsugai, and Hiroshi Suzuki. Chern numbers in discretized brillouin zone: efficient method of computing (spin) hall conductances. *Journal of the Physical Society of Japan*, 74(6):1674–1677, 2005.

[205] T. Thonhauser, Davide Ceresoli, David Vanderbilt, and R. Resta. Orbital magnetization in periodic insulators. *Phys. Rev. Lett.*, 95:137205, Sep 2005.

[206] Di Xiao, Junren Shi, and Qian Niu. Berry phase correction to electron density of states in solids. *Phys. Rev. Lett.*, 95:137204, Sep 2005.

[207] Junren Shi, G. Vignale, Di Xiao, and Qian Niu. Quantum theory of orbital magnetization and its generalization to interacting systems. *Phys. Rev. Lett.*, 99:197202, Nov 2007.

[208] F. D. M. Haldane. Model for a quantum hall effect without landau levels: Condensed-matter realization of the "parity anomaly". *Phys. Rev. Lett.*, 61:2015–2018, Oct 1988.

[209] Jens Koch, Andrew A. Houck, Karyn Le Hur, and S. M. Girvin. Time-reversal-symmetry breaking in circuit-qed-based photon lattices. *Phys. Rev. A*, 82:043811, Oct 2010.

[210] Fahad Mahmood, Ching-Kit Chan, Zhanybek Alpichshev, Dillon Gardner, Young Lee, Patrick A Lee, and Nuh Gedik. Selective scattering between floquet–bloch and volkov states in a topological insulator. *Nature Physics*, 12(4):306, 2016.

[211] Michael Levin and Ady Stern. Fractional topological insulators. *Phys. Rev. Lett.*, 103:196803, Nov 2009.

[212] B. Swingle, M. Barkeshli, J. McGreevy, and T. Senthil. Correlated topological insulators and the fractional magnetoelectric effect. *Phys. Rev. B*, 83:195139, May 2011.

[213] Joseph Maciejko and Gregory A Fiete. Fractionalized topological insulators. *Nature Physics*, 11(5):385, 2015.

[214] Keita Kobayashi, Masahiko Okumura, Susumu Yamada, Masahiko Machida, and Hideo Aoki. Superconductivity in repulsively interacting fermions on a diamond chain: Flat-band-induced pairing. *Phys. Rev. B*, 94:214501, Dec 2016.

[215] Ivar Martin. Moiré superconductivity. *Annals of Physics*, 417:168118, 2020.

[216] Dmitry Panna, Nadav Landau, Liron Gantz, Leonid Rybak, Shai Tsesses, Guy Adler, Sebastian Brodbeck, Christian Schneider, Sven Höfling, and Alex Hayat. Ultrafast manipulation of a strongly-coupled light-matter system by a giant ac stark effect. *ACS Photonics*, 6(12):3076–3081, 2019.

[217] M. J. A. Schuetz, J. Knörzer, G. Giedke, L. M. K. Vandersypen, M. D. Lukin, and J. I. Cirac. Acoustic traps and lattices for electrons in semiconductors. *Phys. Rev. X*, 7:041019, Oct 2017.

[218] Changjun Min, Pei Wang, Chunchong Chen, Yan Deng, Yonghua Lu, Hai Ming, Tingyin Ning, Yueliang Zhou, and Guozhen Yang. All-optical switching in subwavelength metallic grating structure containing nonlinear optical materials. *Opt. Lett.*, 33(8):869–871, Apr 2008.

[219] Lars Onsager. Statistical hydrodynamics. *Nuovo Cim*, 6(2):279–287, 1949.

[220] RP Feynman. Chapter ii application of quantum mechanics to liquid helium. *Progress in Low Temperature Physics*, 1:17–53, 1955.

[221] Alexei A Abrikosov. On the magnetic properties of superconductors of the second group. *Sov. Phys. JETP*, 5:1174–1182, 1957.

[222] C. Caroli, P.G. De Gennes, and J. Matricon. Bound fermion states on a vortex line in a type ii superconductor. *Physics Letters*, 9(4):307–309, 1964.

[223] R. Jackiw and P. Rossi. Zero modes of the vortex-fermion system. *Nuclear Physics B*, 190(4):681–691, 1981.

[224] Grigory E Volovik. *The universe in a helium droplet*, volume 117. Oxford University Press on Demand, 2003.

[225] Russell J Donnelly. *Quantized vortices in helium II*, volume 2. Cambridge University Press, 1991.

[226] M. R. Matthews, B. P. Anderson, P. C. Haljan, D. S. Hall, C. E. Wieman, and E. A. Cornell. Vortices in a bose-einstein condensate. *Phys. Rev. Lett.*, 83:2498–2501, Sep 1999.

[227] K. W. Madison, F. Chevy, W. Wohlleben, and J. Dalibard. Vortex formation in a stirred bose-einstein condensate. *Phys. Rev. Lett.*, 84:806–809, Jan 2000.

[228] J. R. Abo-Shaeer, C. Raman, J. M. Vogels, and W. Ketterle. Observation of vortex lattices in bose-einstein condensates. *Science*, 292(5516):476–479, 2001.

[229] H.-R. Chen, K.-Y. Lin, P.-K. Chen, N.-C. Chiu, J.-B. Wang, C.-A. Chen, Panpan Huang, S.-K. Yip, Yuki Kawaguchi, and Y.-J. Lin. Spin–orbital-angular-momentum coupled bose-einstein condensates. *Phys. Rev. Lett.*, 121:113204, Sep 2018.

[230] Dongfang Zhang, Tianyou Gao, Peng Zou, Lingran Kong, Ruizong Li, Xing Shen, Xiao-Long Chen, Shi-Guo Peng, Mingsheng Zhan, Han Pu, and Kaijun Jiang. Ground-state phase diagram of a spin-orbital-angular-momentum coupled bose-einstein condensate. *Phys. Rev. Lett.*, 122:110402, Mar 2019.

[231] G. Blatter, M. V. Feigel'man, V. B. Geshkenbein, A. I. Larkin, and V. M. Vinokur. Vortices in high-temperature superconductors. *Rev. Mod. Phys.*, 66:1125–1388, Oct 1994.

[232] Tsofar Maniv, Vladimir Zhuravlev, Israel Vagner, and Peter Wyder. Vortex states and quantum magnetic oscillations in conventional type-ii superconductors. *Rev. Mod. Phys.*, 73:867–911, Nov 2001.

[233] A. Bogdanov and A. Hubert. Thermodynamically stable magnetic vortex states in magnetic crystals. *Journal of Magnetism and Magnetic Materials*, 138(3):255 – 269, 1994.

[234] Ulrich K Roessler, AN Bogdanov, and C Pfleiderer. Spontaneous skyrmion ground states in magnetic metals. *Nature*, 442(7104):797–801, 2006.

[235] Naoto Nagaosa and Yoshinori Tokura. Topological properties and dynamics of magnetic skyrmions. *Nature nanotechnology*, 8(12):899–911, 2013.

[236] J M Kosterlitz and D J Thouless. Ordering, metastability and phase transitions in two-dimensional systems. *Journal of Physics C: Solid State Physics*, 6(7):1181–1203, apr 1973.

[237] J M Kosterlitz. The critical properties of the two-dimensional xy model. *Journal of Physics C: Solid State Physics*, 7(6):1046–1060, mar 1974.

[238] P. A. Murthy, I. Boettcher, L. Bayha, M. Holzmann, D. Kedar, M. Neidig, M. G. Ries, A. N. Wenz, G. Zürn, and S. Jochim. Observation of the berezinskii-kosterlitz-thouless phase transition in an ultracold fermi gas. *Phys. Rev. Lett.*, 115:010401, Jun 2015.

[239] Daniel S. Fisher, Matthew P. A. Fisher, and David A. Huse. Thermal fluctuations, quenched disorder, phase transitions, and transport in type-ii superconductors. *Phys. Rev. B*, 43:130–159, Jan 1991.

[240] P. L. Gammel, L. F. Schneemeyer, J. V. Wasczak, and D. J. Bishop. Evidence from mechanical measurements for flux-lattice melting in single-crystal $yba_2cu_3o_7$ and $bi_{2.2}sr_2ca_{0.8}cu_2o_8$. *Phys. Rev. Lett.*, 61:1666–1669, Oct 1988.

[241] R. H. Koch, V. Foglietti, W. J. Gallagher, G. Koren, A. Gupta, and M. P. A. Fisher. Experimental evidence for vortex-glass superconductivity in y-ba-cu-o. *Phys. Rev. Lett.*, 63:1511–1514, Oct 1989.

[242] Michael Stone and Suk-Bum Chung. Fusion rules and vortices in $p_x + ip_y$ superconductors. *Phys. Rev. B*, 73:014505, Jan 2006.

[243] Kishore T. Kapale and Jonathan P. Dowling. Vortex phase qubit: Generating arbitrary, counterrotating, coherent superpositions in bose-einstein condensates via optical angular momentum beams. *Phys. Rev. Lett.*, 95:173601, Oct 2005.

[244] Paraj Titum, Erez Berg, Mark S. Rudner, Gil Refael, and Netanel H. Lindner. Anomalous floquet-anderson insulator as a nonadiabatic quantized charge pump. *Phys. Rev. X*, 6:021013, May 2016.

[245] Hwanmun Kim, Hossein Dehghani, Hideo Aoki, Ivar Martin, and Mohammad Hafezi. Optical imprinting of superlattices in two-dimensional materials. *Phys. Rev. Research*, 2:043004, Oct 2020.

[246] S. A. Sato, J. W. McIver, M. Nuske, P. Tang, G. Jotzu, B. Schulte, H. Hübener, U. De Giovannini, L. Mathey, M. A. Sentef, A. Cavalleri, and A. Rubio. Microscopic theory for the light-induced anomalous hall effect in graphene. *Phys. Rev. B*, 99:214302, Jun 2019.

[247] E. G. Novik, A. Pfeuffer-Jeschke, T. Jungwirth, V. Latussek, C. R. Becker, G. Landwehr, H. Buhmann, and L. W. Molenkamp. Band structure of semimagnetic $hg_{1-y}mn_yTe$ quantum wells. *Phys. Rev. B*, 72:035321, Jul 2005.

[248] GE Volovik. Vortex motion in fermi superfluids and the callan-harvey. *JETP Lett.*, 57(4):244, 1993.

[249] Yasuhiro Tada, Wenxing Nie, and Masaki Oshikawa. Orbital angular momentum and spectral flow in two-dimensional chiral superfluids. *Phys. Rev. Lett.*, 114:195301, May 2015.

[250] Teemu Ojanen. Ground-state angular momentum, spectral asymmetry, and topology in chiral superfluids and superconductors. *Phys. Rev. B*, 93:174505, May 2016.

[251] Abhinav Prem, Sergej Moroz, Victor Gurarie, and Leo Radzihovsky. Multiply quantized vortices in fermionic superfluids: Angular momentum, unpaired fermions, and spectral asymmetry. *Phys. Rev. Lett.*, 119:067003, Aug 2017.

[252] David P DiVincenzo, Dave Bacon, Julia Kempe, Guido Burkard, and K Birgitta Whaley. Universal quantum computation with the exchange interaction. *Nature*, 408(6810):339–342, 2000.

[253] Heng Fan, Vwani Roychowdhury, and Thomas Szkopek. Optimal two-qubit quantum circuits using exchange interactions. *Phys. Rev. A*, 72:052323, Nov 2005.

[254] Daniel Loss and David P. DiVincenzo. Quantum computation with quantum dots. *Phys. Rev. A*, 57:120–126, Jan 1998.

[255] Bruce E Kane. A silicon-based nuclear spin quantum computer. *nature*, 393(6681):133–137, 1998.

[256] Rutger Vrijen, Eli Yablonovitch, Kang Wang, Hong Wen Jiang, Alex Balandin, Vwani Roychowdhury, Tal Mor, and David DiVincenzo. Electron-spin-resonance transistors for quantum computing in silicon-germanium heterostructures. *Phys. Rev. A*, 62:012306, Jun 2000.

[257] Iliya Esin, Mark S. Rudner, Gil Refael, and Netanel H. Lindner. Quantized transport and steady states of floquet topological insulators. *Phys. Rev. B*, 97:245401, Jun 2018.

[258] Thomas Iadecola and Claudio Chamon. Floquet systems coupled to particle reservoirs. *Phys. Rev. B*, 91:184301, May 2015.

[259] Tatsuhiko Shirai, Takashi Mori, and Seiji Miyashita. Condition for emergence of the floquet-gibbs state in periodically driven open systems. *Phys. Rev. E*, 91:030101, Mar 2015.

[260] Hossein Dehghani and Aditi Mitra. Optical hall conductivity of a floquet topological insulator. *Phys. Rev. B*, 92:165111, Oct 2015.

[261] Hossein Dehghani and Aditi Mitra. Floquet topological systems in the vicinity of band crossings: Reservoir-induced coherence and steady-state entropy production. *Phys. Rev. B*, 93:245416, Jun 2016.

[262] Tomotaka Kuwahara, Takashi Mori, and Keiji Saito. Floquet-magnus theory and generic transient dynamics in periodically driven many-body quantum systems. *Annals of Physics*, 367:96–124, 2016.

[263] M. F. Andersen, C. Ryu, Pierre Cladé, Vasant Natarajan, A. Vaziri, K. Helmerson, and W. D. Phillips. Quantized rotation of atoms from photons with orbital angular momentum. *Phys. Rev. Lett.*, 97:170406, Oct 2006.

[264] Michael DeMarco and Han Pu. Angular spin-orbit coupling in cold atoms. *Phys. Rev. A*, 91:033630, Mar 2015.

[265] Kuei Sun, Chunlei Qu, and Chuanwei Zhang. Spin–orbital-angular-momentum coupling in bose-einstein condensates. *Phys. Rev. A*, 91:063627, Jun 2015.

[266] Ke-Ji Chen, Fan Wu, Shi-Guo Peng, Wei Yi, and Lianyi He. Generating giant vortex in a fermi superfluid via spin-orbital-angular-momentum coupling. *Phys. Rev. Lett.*, 125:260407, Dec 2020.

[267] Liang-Liang Wang, An-Chun Ji, Qing Sun, and Jian Li. Exotic vortex states with discrete rotational symmetry in atomic fermi gases with spin-orbital–angular-momentum coupling. *Phys. Rev. Lett.*, 126:193401, May 2021.

[268] S Tsesses, E Ostrovsky, K Cohen, B Gjonaj, NH Lindner, and G Bartal. Optical skyrmion lattice in evanescent electromagnetic fields. *Science*, 361(6406):993–996, 2018.